Design of Indium Arsenide nanowire sensors for pH and biological sensing and low temperature transport through p-doped Indium Arsenide nanowires

Shivendra Upadhyay

This thesis has been submitted to the PhD School of The Faculty of Science, University of Copenhagen

Academic advisor

Jesper Nygård

Referees

Charles M. Marcus

Michel Calame

Winnie E. Svendsen

Submitted

October 17, 2013

Contents

Abstract

With the goal of real time electrical detection of chemical and biological species, nanowires have shown great promise with high sensitivity due to their large surface to volume ratio. While the focus of such electrical detection has shifted to one dimensional semiconductor nanostuctures, Silicon remains the primary material of choice.

This research is about investigating Indium Arsenide nanowires as alternative platform for sensing charged species - chemical and biological, in solution. In the thesis, a basic understanding of the underlying mechanism for the sensitivity of the sensor to surface interactions of charged species is first presented. Progressing from H^+ ions to protein sensing, the implication of the finite size of the protein and electrostatic screening due to counter-ions is discussed. Then, starting with nanowires grown via molecular beam epitaxy in a ultra high vacuum chamber, we discuss the fabrication of nanowire transistors using both UV and electron beam lithography as well as the steps to encapsulate the nanowire transistors into an electrically isolated water tight package to be used in a fluidic exchange setup. In the following chapters experiments demonstrating pH sensitivity of the NW sensor are presented. Starting with a simple fluid exchange setup and non-buffered H^+ ion solutions, several iterations of experiments are presented, with each iteration aimed at improving the reliability and reproducibility of the nanowire sensors with changes to type of H^+ion solution, method of solution delivery and evacuation as well as additional electrodes immersed in the solution.

Having established and tested a stable sensing platform via pH sensing, we apply the same to a more complex system - proteins. The sensing protocol involves the functionalization of the sensor surface with biotinylated BSA followed by the addition of the protein of interest - Streptavidin (Avidin). While BSA and Streptavidin are negatively charged at the pH values of the buffers used, sensor response to the positively charged Avidin is used to check if the response is based on the protein

charge. The magnitude and stability of the sensor response to protein binding with changing ion concentration in the pH buffer used is also studied.

Finally, we present low temperature measurements on p-doped InAs nanowires. It is a unique system with a surface electron layer, an intrinsic property of InAs, along with a hole doped core. By means of an external electric field, the majority charge carrier in the nanowire is changed from electrons to holes. Transport properties of the charge carriers is studied as a function of source-drain bias, gate bias, temperature and magnetic field.

Dansk resume

Nanotråde har høj sensitivitet, grundet deres høje overflade/volumen forhold, og er en lovende platform til realtids elektrisk detektering af kemiske og biologiske stoffer. Mens fokus på elektrisk detektion har skiftet til en-dimensionelle halvleder nanostrukturer er silicium stadig det mest benyttede materiale.

Denne forskning undersøger indiumarsenid nanotråde som en alternativ materialeplatform til at detektere ladede partikler, både kemiske og biologiske, i opløsning. Først præsenteres de basale mekanismer for sensorens reaktion på overfladeudvekslinger med ladede partikler. Gennem en udvidelse fra H^+ ion til proteindetektering belyses påvirkningen af proteinets endelige størrelse og den elektrostatiske screening på grund af counterioner. Derefter diskuteres hvordan molekylestråle epitaxiskt dyrkede nanotråde bruges til at lave nanotrådstransistorer ved brug af både UV og elektronstråle litografi, og hvilke trin der er nødvendige for at pakke nanotrådstransistorne ind i en elektrisk isoleret og vandtæt pakke, der kan bruges i en væskeudvekslingsforsøgsopstilling. I de følgende kapitler præsenteres eksperimenter der demonstrerer nanotråds sensorens pH følsomhed. Med udgangspunkt i en simpel væskeudvekslingsforsøgsopstilling og ikke-bufferede H^+ ionopløsninger præsenteres flere forsøgsiterationer, hvor hver iterations mål er at forbedre pålideligheden og graden af reproduktion af nanotrådssensorens følsomhed over for ændringer i typen af pH-opløsning, måden hvormed opløsningen leveres og fjernes, samt yderligere elektroder nedsænket i samme opløsning.

Den udviklede og testede stabile pH-sensorplatform, bruges derefter til det mere komplekse system - proteiner. Protein sensorprotokollen starter med en funktionalisering med biotineret BSA, der er et alment brugt protein der nemt binder til overflader og den biotinerede version binder yderligere til andre proteiner. De proteiner der skal undersøges, Streptavidin og Avidin, kan derfor binde til den BSA funktionaliserede sensor overflade. Mens både BSA og streptavidin er negativt ladede ved de benyttede bufferes pH-værdier er Avidin positivt ladet, derfor benyttes Avidin til

at teste om sensorens reaktion er baseret på proteinernes ladning. Størrelsen og stabiliteten af sensorens reaktion på protein binding ved ændrede ionkoncentrationer i pH-bufferen er også studeret.

Endeligt præsenterer vi lavtemperatur målinger på p-doterede InAs nanotråde. Det er et unikt system med et overflade-elektron lag, en iboende egenskab af InAs, kombineret med en hul-doteret kerne. Ved brug af et eksternt elektrisk felt ændres majoritet ladningsbærertypen i nanotråden fra elektroner til huller. Transportegenskaberne af ladningsbærerne studeres som en funktion af source-drain spænding, gate-spænding, temperatur og magnetisk felt.

Acknowledgments

The conclusion of this thesis marks the end of a stage for me - I shall no longer be a university student. There are several people[1] I would like to acknowledge who have made this journey... well, fun[2]!

I would have never come to Copenhagen had it not been for Jesper and a misleading wiki article about the weather here. Jesper was the head of a small but well equipped lab, armed with metallization chambers, an AFM, an SEM and soon a shiny Raith eLine-100. There were dilution fridges, both old and new but best of all, there was this friendly group dynamic that sucked you in. Thank you Jesper, for giving me enough independence to figure out my way through this project and still keeping an eye on me to make sure I did not stray too far from the original objective.

Claus and Nader deserve a special mention. Their tireless work behind the curtains kept the essential equipment online and not much would get done without them.

Rune Frederiksen, you were involved in all the crazy BioFET experiments and the subsequent analysis. Thank you for the unending supply of the buffers and proteins - both the approved and unapproved variety. I'm glad the NWs finally 'saw' the proteins in the end. Thank you for patiently reading through the thesis chapters and your detailed feedback. I hope to return the favour in a year :)

Peter Nissen, you were my office mate high up on the 5th floor and again on the 2nd, after the bio-displacement. I have enjoyed all our little conversations as well as our joint efforts to combat covert surveillance. *cough... mirror... cough.* Peter '$\Delta G < 0$' Krogstrup, Jeppe 'Lars' Holm, Morten, Rawa, Paweł and now Giulio, there's never a dull moment to be had having shared an office room with you. Peter, it's nice when accidental conversations last longer than the trip to the coffee machine and back, and eventually lead to collaborations. Jeppe, we need to reconsider the 'Lars'

[1] Foot notes are awesome

[2] I'll assume my acknowldgements from my B.Tech and MSc theses are still valid, so I won't have to go too far back.

coffee rule. It's good that you're still hanging around. Peter and Morten, thank you for the neat wires that you grew for us. At times, it felt like a bakery, where one could 'order' a certain type of bread.. um, nanowires and have them the next day, if the oven was warm and ready. Giulio, I see the MBE is almost ready again. Prepare yourself for the fresh round of orders :) Rawa, I wish you all the best with your PhD. It's definitely more fun with more people around.

Thomas and Kasper, you were the cornerstones of the old lab and always willing to help out the young ones. I am grateful for the all the times for taking time out and showing me the ropes. Thomas, I admire your ability to plan the most efficient route for a research project and our *p*-type adventure was an interesting detour. Kasper, I have pestered you about topics ranging from the humble current pre-amplifier to funky 3D mathematica models and I grateful for your good natured help every single time.

One valuable experience was being a lab assistant for the experimental section of the course Nano3. I loved breaking down text book quantum mechanics experiments and explaining phenomenon with little or no equations, and in the process learning as much as the students themselves... students, who are now master students and I wish them all the best in whatever endeavour they choose.

Diana, you were patient and supportive through the pressures of the final year and I'm glad you were there. I look forward to spending more time with you than nanowires now :)

I would also like to.. *[what? Music? I guess, they're playing me off!]* I'm glad I'll be sticking around doing what I love with people that are fun and... *mic goes dead*

1. Introduction

> "*...[while] video cameras arguably provides an artificial eye on our world, we seem to be missing effective electronic versions of our other senses.*" - Anthony Turner[1]

1.1. Scope

In the past decade one dimensional (or nearly one dimensional) semiconductor structures of nanometer dimensions referred to as nanowires (NWs) have shown great promise in a variety of fields. Demonstrations of NWs as a transistor[2], optoelectronic devices[3–5], solar cells[6], gas sensors[7] as well as chemical/biological sensors[8,9] have established NWs as a versatile platform for a variety of applications. As for some of the more novel applications NWs have provided a system where at cryogenic temperatures a single electron/hole can be trapped in a 'box' (quantum dot) and its spin could be manipulated by means of an external electric field[10,11]. More recently signatures of Majorana fermions have been seen in InAs, InSb NWs[12,13] and may lead to a new direction for quantum computation. Solar cells based on individual standing NWs show a larger effective efficiency[14] and combined multi-junction NWs could hold much potential.

With growing expertise over growth and fabrication of NW based devices there was an interest in applying NWs as an interface with biological systems. The concept of using planar MOSFET devices with the gate region exposed to solution as a chemical/biological sensor was introduced in 1970[15] and in 2001 with the demonstration of Si NWs as a pH and a protein sensor by Cui et al[8] there was renewed interest in applying new 1D and 2D systems to the field of chemical and biological sensing.

1.2. Sensor concept

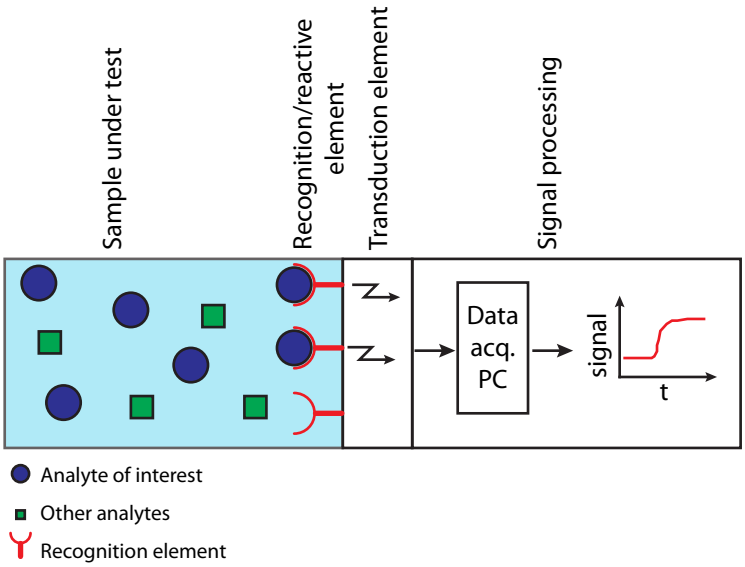

Figure 1.1.: Schematic depiction of a chemical/biological sensor with its constituting components: a recognition element that specifically binds/reacts to the analyte of interest, a transduction element that responds to the binding/reaction event at the interface and a data acquisition/signal processing setup that measures and displays the response of the transduction element.

Fig. 1.1 shows the general scheme of a biosensor comprising a recognition element that reacts to the presence of a target molecule with high specificity, a transduction element which responds to the interactions at the interface with the recognition element and finally a data acquisition/measurement setup which measures and displays the response of the transduction element. Typical recognition elements can be catalytic based - enzymes, whole cells, etc or affinity based - single strand DNA, antibodies and other elements that facilitate specific molecular binding to the target analyte. The recognition element can be immobilized on the surface of the transduction element via chemical bonding or physical adsorption, entrapment, etc.

Some of the common transduction element types are electrochemical, electromechanical and optical. Electrochemical elements respond with a change in conductance/current and typically involve charge transfer or a capacitive interaction with the charge of the binding molecule. Electromechanical elements such as cantilevers and quartz crystal microbalance respond with a change in resonant frequency dependent on the mass of the binding molecule. Optical elements detect changes (surface

plasmon resonance) via the interaction of light with the surface due to small changes in refractive index for example due to the binding of target molecules. The common underlying principle is that the response is based on an intrinsic property of the target molecule such as charge and mass. The choice of the transduction mechanism is dependent on the requirements of scalability, throughput, multiplexing, size limitations, etc.

Typically label based detection schemes involve labeling of the target analyte with a fluorescent dye or radioisotopes tags. Labeling is time and labour intensive and while this method has been shown to be ultra-sensitive, there are uncertainties associated with labeling and its effect on the conformational properties as well as function of the target molecule under investigation. The label free biosensors on the other hand allow a scheme which can be applied not only to the detection but also real time binding/interaction kinetics of analytes[16]. With the end goal of interfacing with biological systems such as proteins and even cells, label-free techniques make it possible to work with unmodified systems and thereby avoid artifacts.

1.2.1. Semiconductor field effect transistor (FET)

In this thesis we present a conductance based FET sensor with the goal of demonstrating a stable sensing platform using InAs NWs. A semiconducting NW FET lies at the heart of the scheme. A semiconductor is a material with properties between that of a metal and an insulator, see Fig. 1.2. The valence band in a material refers to

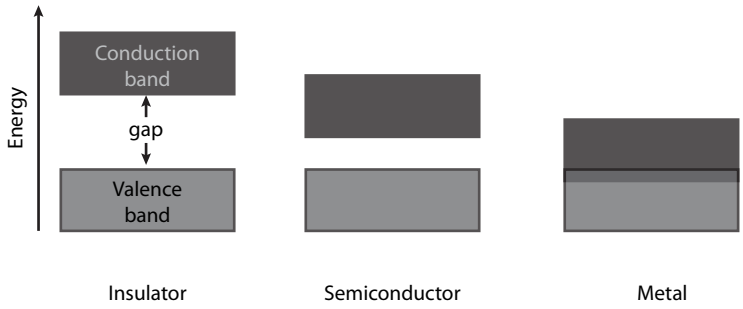

Figure 1.2.: The energy gap between the conduction and valence band in an insulator, semiconductor and a metal. The shaded regions indicate bands of allowed states.

the range of energies of an electron bound to the atomic nuclei while the conduction

band refers to energies of electrons that are free. In a semiconductor these bands are separated in energy by a small gap, the band gap. At finite temperature, electrons from the valence band can acquire energy and be excited into the conduction band thereby creating mobile holes in the valence band and electrons in the conduction band, that can now move in response to a source-drain bias. Semiconductors can be intentionally doped with impurities that can add electrons (holes) to the system increasing conductivity. The typical charge carrier density in an undoped Si is around $10^{10}\,\mathrm{cm}^{-3}$ and with doping this value can be increased to $10^{18}\,\mathrm{cm}^{-3}$. In addition to this semiconductors have another interesting property. With the application of a electric field, typically via a metal electrode in close proximity, the concentration of the charge carriers can be affected locally making it possible to deplete or populate a segment of electrons (holes) controlling conductivity.

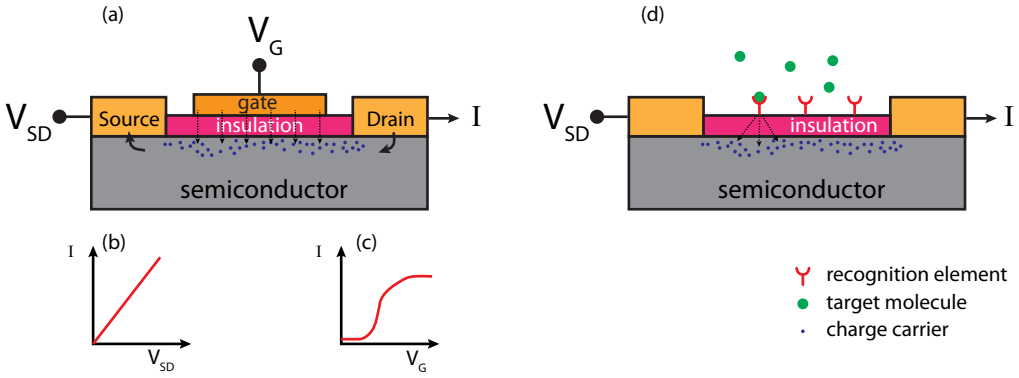

Figure 1.3.: Basic scheme of a (a) typical MOSFET and current through the device as a function of (b) source-drain bias V_{SD} and (c) gate bias V_G. (d) FET based sensor is a modified MOSFET with the gate electrode exposed solution and the interface functionalized with the recognition element.

For simplicity we assume an n-doped semiconductor with electrons as the majority charge carriers but the discussion is valid for a p-doped semiconductors as well. Fig. 1.3 a shows a simplified scheme of a metal oxide semiconductor field effect transistor (MOSFET). The source-drain electrodes make ohmic electrical contact with the semiconductor leading the current into and out of the semiconductor. The ohmic contact is depicted by the linear response of current I as a function of source-drain bias V_{SD}, Fig. 1.3 b. The gate electrode only couples capacitively to the semiconductor and voltage applied to this electrode V_G can tune the density of electrons in the conducting channel between the source-drain electrodes, thereby affecting current (conductance), Fig. 1.3 c. Applying a negative V_G would deplete electrons under the

gate while applying a positive potential would accumulate electrons. This effect of the electric field from the gate on the current/conductance of the semiconductor is referred to as the field-effect.

Bergveld[15] proposed modifying this device concept into a sensor by exposing the gate electrode region to solution with the insulator ensuring a capacitive only interaction, Fig. 1.3 d. The interface with the solution could be modified with an ion-selective membrane, an insulator with a high density of reactive terminal groups, single strand DNA or other biological recognition motif. This forms the basis of the operating principle of the FET sensor - interaction of the target species (protons, proteins, ions, etc) changes the surface charge distribution at the solution-semiconductor interface which is transduced into a change in current/conductance via electrostatic field effect. Thus, a positively charged molecule binding to the surface would lead to increased current/conductance due to increased accumulation of electrons. The timeline for the introduction of devices based on these concepts (Ion Sensitive FETs, Gene screening FETs, Enzyme coupled FETs, etc) and experimental realizations are summarized by Schöning et al[17].

1.3. Choice of system: form factor and material

All devices mentioned above utilize planar geometry and primarily Si as the choice of material. In the last decade new novel materials such as carbon nanotubes (CNTs), graphene have been realized and great progress has been made in the controlled growth of nearly 1D semiconducting nanostructures (NWs). 1D nanostructures being on a similar size scale as the biological systems of interest, can have significant advantages with regard to signal to noise presented in the sensor response as well as detection limits. In the following we discuss the advantages of 1D form factor.

1.3.1. Form factor: 1D Nanowires

NWs can be made via either bottom up or top down methods. The bottom up approach typically involves an evacuated chamber in which the constituent precursors dissolve in a catalytic gold seed at elevated temperatures (~400 °C), supersaturate and crystallize out at the bottom of the gold droplet. In this manner a single crystal NW grows layer by layer. Molecular beam epitaxy (MBE) and metal organic

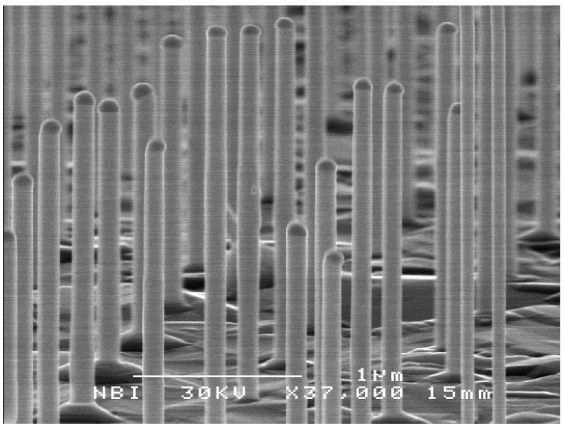

Figure 1.4.: An SEM image of InAs NWs grown via MBE. Image courtesy of P. Krogstrup.

vapour phase epitaxy (MOVPE) are some examples of this technique. Due to the gradual relaxation of strain in the radial direction bottom up techniques can be used to tailor NWs with a large range materials and dopants to achieve radial and axial heterostructures that may not be possible in the 2D planar geometry due to lattice mismatch. Top down techniques involve etching out 1D nanostructures out in a substrate of suitable material. Such NWs can be doped post etching via high energy ion implantation.

NWs typically are $\sim 50 - 100\,\text{nm}$ in diameter and a few microns in length, and thus possess a large surface to volume ratio. In comparison to planar ISFET systems, NWs have one dimension much closer to the typical size of biological systems and interactions at the NW surface are likely to affect the 'bulk' of semiconductor[8]. NW based FET sensors have shown the sensitivity to detect a single virus[18] and telegraph noise due to the trapping-detrapping of a single electron has been observed[19] in short Si NW devices (W $\times$ L - 30 $\times$ 60 nm) at room temperature, all confirming NWs as building blocks for ultra sensitive and large signal-to-noise[20] sensors. In addition to sensitivity, the form factor also allows access that may not be feasible with the 2D geometry. As an example of this consider the interfacing of live cells with standing NWs by Berthing et al[21] and intra-cellular probes by Duan et al[22]. Nair et al[23] simulated the kinetics of the detection taking diffusion of the analyte to the sensor surface into account and have found moving from planar (2D) to NW (1D) geometry offers significant improvements in the average detection time and the detection limit given a reasonable incubation time. Finally, the small form

factor allows for the fabrication of large arrays of devices and by functionalizing different areas of the sensor chip differently (spotting) and thus enabling multiplexed detection[24].

1.3.2. Materials and sensing experiments

Table. 1.1 presents an overview of some of the recent applications of 1D and 2D nanostructured materials used for FET based sensors. Si is the material of choice in the semiconductor industry and there is large body of knowledge regarding semiconductor processing, doping as well as chemical surface modification. Indeed, the first NW sensor was based on a Si NW[8] grown via a bottom up technique[27]. Using *p*-doped NWs, Cui et al demonstrated pH sensing, both with and without sensor surface modification (APTES). After immobilizing biotin on the surface, they demonstrated irreversible binding of Streptavidin down to a concentration of 10 pM as well as the reversible binding of m-antibiotin. Detection of calcium ions was also shown with the immobilization of calmodulin on the sensor. Using either a single NW or multiple parallel NWs based devices detection of DNA down femtomolar levels has been shown[28,29] . Patolsky et al[18] demonstrated the sensitivity of NW based sensors with the detection of a single virus (influenza A). Progressing towards more complex motifs, others[30] have managed to control the binding of ATP to the sensor surface as well as ultrasensitive detection of uncharged steroids[31]. Combining transparent flexible substrate platforms with FET sensors[32] allows additional manoeuvering freedom as well as simultaneous optical monitoring[33]. The specificity of antigen-antibody binding has been used to demonstrate[9,24,34] facilitate the binding and detection of several target species, however the size of the recognition element requires large Debye lengths or salt concentrations orders or magnitude lower than physiological conditions. One proposed approach to deal with the Debye screening limitation was shown by Stern et al[35] where T-cells were triggered into releasing protons into solution on exposure to the target molecules and the FET sensor responds to the change in pH.

The above concept was extended[36], termed ne-ELISA, using In_2O_3 NWs wherein the gold source-drain electrodes were functionalized via thiol chemistry with urease. Reaction with the target molecules interleukin-2 results in the release of protons which in turn results in a pH response from the NW sensor, thus demonstrating detection in physiological salt concentrations. In_2O_3, ZnO[37], SnO_2 based NWs are

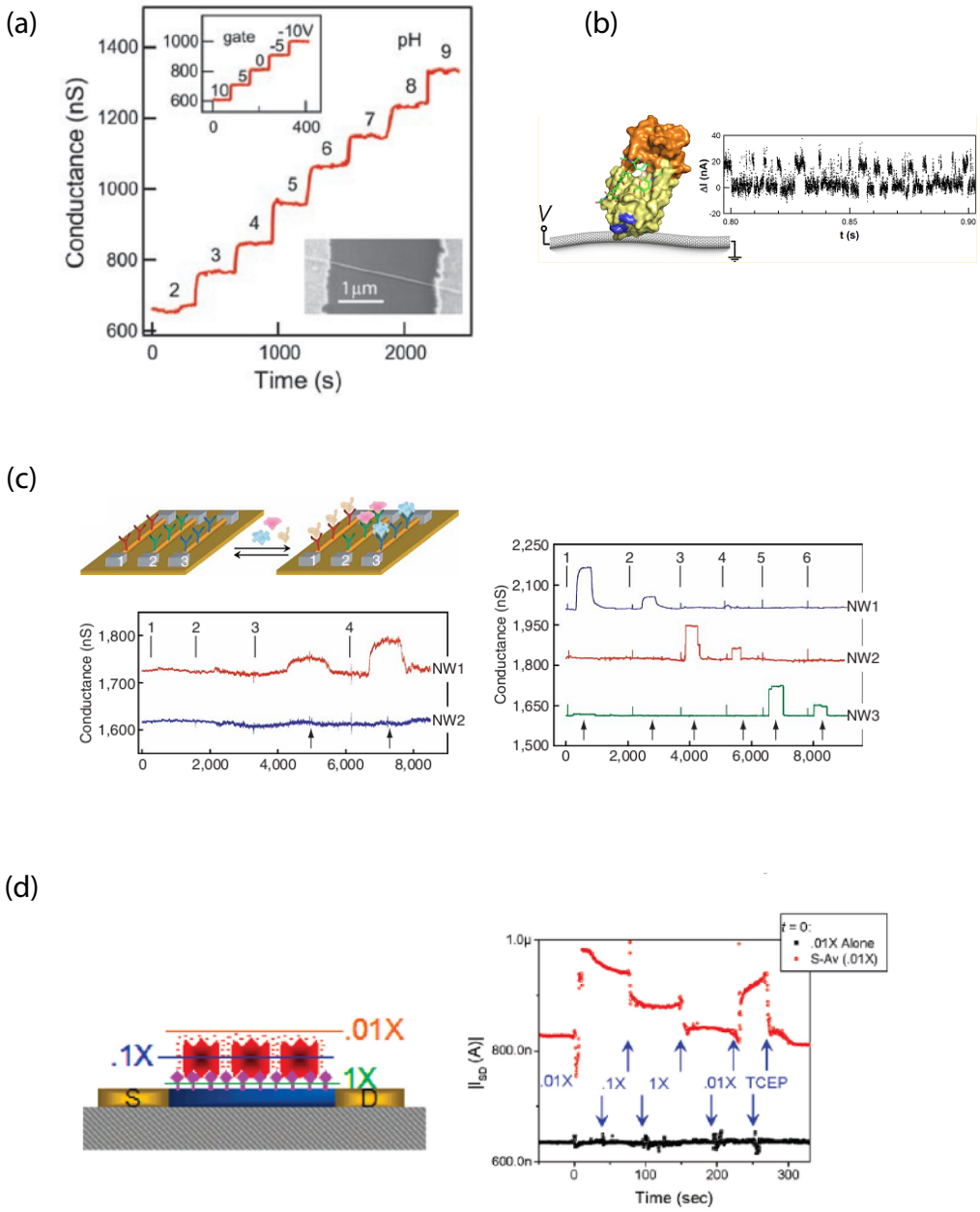

Figure 1.5.: Some demonstrations of sensing applications. (a) Cui et al[8] demonstrate pH sensing using Si NW FETs. (b) Choi et al[25] demonstrate the transduction of the binding of a single enzyme molecule to a CNT FET. (c) Zheng et al[24] show multiplexed detection using Si NW FETs. (d) Stern et al[26] show the impact of ionic screening on the FET sensor response.

not very conducting but have the advantage that the surface is not capped with a native insulating layer. NWs of such materials have been applied to a variety of detection schemes[38–42].

CNTs[25,43,44] are another popular choice of chemical and biological sensing. A known drawback is that the methods of growing CNT yields a mixtures metallic and semiconducting tubes without an easy way to separate or identify either group without electrical measurement. Only the semiconducting CNTs would respond interactions with charged target molecules with a change in conductance. CNTs can be functionalized[45] and have been successfully demonstrated as a biosensor to detect t-PSA[46], alga as well as streptavidin[47], E-coli[48], DNA[49] and even direct analysis of human serum[50]. Single molecule (lysozyme variants) detection has also been shown using CNT FET sensors[25].

Graphene based FET sensor are planar (2D) and thus do not protrude from the surface as well as small active area. Cohen-Karni et al[51] demonstrate electrical detection of a beating embryonic chicken cardiomyocyte while others[52,53] have shown pH as well as glucose sensing. Conducting polymers (poly-pyrrole based) is another example of new materials being applied to FET based sensing using the NW/nanotubes form factor and have been used to demonstrate detection of bacterial spores and other biological elements[54–56].

1.3.3. Motivation: InAs

InAs is a well known high mobility[57,58] III-V semiconductor applied to electronic as well as opto-electronic fields due to its small band gap and low effective electron mass. It has a characteristic surface electron accumulation layer which yield problem free ohmic electrical contact. In addition NWs of this material can be grown with control over morphology and doping, both n and p. Finally, the Thomas-Fermi screening length in the material is comparable to the size of the electron accumulation layer[59,60] and we expect surface interactions with ions and proteins would influence the 'bulk' of the conducting charge carriers. While InAs NWs have already been applied as gas sensors[61] as well as extracellular interface with live mammalian cells[21], to the best of our knowledge they have not as yet been applied as FET based chemical and biological sensors.

Table 1.1.: Overview of nanostructured materials used for chemical and biological sensing as well target molecules and the corresponding limit of detection (LOD). Nanowire biosensors have been reviewed in greater detail in a number of articles elsewhere[62–66].

Material	Authors	NW type	Target/Receptor	LOD
Si	Cui et al[27]	Bottom up	H^+/ bare oxide & APTES modified	-
			streptavidin/BSA-biotin	10 pM
			m-antibiotin/biotin	5 nM
			Ca^{+2}/calmodulin	25 μM
	Hahm et al[28]		DNA/PNA	10 fM
	Patolsky et al[18]		Single virus	-
	Zheng et al[24]		PSA/anti-PSA	1.4 pg ml^{-1}
			CEA/anti-CEA	2 pg ml^{-1}
			mucin-1/anti-mucin-1	5 pg ml^{-1}
	Wang et al[30]		Conc. dependent inhibition of Gleevac	-
	Gao et al[29]	Top down	DNA/PNA	25 fM
	Chang et al[31]		steroid,19-norandrostendione/Δ^5-3-Ketosteroid isomerase	1.3 fM
	Stern et al[9]		Streptavidin/biotin	10 fM
			Avidin/biotin	1 nM

			Mouse Immunoglobulin A and G/anti-IgA, anti-IgG	100 fM
	Lee et al[67]		C-reactive protein/anti-CRP	1 fM
	Tian et al[34]		BSA/anti-BSA	0.13 fM
	Tarasov et al[68,69]		H^+	-56 mV/pH
	Wipf et al[70]		K^+	1 mM,-44 mV/dec.
poly-Si	Hsiao et al[71]		Avidin & Streptavidin/biotin	167 fM
	Hakim et al[72]		Interleukin-8 (IL-8)/Anti-IL-8	10 fM
			tumor necrosis factor-alpha (TNF-α)/Anti-TNR-α	10 fM
In_2O_3	Stern et al[36]	Bottom up	interleukin-2 via ne-ELISA	1.6 pg ml^{-1}
	Ishikawa et al[41]		Nucleocapsid (N) protein/Antibody mimic protein	0.6 nM
	Li et al[38]		PSA/anti-PSA	5 ng ml^{-1}
	Rouhanizadeh et al[39]		Differentiate reduced and oxidized LDL cholesterol/anti-oxLDL,non-anti-oxLDL	-
ZnO	Yeh et al[42]		hemoglobin/physical adsorption	2 fg ml^{-1}

SnO_2	Cheng et al[40]	Bottom up/- Nanobelt	H^+/ bare oxide & APTES modified	-
CNT	Okuno et al[46]	-	t-PSA	
	Ishikawa et al[47]		streptavidin	
	Subramanian et al[48]		E-coli	
	Kurkina et al[49]		DNA	
	Choi et al[25]		lysozyme variants	single molecule
Graphene	Lei et al[52]	Mech. exfoliation	H^+	-
	Hunag et al[73]	CVD	glutamate molecules/glucose oxidase	0.1 mM
Polypyrrole	Tolani et al[54]	Electrochem. fabrication	HSA/anti-HSA	50 nM
	Aravinda et al[55]		Cu^{+2} via chelation	10 fM
			His_5-syntaxin	1 ng ml^{-1}
	Garcia-Aljaro et al[56]		Bacterial spore	-

1.4. Outline of the thesis

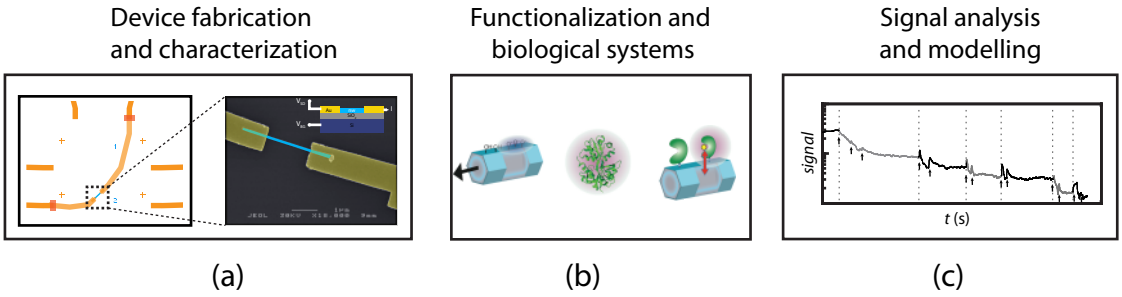

Figure 1.6.: Interdisciplinary inter-department collaboration. (a) Device fabrication and measurement setup is handled in Jesper Nygård's group (Nanoscience/-Nanophysics). (b) Protein protocol and sensor functionalization is investigated and optimized in Karen Martinez's group (Bionanotechnology) . (c) Measurement and signal analysis is performed together while modeling of the sensor response is performed in Jan Jensen's group (Chemistry).

This work was in part funded by the UNIK center for synthetic biology. Synthetic Biology is the engineering of biology, a deliberate (re)design and exists in the intersection between biological sciences, chemistry, physics and information technology.. The center creates a framework for research in synthetic biology and gathers researchers and students from several departments at University of Copenhagen. The work done in this thesis is part of a larger picture involving three different research groups, Fig. 1.6:

- Nanophysics (Jesper Nygård): Device fabrication and electrical characterization
- Bionanotechnology (Karen Martinez): Surface functionalization and biological systems
- Chemistry (Jan Jensen): Signal analysis and modeling.

The overall objective of this thesis is to demonstrate and establish InAs nanowires as a stable platform for rapid real time detection of chemical and biological species. The outline of the thesis is divided as follows:

In chapter 1, we have presented an overview of the field of chemical and biological sensing. We present various label free detection schemes and reasons why they may be preferred over label based schemes. Recent breakthroughs and state of the art is presented. Motivation for using InAs as well the NW form factor are explained.

In chapter 2, a brief overview of the theory of pH and protein sensing is presented. We shall understand the response of the sensor to solutions of varying pH values arises from the interaction of protons in solution with the terminal groups, typically hydroxyl (-OH), at the sensor-solution interface. The influence of the terminal group density, reactivity and electrolyte composition is discussed. We conclude with a discussion of sensor response to protein interaction with the surface. Due to protein size being comparable to the ion screening length in solution, spatial distribution of charge within the protein becomes relevant.

In chapter 3, the material - InAs is presented and the method of NW growth is briefly discussed. A field effect transistor (FET) is explained. Starting with the lithographic techniques for the fabrication of FET devices, we outline the steps needed to go from a forest of InAs NWs to a FET based sensor electrically isolated and encapsulated in a dual inline pin (DIP) socket. We conclude with the presentation of the fluidics setup.

In chapter 4, to demonstrate a sensing platform using InAs nanowires, we demonstrate proof of concept by establishing a pH sensor. Different iterations of device setup/protocol are discussed to overcome limitations of the previous generation. We conclude with the demonstration of a stable reproducible platform with respect to pH sensing.

In chapter 5, having established a stable platform we apply the same to a more complex system - proteins. The sensing protocol involves the functionalization of the sensor surface with biotinylated BSA followed by the addition of the protein of interest - Streptavidin (Avidin). BSA is a commonly used protein that binds easily to surfaces and the biotinylated version of the protein allows binding to additional proteins. While BSA and Streptavidin are negatively charged at the pH values of the buffers used, sensor response to the addition of positively charged Avidin is used to check if the response is based on the protein charge.

In chapter 6, we present low temperature measurements on p-doped InAs NWs. It is a unique system with a surface electron layer, an intrinsic property of InAs, along with a hole doped core. By means of an external electric field, the majority charge carrier in the NW is changed from electrons to holes. Transport properties of the charge carriers is studied as a function of source-drain bias, gate bias, temperature and magnetic field.

In chapter 7, we provide concluding remarks and an outlook on InAs NWs for sensing

applications.

2. Theoretical Formulation of Nanowire sensing

In this chapter we present a simple theoretical model in order to understand the NW sensor-electrolyte system. We first present the site binding model to explain the interaction of protons (H^+) in the electrolyte with the sensor surface and the resulting surface charge distribution. The relevant capacitances in the system are discussed which relate the surface charge density to the current flowing through the NW. Properties of the sensor surface which impact the extent of interaction with the electrolyte are discussed and the upper limit for the same is derived. We briefly discuss the role of other ions in the electrolyte and their interactions with the surface. Finally, moving from chemical to biological species we introduce a basic scheme of protein detection and the role of Debye lengths.

2.1. Principle of operation

As mentioned earlier, Sec. 1.2.1 a semiconducting NW used as a field effect transistor[1] lies at the heart of our sensor. The schematic in Fig. 2.1 a shows a typical NWFET sensor device exposed to an aqueous solution. Electrical isolation, typically an oxide, prevents leakage current between the electrolyte and the NW, ensuring a capacitive only interaction with the surface. The concept first explored by Bergveld et al[15,74,75] involves a planar FET with the gate insulation exposed to solution instead of a metal electrode. The sensing mechanism involves a change in the conductance of the FET in response to a change in surface charge distribution via field effect. Exploiting the large surface to volume ratio, Cui et al[8] were the first to use semiconducting (Si) NWs to demonstrate highly sensitive FET sensors.

[1] our FET devices are discussed later in Sec. 3.3

For a NW of radius r, uniform carrier concentration ρ, carrier mobility μ and electron charge e, its conductance within the Drude model is given by $G = e\mu\rho\pi r^2$. Here we consider the bulk conductance of the NW and ignore the role of the contacts. Modulation of ρ changes G and with G_0 as the initial conductance, it is convenient to define a dimensionless parameter $\frac{\Delta G}{G_0}$ to describe the sensor response[76]. This normalized parameter allows comparison of response from sensors of varying dimensions and doping densities, describing the volume ratio of the NW that responds to the surface potential to the total bulk. This term increases[76] with the increasing surface to volume ratio as well as decreasing carrier densities (increasing Thomas-Fermi length). Alternatively, the system can be described using different parameters. The surface charges (σ_T) result in a potential profile, see Fig. 2.1 c. With ψ_0 denoting the potential at the sensor surface, converting[2] ΔG back to $\Delta\psi_0$ is convenient as the latter quantity solely depends on the interactions of the insulator surface with the electrolyte which is the primary interest of using the sensor.

2.2. Electrolyte-Insulator interface

The following discussion on the origin of the solution pH dependent sensor response is based on Bousse et al[78] and Nair et al[79]. The site binding model[80,81] (SBM) is a commonly accepted model for relating charge and potential at the electrolyte-insulator interface[68,82–84]. The FET sensor is separated from the solution by typical electrically insulating materials such as SiO_2, Si_3N_4, Al_2O_3, HfO_2, etc[85]. The surface of these insulators have reactive terminal groups, typically hydroxyl groups (-OH) formed by the hydrolysis of the surface oxide groups and the former can either be charged or neutral depending on the solution (Fig. 2.2). The protonation/deprotonation reactions at the interface are each characterized by an equilibrium constant K,

$$[I-OH] \overset{K_a}{\rightleftharpoons} [I-O^-] + [H_s^+],\ K_a = \frac{[I-O^-][H_s^+]}{[I-OH]} \tag{2.1}$$

$$[I-OH_2^+] \overset{K_b}{\rightleftharpoons} [I-OH] + [H_s^+],\ K_b = \frac{[I-OH][H_s^+]}{[I-OH_2^+]} \tag{2.2}$$

$[I-OH]$, $[I-O^-]$ and $\left[I-OH_2^+\right]$ are the molar concentration of the interfacial

[2]The method is explained later, see for eg. Sec. 4.2

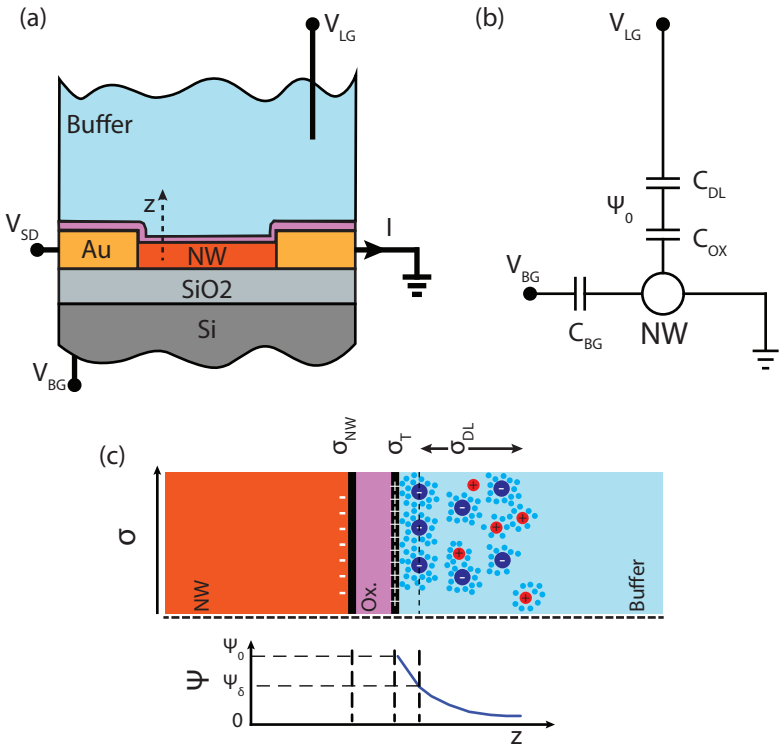

Figure 2.1.: (a) Schematic of the nanowire device showing the source-drain bias (V_{SD}), backgate bias (V_{BG}) and liquid gate bias (V_{LG}). (b) A schematic of the relevant capacitances in the circuit. This is discussed in detail later in Sec. 2.3. (c) Charge distribution along the dotted line in (a) (adapted from [23] and [77]). σ_T is the charge distribution at the oxide-electrolyte interface due to protonation-deprotonation reactions. This charge attracts ions with densityσ_{DL} in the electrolyte as well as induces σ_{NW} in the semiconductor. The potential distribution at the oxide-buffer interface according to the Gouy-Chapman-Stern model is shown below. ψ_0 is the potential at the surface while ψ_δ is what is referred to as the Stern potential.

hydroxyl groups and $[H_s^+]$ the proton concentration close to the oxide surface. The surface density of the hydroxyl groups at the surface is the sum of the charged and neutral species,

$$N_s = [I - OH_2^+] + [I - O^-] + [I - OH] \tag{2.3}$$

The surface charge density, σ_T is then the difference of the positive and negative charges at the surface,

$$\sigma_T = q\left([I - OH_2^+] - [I - O^-]\right) \tag{2.4}$$

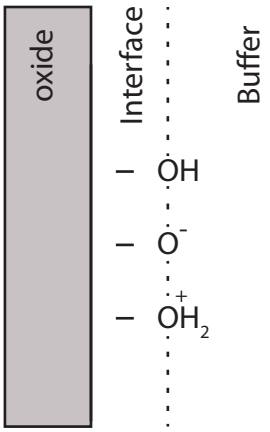

Figure 2.2.: Hydroxyl groups at the insulator-electrolyte interface can be neutral (I-OH), protonated (I-O$^-$) or de-protonated $\left[\mathrm{I}-\mathrm{OH}_2^+\right]$.

Combining Eqn. Eqn. 2.1 -Eqn. 2.4, we see that the surface charge density is a function of the local hydrogen ion concentration ($[H_s^+]$) and depends on the reactivity (K_a, K_b) as well as density (N_s) of the terminal groups,

$$\sigma_T = qN_S\left(\frac{[H_s^+]^2 - K_aK_b}{K_aK_b + K_b[H_s^+] + [H_s^+]^2}\right) \tag{2.5}$$

When the surface is electrically neutral, ($\sigma_T = 0$) there is no corresponding potential profile in solution and thus no concentration gradients for the ionic species. Defining $pK = -\log K$, this situation occurs when $pH = \frac{pK_a+pK_b}{2}$ with equal numbers of protonated and de-protonated hydroxyl groups, as seen in Eqn. Eqn. 2.5. This pH is referred to as the point of zero charge, $\mathrm{pH_{pzc}}$. For $pH < pH_{pzc}$, the surface is positively charged with an excess of $\left[-OH_2^+\right]$ and negatively charged with an excess of $[-O^-]$ groups for $\mathrm{pH} > \mathrm{pH_{pzc}}$.

Charges at the surface attract counter ions in the solution. Due to finite size of the ions as well as their low concentration, a single layer of ions cannot sufficiently screen the surface charges leading to a diffuse layer of counter-ions near the surface and hence a potential profile. The Gouy-Chapman-Stern model is used to estimate this oxide-electrolyte interface potential[86]. Due to the finite size of the ions in the buffer, there is a minimum separation between the ions and the surface. This layer is referred to as the Stern layer (Helmholtz layer) and is electrically neutral. This is followed by the Gouy-Chapman layer (the diffuse layer) which is a mixture of a

counter-ions and a smaller proportion of co-ions.

With reference to Fig. 2.1 c, the Gouy-Chapman model relates the charge in the double layer to potential[3] at the Stern layer (ψ_δ) as[86,87],

$$\sigma_T = \sqrt{8k_bT\epsilon_W\, c}\, \sinh\left[\frac{e\psi_\delta}{2k_bT}\right] \tag{2.6}$$

where ϵ_W is the permittivity of the electrolyte, ψ_0 is the surface potential, c is the total number concentration of the ion pairs in the buffer calculated by multiplying molar concentration in moles/m^3 with Avogadro's number (N_A), T is absolute temperature and k_b the Boltzmann's constant. The Stern layer is modeled as a capacitor, of capacitance C_{Stern} (typically ~0.2 μF/m^2), with the potential drop across given by,

$$\psi_0 - \psi_\delta = \frac{\sigma_T}{C_{Stern}} \tag{2.7}$$

Thus, using Eqn. Eqn. 2.6 -Eqn. 2.7 the potential profile (ψ_0) due to a charge distribution at the surface (σ_T) is,

$$\psi_0 = \frac{\sigma_T}{C_{Stern}} + \frac{2k_bT}{e}\, \sinh^{-1}\left[\frac{\sigma_T}{\sqrt{8k_bT\epsilon_W\, c}}\right] \tag{2.8}$$

Finally, the Boltzmann's distribution, arising from statistical mechanics, relates the concentration of an ionic species at a given potential with respect to its bulk concentration. The proton concentration close the oxide-electrolyte interface ($[H_s^+]$) which influences reaction dynamics can be written as,

$$\left[H_s^+\right] = \left[H_B^+\right] \exp\left(-\frac{e\psi_0}{k_bT}\right) \tag{2.9}$$

[3]The expression is for a monovalent symmetric analyte such as NaCl. This assumption still allows us to understand the interaction of the surface without complicated equations.

The set of equations governing the surface charge and its dependence on pH of the bulk electrolyte are visualized in Fig. 2.3. The surface charge is related to the $\left[\mathrm{H_S^+}\right]$ via reaction with terminal groups (Eqn. Eqn. 2.5). The resulting surface charge leads to a potential profile which can be solved by Poisson-Boltzmann's equations (Eqn. Eqn. 2.8). Surface potential ψ_0 relates the local and bulk proton concentration ($\left[H_B^+\right]$) via the Boltzmann's relation (Eqn. Eqn. 2.9). pH of the bulk electrolyte is a parameter here that can be controlled externally which affects the NW sensor conductance by modulating the surface charge density.

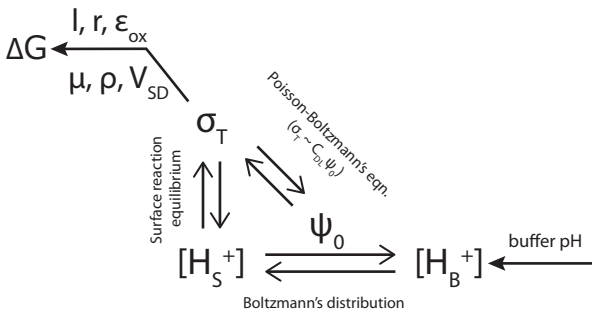

Figure 2.3.: The equations governing the relation between the pH of bulk electrolyte, a parameter that is controlled externally and the surface charge, σ_T which influences the NW conductance, a measured quantity. $\left[H_B^+\right]$ or pH of the bulk electrolyte is an external controlled parameter while ΔG is the response of the NW sensor.

2.3. Capacitances in the system

In this section we present the various capacitances in the system and their relevance to the interaction of the voltages applied to the back gate (liquid gate) as well the coupling of the surface charge density with mobile ions in solution.

Voltage applied to the back gate/liquid gate can change the density ρ of the charge carriers in the NW via the corresponding capacitive coupling, C_{BG}/C_{LG}. The equivalent circuit with the relevant capacitances is shown in Fig. 2.1 b. The resulting charges at the oxide-electrolyte interface due to the reaction of the hydroxyl groups (σ_T) are balanced by charge induced in in the double layer (σ_{DL}) and charge induced

in the NW (σ_{NW}). Electrical neutrality relates the three charge densities as,

$$-\sigma_T = \sigma_{NW} + \sigma_{DL} \tag{2.10}$$

σ_{NW} depends on the capacitance of the oxide as[88],

$$\sigma_{NW} = -C_{ox}\psi_0 = -\frac{2\pi\epsilon_{ox}\epsilon_0}{\cosh^{-1}\left[1+\frac{t_{ox}}{r_{nw}}\right]}\psi_0 \tag{2.11}$$

where C_{ox} is the capacitance of the cylindrical shell of oxide isolation around the NW, ϵ_{ox} is the relative permittivity of the oxide, ϵ_0 vacuum permittivity, t_{ox} the thickness of the oxide layer and r_{nw} the radius of the nanowire. σ_T and σ_{DL} form a capacitor referred to as the double layer capacitance, C_{DL}, discussed further on. The ratio in which the surface charge density is balanced between the NW and the double layer depends on the ratio of the capacitances. C_{DL} is typically around $0.2\,\mathrm{F/m^{-2}}$ and thus for a wire of length ~1 μm and diameter 100 nm this capacitance is of the order 10^{-14} F. In comparison the typical back gate capacitance C_{BG} to a NW of length 1 μm and oxide thickness $t_{ox} \sim 50$ nm is of the order 10^{-16} F[88]. With C_{DL} orders of magnitude larger than C_{ox}, σ_{NW} is much smaller compared to σ_{DL}. The charge balance can thus be written as,

$$\sigma_T \approx -\sigma_{DL} \tag{2.12}$$

Since C_{DL} is the differential capacitance of the double layer, defined as the latter's ability to store charge in response to a change in the surface potential, it can be expressed as,

$$C_{DL} = \frac{d\sigma_T}{d\psi_0} \tag{2.13}$$

Differentiating Eqn. Eqn. 2.8 we get,

$$\frac{1}{C_{DL}} = \frac{d\psi_0}{d\sigma_T} = \frac{1}{C_{Stern}} + \frac{2k_bT}{e}\frac{1}{\sqrt{\sigma^2 + 8k_bT\epsilon_W\, c}} \tag{2.14}$$

The double layer capacitance can be seen as composed to two capacitors in series, C_{Stern} and the diffuse layer capacitance, C_D. For typical buffer compositions with salt concentration, $c \sim 100$ mM, we can neglect the second term on the R.H.S and use $C_{DL} \sim C_{Stern}$. Even deviations at low salt concentrations becomes irrelevant for a large density of surface sites at the oxide-buffer interface ($\sim 10^{18}\, m^{-2}$). This assumption is explored further in Sec. 2.4.3.

With reference to Fig. 2.1 b, the drop in voltage applied to the liquid gate electrode V_{LG} across C_{DL} is $\propto \frac{C_{ox}}{C_{ox}+C_{DL}}$ and since $C_{DL} \gg C_{ox}$ the voltage drop across C_{DL} is negligible and most of the applied V_{LG} appears at the oxide surface. Thus if we assume a change in the surface potential $\Delta\psi_0$ due to reaction of the surface terminal groups and define ΔV_{LG} as the liquid gate potential needed to compensate $\Delta\psi_0$ keeping the current/conductance constant, then [75]

$$\Delta\psi_0 \approx \Delta V_{LG} \tag{2.15}$$

In other words, ΔV_{LG} is a direct measure of $\Delta\psi_0$. Both the back gate and the liquid gate can tune the charge carrier density ρ in the NW through their respective capacitive coupling (C_{BG}, C_{LG}). Voltage applied to the back gate ΔV_{BG} can also be used to estimate $\Delta\psi_0$ as,

$$\begin{aligned} C_{BG}\Delta V_{BG} &= C_{ox}\Delta V_{LG} \\ \therefore \Delta\psi_0 \approx \Delta V_{LG} &= \Delta V_{BG}\,\frac{C_{BG}}{C_{ox}} \end{aligned} \tag{2.16}$$

There can be significant differences between the analytically estimated and experimentally measured values of the back gate capacitive coupling to the NW due to fringe fields. Accurate numerical estimates can be made by solving three dimensional Poisson's equations [88]. For this reason it is not easy to convert a change in back gate potential, $\Delta \mathrm{V_{BG}}$ to $\Delta\psi_0$. Having established the interplay between the gates, surface potential and H^+ ions in solution, we examine the pH response and sensitivity of the sensor in the next section.

2.4. pH Sensitivity

Intrinsic sensitivity of a pH sensor can be defined as the change of surface potential (ψ_0) per decade change of the bulk proton concentration (pH_B), i.e., $\frac{\mathrm{d}\psi_0}{\mathrm{dpH}}$. This quantity is found to depend on factors such as terminal group density, reactivity and electrolyte composition. The transduction of the surface potential into a change in current/conductance of the NW FET sensor is further influenced by factors such as the insulation capacitance (C_{ox}), dimensions of the FET (length, diameter), carrier density (ρ) as discussed in Sec. 2.1 and Eqn Eqn. 2.11. The aim of this section is to derive a simplified relation between the surface potential ψ_0 and pH of the bulk electrolyte pH_B.

We defining, $\alpha_0 = \frac{\sigma_T}{eN_S}$ and $\delta = 2\sqrt{\frac{K_a}{K_b}}$. α_0 represents the ratio of the surface charge density to the maximum value of the same, i.e, total number of terminal groups times the electron charge. For typical oxide surfaces such as SiO_2, Al_2O_3, etc surface density of hydroxyl groups, N_s is large, ~10^{18} - 10^{19}/$m^2$and for usual aqueous solutions with pH between 4 and 10, this ratio is around ~0.1. At low N_s a larger percentage of the hydroxyl groups are protonated/deprotonated and this ratio is higher. Thus, solving Eqn Eqn. 2.5 -Eqn. 2.9 and substituting α_0 and δ, we can relate $\left[H_B^+\right]$ to ψ_0,

$$[H_B^+] = \sqrt{K_a K_b}\, \exp\left[\frac{e\psi_0}{k_b T}\right] \frac{\left(\frac{\alpha_0}{\delta} + \sqrt{1 + \left(\frac{\alpha_0}{\delta}\right)^2 (1-\delta^2)}\right)}{1-\alpha_0} \tag{2.17}$$

Substituting $\mathrm{pH_{pzc}}$= ($\mathrm{pK_a}$+$\mathrm{pK_b}$)/2 and rearranging, we get,

$$\ln 10 \cdot (pH_{pzc} - pH_B) = \frac{e\psi_0}{k_b T} + \log\left[\frac{\alpha_0}{\delta} + \sqrt{1 + \left(\frac{\alpha_0}{\delta}\right)^2 (1-\delta^2)}\right] - \log[1-\alpha_0] \tag{2.18}$$

For small $\frac{\alpha_0}{\delta}$, the second term on the right hand side (RHS) can be reduced to $\log\left[1 + \frac{\alpha_0}{\delta}\right] \sim \frac{\alpha_0}{\delta}$. Similarly, for typical values[68] $\alpha_0 \ll 1$ and thus the third term

on the RHS can be neglected. Expanding α_0,

$$\ln 10 \cdot (pH_{zc} - pH_B) = \frac{e\psi_0}{k_bT} + \frac{C_{DL}\psi_0}{eN_S\delta} \tag{2.19}$$

Defining, $\beta = \frac{e^2 N_S \delta}{C_{DL} k_b T}$, a term dependent on the material properties of the surface (N_S, δ) and electrolyte composition (C_{DL}) and independent of the pH_B,

$$\psi_0 = \ln 10 \cdot \frac{k_bT}{e} \frac{\beta}{\beta + 1} (pH_{zc} - pH_B) \tag{2.20}$$

Thus, with some assumptions the surface potential response with changing $\mathrm{pH_B}$ can be linearized. The effect of the material properties of the surface (N_S, K_a, K_b) as well as the electrolyte composition (C_{DL}) on the pH sensitivity ($d\psi_0/dpH_B$) of surface potential change is examined in the following subsections.

2.4.1. pH sensitivity: Effect of the density of surface terminal groups ($\mathrm{N_S}$)

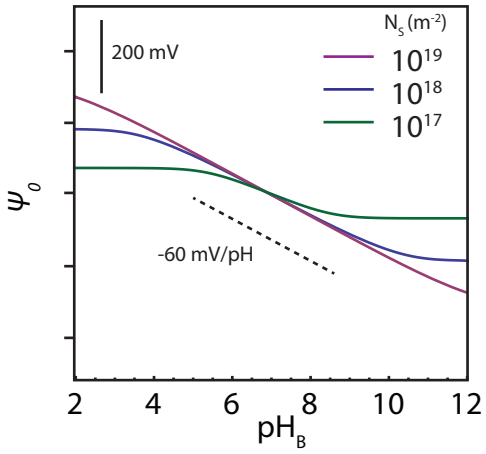

Figure 2.4.: Effect of surface hydroxyl group density, N_S on ψ_0 response at different pH_B using Eqn. 2.18. This is assuming $pK_a = pK_b = 7$. The dashed offset line indicates the maximum Nernstian response of $\sim -60\,\mathrm{mV/pH}$. This figure reproduces the results shown by Tarasov et al[68].

Terminal group density, N_s is the number of reactive sites per unit area at the sensor surface. Its impact on the sensor pH response (See Van den Berg et al[89]) depicted in Fig. 2.4 shows that N_s has a significant influence on the ψ_0-pH_B trace. The shape of this trace varies from a linear Nernstian response of 60 mV/pH at large $N_s \sim 10^{19}\,\mathrm{m}^{-2}$ to a sigmoidal shape at lower $N_s \sim 10^{17}\,\mathrm{m}^{-2}$ saturating at pH values far from the pH_{pzc}. Typically the upper limit for N_s, set by the inter atomic bonding distances in the insulator, is around $10^{19}\,\mathrm{m}^{-2}$. It can be seen from Eqn. Eqn. 2.20 that $\left|\frac{\partial\psi_0}{\partial pH_B}\right| = 2.303\,\frac{k_bT}{e}\frac{\beta}{\beta+1}$. For $\beta \gg 1$, $\left|\frac{\partial\psi_0}{\partial pH_B}\right|$ reduces to the expected maximum Nernstian value of ~ 59.9 mV/pH at 300 K. A limited pH response can be seen arising due to the dimensionless parameter β, which in turn depends on the properties of oxide at the interface, specifically the surface site density, N_S and δ through the protonation/deprotonation equilibrium constants, K_a and K_b. For $N_S = 10^{18}\,\mathrm{m}^{-2}$ and $\delta = 2$, $\beta/\beta + 1 \approx 0.98$. Practically, at pH_{pzc} the surface is neutral with the highest number of unreacted terminal groups and is thus most reactive. pH sensitivity of the sensor close to pH_{pzc} is the largest. For low to moderate $N_s < 10^{18}\,\mathrm{m}^{-2}$, increasing deviation from the pH_{pzc} decreases the total number of available reactive terminal groups since the latter react and exist in their charged protonated/de-protonated state, depending on if the pH increases or decreases w.r.t the pH_{pzc}. Thus the saturation of the ψ_0-pH_B trace can be understood as decreasing density of available reactive groups. On the other hand, at high $N_s > 10^{18}\,\mathrm{m}^{-2}$ the surface potential response remains linear over the entire pH range. Insulators such as Ta_2O_5, Al_2O_3 are known to have large number of surface site groups in comparison to materials such as SiO_2 and have been observed[86] to be more pH sensitive experimentally. Contamination of the sensor surface can reduce N_s and consequently the pH sensitivity. Oxygen plasma cleaning (descum) can be used to regenerate surface hydroxyl groups.

2.4.2. pH sensitivity: Effect of surface reactivity ($\mathbf{pK_a}, \mathbf{pK_b}$)

The equilibrium constants K_a, K_b represent the reactivities of the terminal group with the protons close to the surface. It is easy to see that for small reactivities, for a given change in the bulk pH (pH_B), there would be a smaller change in the surface charge and hence a smaller $\Delta\psi_0$. The ratio of the two constants appears in β as $\delta = 2\sqrt{\frac{K_a}{K_b}}$ in the numerator. A larger value would imply a larger sensitivity. SiO_2 has been found to show sensitivities of ~30-40 mV/pH[81,82]. $pK_a - pK_b$ for

the same have been determined to be as large as ~8[89], implying a small δ. Al_2O_3, HfO_2 on the hand, have $\delta \sim 1$ with smaller differences in reactivity constants ($pK_a - pK_b$~1-2[69,84]) and have been found to show near Nernstian response of the surface potential. Values for these constants for typically used insulators are presented in[86]. Reactivities and surface site densities of the oxide have been shown to be modified by thermal treatment[89–91]. In the context of our experiments, a shift in the point of maximum pH sensitivity upon chemical modification of the surface is observed and this indicates a change in the surface reactivity due to the change in the terminal groups. Examining the parameter $\beta = \frac{e^2 N_S \delta}{C_{DL} k_b T}$ it can be seen that N_s which can vary by orders of magnitude for different materials will have a larger impact than than δ which has a smaller comparative variation between materials.

2.4.3. pH sensitivity: Effect of electrolyte salt composition

It was shown in Sec. 2.4.3 that the double layer system can be modeled according to the Gouy-Chapman-Stern theory as a combination of two capacitors, the Stern capacitance (C_{Stern}) and the diffuse layer capacitance (C_{DL}) in series. It was then stated that at the typical compositions of buffered solutions, $C_{DL} \approx C_{Stern}$. Here we shall briefly examine this assumption. From Eqn Eqn. 2.3 we have,

$$\begin{aligned} \frac{1}{C_{DL}} &= \frac{1}{C_{Stern}} + \frac{1}{C_D} \\ &= \frac{1}{C_{Stern}} + \frac{2k_bT}{e} \frac{1}{\sqrt{\sigma^2 + 8k_bT\epsilon_W c}} \end{aligned} \tag{2.21}$$

The variation of C_{DL} with pH of the bulk buffer is plotted in Fig. 2.5 and shows the deviation of C_{DL} from C_{Stern} close to pH_{zc}. For salt concentrations above 100 mM, the second term on the RHS of Eqn. Eqn. 2.21 is negligible compared to $1/C_{DL}$ and the Stern capacitance dominates. For lower electrolyte concentrations we cannot neglect the contribution of the diffuse layer capacitance (second term).

Physically, the double layer capacitance describes the ability of the double layer to store charge in response to a potential. As the electrolyte concentration decreases, the length over which the surface charges induce a potential (Debye length, see Sec. 2.6.1) increases leading to a expansion of the diffuse layer and consequently

the diffuse layer capacitance becomes smaller and more comparable to the Stern capacitance. This effect is observed in Fig. 2.6 as an increasing mismatch between predicted $\psi_0 - pH_B$ curves for constant (red) and variable (blue) C_{DL} assumption ($N_s = 10^{17}\,\mathrm{m}^{-2}$). However, at a large enough N_S, variable capacitance yields no difference from the constant capacitance assumption. This is because for large density of reactive terminal groups, even with protonation/de-protonation there are sufficient numbers of reactive hydroxyl groups available far from pH_{pzc} and thus ψ_0 remains linear over nearly the entire pH range (typically 4 - 10). Analytically, this is seen in the dependence of the prefactor in Eqn. Eqn. 2.20 on C_{DL} which becomes irrelevant at large N_S since $\frac{\beta}{\beta+1} \sim 1$. We further analyse the role of the ionic species on the sensor response in Sec. 2.5.

An interesting consequence of the Boltzmann's distribution due to the potential profile resulting from the surface charge distribution is that the pH of the bulk electrolyte is not the same as the pH of the local environment close to the oxide surface (Fig. 2.7). The exact relation between surface charge density and $[H_s^+]$ depends on the model (site binding, etc) used. Taking the logarithm and differentiating Eqn. Eqn. 2.9 we get, $\frac{dpH_s}{dpH_B} = 1 + \frac{e}{2.303\,k_bT}\frac{d\psi_0}{dpH_B}$. For large surface site densities, sub-

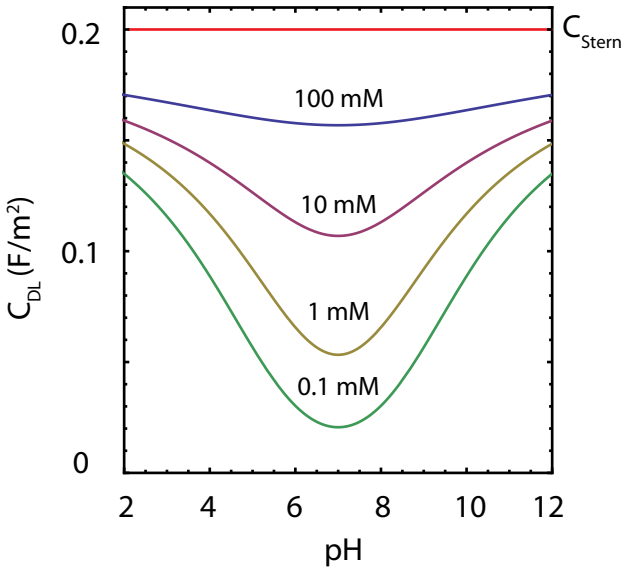

Figure 2.5.: Deviation of the overall double layer capacitance from the Stern capacitance (~0.2 F/m^2,red trace) as a function of bulk pH of the buffer for different electrolyte concentrations (colours). The plot is made assuming $pK_a = pK_b = 7$ and $N_S = 10^{18}\,\mathrm{m}^{-2}$.

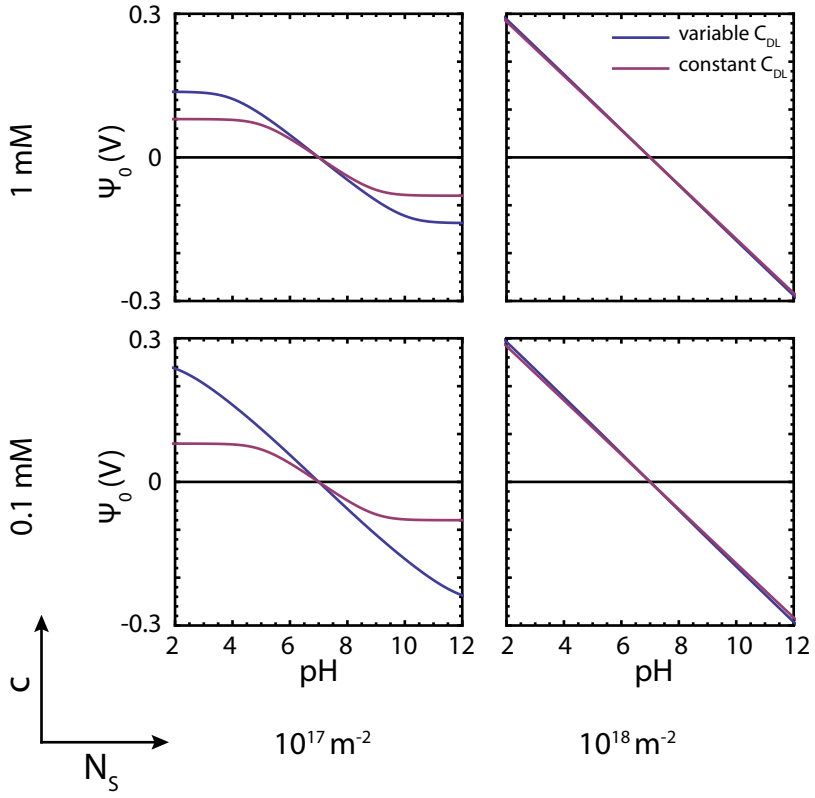

Figure 2.6.: Calculated surface potential, ψ_0 with and without the assumption of C_{DL} for different salt concentrations (c) and surface site densities (N_S) assuming $pK_a = pK_b = 7$.

stituting $\frac{d\psi_0}{dpH_B} = 59.9\,\text{mV/pH}$, we get $\frac{dpH_s}{dpH_B}$ =0.005. This implies that large changes in the bulk pH (pH_B) only lead to small variations in the pH close to the surface (pH_s). Physically, this is expected as large surface terminal group densities are able to buffer changes in the local pH.

Finally we discuss another consequence of the electrolyte composition on the sensor response. Van Kerkhof et al[92] performed an experiment wherein solutions of varying compositions are flushed over an ISFET and the time dependent sensor response was recorded. The salt concentration of the solutions was varied while pH was maintained constant. The authors observed a spike and a subsequent transient response following the solution exchange. The transient response shown in Fig. 2.8 was described as resulting from the diffusion limited equilibration of $[H^+]$. Decreasing the electrolyte concentration would immediately decrease double layer capacitance, C_{DL} (See Eqn. Eqn. 2.21). Referring to Fig. 2.3, it can be seen that a

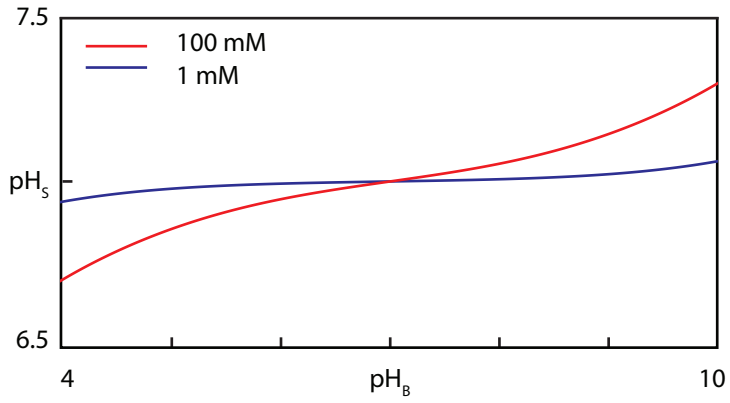

Figure 2.7.: Using the simple site binding model, the pH close to the oxide surface, pH_s is calculated as a function of the bulk electrolyte pH (pH_B) at two different electrolyte concentrations.

change in C_{DL} would effect the surface potential, ψ_0, and since the pH_B remains the same, the surface charge distribution σ would have to adapt. The time constant for this process is limited by the diffusion of $[H^+]$ ions to the surface and the buffer capacity of the electrolyte. The system is modeled numerically by the authors using a combination of Nernst-Planck equations and the Poisson's equation. The former is a mass balance equation that describes the motion of ions in response to an ionic gradient as well as an electric field. Poisson's equation describes the variation of potential given a spatial distribution of charge. Experimentally it was observed that the amplitude of the spike following transient solution exchange notably decreased on switching to a pH buffered electrolyte from an aqueous solution with pH adjusted with KOH/HCl. Upon increasing the electrolyte concentration (KCl) of the buffer, the transient response decreases due to a smaller change in C_{DL}. This is a useful analysis of the system relevant to our system as we observe a transient sensor response using pH adjusted (KOH/HCl) aqueous solutions (See Sec. 4.1.1) which not observed upon using pH buffered solutions (Sec. 4.2).

2.5. Surface Complexation: Role of the anion

In this section we discuss the effect of the solution composition on the sensitivity of pH response of the sensor (Sec. 4.2.3) and use the proposed model to analyse the sensitivity of our sensor at different buffer dilutions. Recently, Tarasov et al [69]

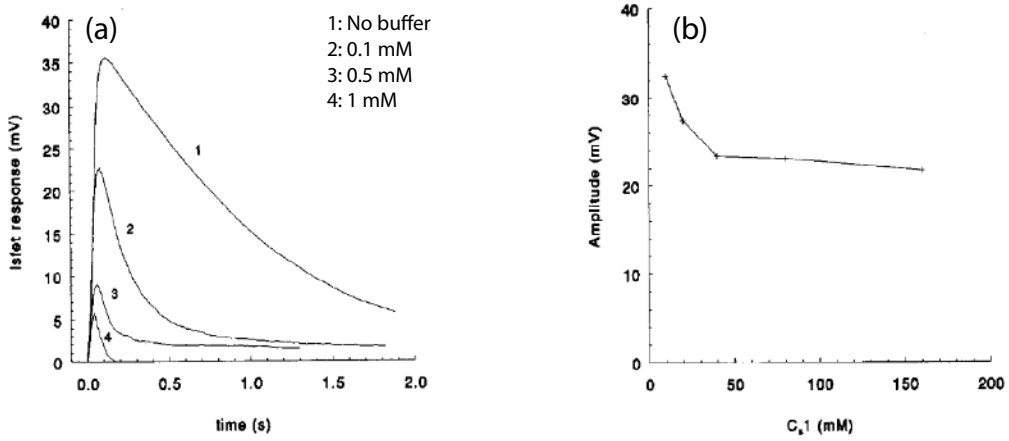

Figure 2.8.: Figures reproduced from Van Kerkhof et al[92]. (a) Spikes in the response of a planar ISFET coated with Ta_2O_5 for an ion step of 10 to 50 mM KCL in different TRIS concentrations. All solutions had a pH of 8.3. (b) The amplitude of the step response for an ion step from c_s1 to $5 \times c_s1$ is plotted as a function of the initial KCl concentration (c_s1) all made in unbuffered solutions.

examined the role the electrolyte salt concentration c on the response of a NW based pH sensor. They find device sensitivity $\left(\frac{d\psi_0}{dpH}\right)$ to be around 56 mV/pH and independent of the salt (KCl) concentration, the latter varied between 10 mM and 1 M. They explore several models (Fig. 2.9 a-c) and find them to be insufficient in describing their experimentally observed dependence of ψ_0 on c. An alternative model (model and fit to the data shown in Fig. 2.9 d-e) is proposed which involves complexation of the anion (in this case Cl^-) with the protonated hydroxyl groups at the oxide-electrolyte interface with a equilibrium constant, K_c

$$[I - OH_2^+] + [Cl_s^-] \overset{K_c}{\rightleftharpoons} [I - OHCl^-] + [H_B^+],\ K_c = \frac{[I - OHCl^-][H_B^+]}{[I - OH_2^+][Cl_s^-]} \tag{2.22}$$

where the $[X]$ corresponds to the molar concentration of an ionic species, the subscript (s, b) indicates if it is a local or bulk concentration. Assuming surface properties such as $pK_a = pK_b = 7$ and $N_s = 10^{19}\,\mathrm{m}^{-2}$ from earlier measurements on similar devices as well as a constant double layer capacitance, they show a good agreement between the proposed model and data. In order to implement the model to numerically (or analytically) simulate the effect of the salt concentration on the

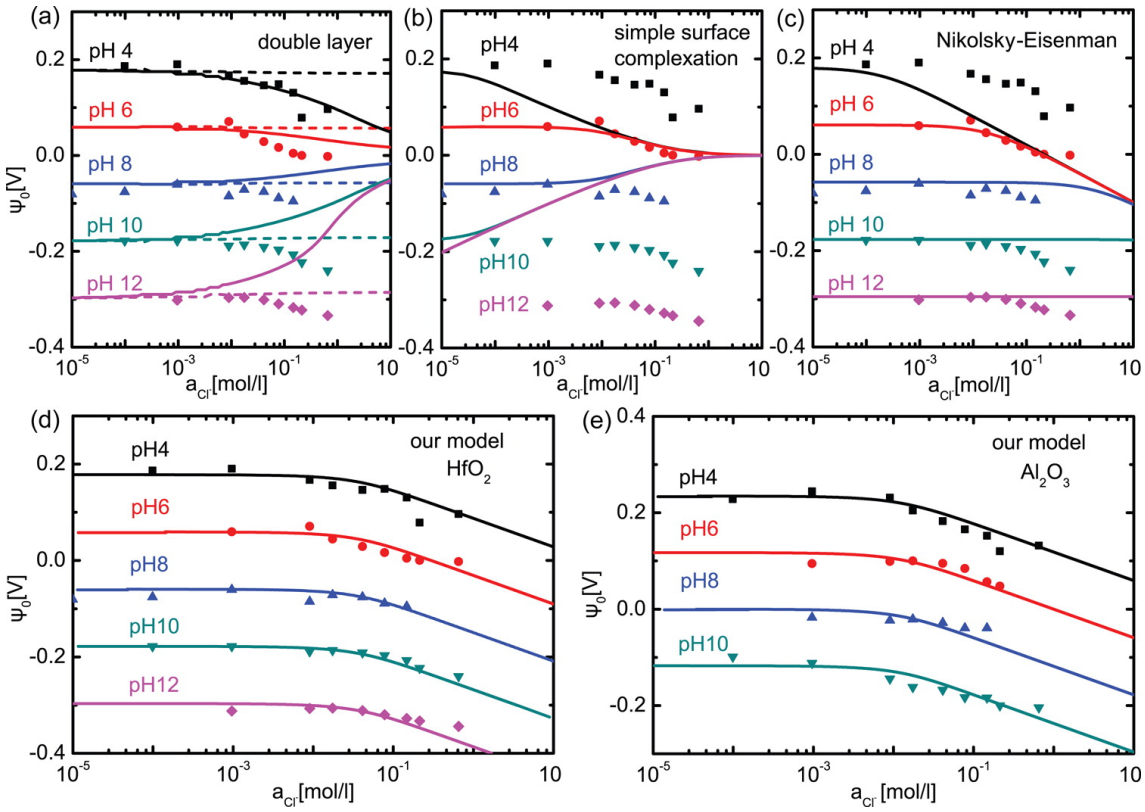

Figure 2.9.: Figure reproduced in its entirety from Tarasov et al[69]. The coloured squares correspond to experimental points and the lines correspond to the best fit according to a specific model. (a) Site binding model. (b) Simple surface complexation. (c) Nikolsky-Eisenman model. (d) Proposed model with Al_2O_3 insulation and (e) HfO_2 insulation.

surface potential, equations Eqn. Eqn. 2.3 -Eqn. 2.4 are modified as,

$$\begin{aligned} N_S &= [I-OH_2^+] + [I-O^-] + [I-OH] + [I-OHCl^-] \\ \sigma_T &= q\left[[I-OH_2^+] - [I-O^-] - [I-OHCl^-]\right] \end{aligned} \tag{2.23}$$

along with the Boltzmann relation for bulk and surface chloride ion concentration,

$$\left[Cl_S^-\right] = \left[Cl_B^-\right] \cdot \exp\left(\frac{e\psi_0}{k_b T}\right) \tag{2.24}$$

The equations can be solved analytically, assuming a constant double layer capacitance, $C_{DL} = C_{Stern}$ with $\sigma_T = C_{Stern}\psi_0$. As discussed in Sec. 2.4.3, for large N_s ($> 10^{18}/\mathrm{m}^2$) changing c has little effect on C_{DL} as σ_T remains small. However, at

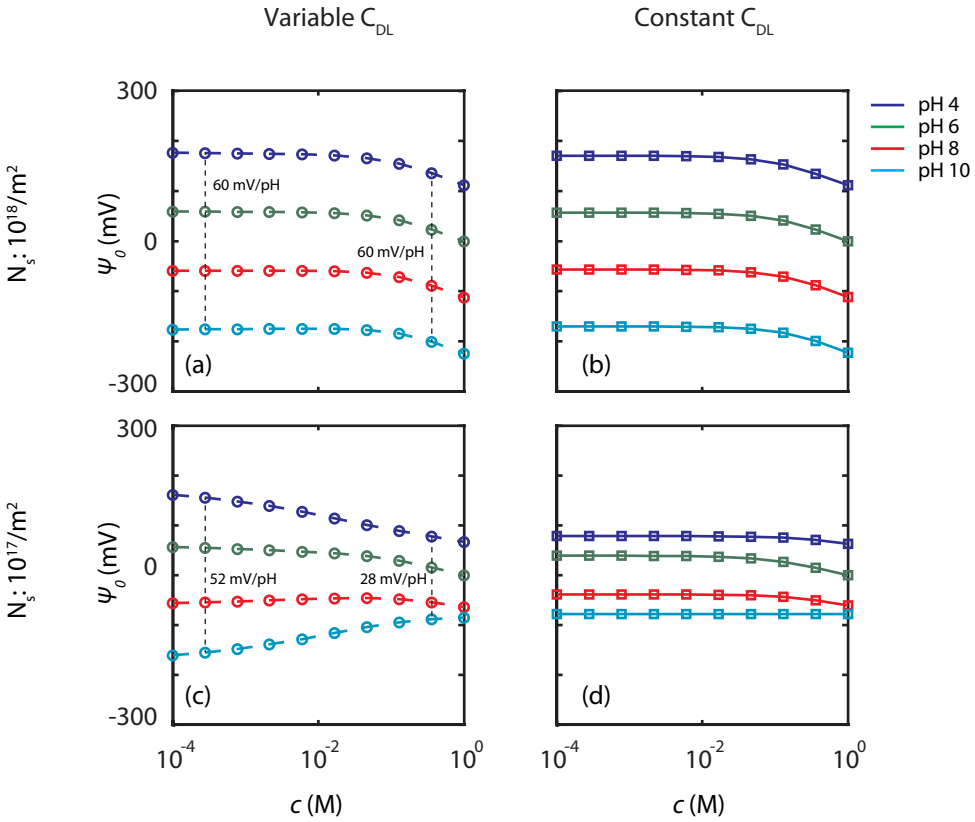

Figure 2.10.: Numerical solution of the surface potential, ψ_0 as a function electrolyte concentration, c for different buffer pH values (colours) using the site binding model (SBM) and anion complexation. Solutions for both the constant and variable double layer capacitance (C_{DL}) are shown for surface site densities, $N_s = 10^{17}$ and $10^{18}\,\mathrm{m}^{-2}$. Vertical black dashed lines in (a) and (c) show the sensor sensitivities.

lower N_S this assumption predicts lower than observed (see Sec. 4.2.3) sensor sensitivities $\left(\frac{d\psi_0}{dpH}\right)$ with a weak dependence on c. Using Eqn. Eqn. 2.8 to relate σ_{T} and ψ_0, the proposed model can be numerically solved for different N_s. Fig. 2.10 shows the result of the numerical solution for $N_S = 10^{17}\,\mathrm{m}^{-2}$ and $10^{18}\,\mathrm{m}^{-2}$ for both the constant and variable C_{DL} assumption. As expected, for large N_s (Fig. 2.10 a-b) the solution shows no difference between the constant and variable C_{DL} assumption and matches the prediction of the original article. The sensor shows a sensitivity of $\sim 60\,\mathrm{mV/pH}$ for all electrolyte concentrations. However, for a smallerN_s (Fig. 2.10 c-d) we see a visible difference arise for $c < 0.1$ M. The model predicts increasing sensor sensitivity with decreasing electrolyte concentration. As a concluding remark it is interesting to note that though the model is able to correctly predict the exper-

imental observation of ψ_0 with changing ionic concentration c, the model presented in Eqn. Eqn. 2.22 is not strictly correct. The reaction constant K_c should relate the local activities or concentration of the species involved in the reaction. Thus $K_c^* = \frac{[I{-}OHCl^-][H_s^+]}{[I{-}OH_2^+][Cl_s^-]}$ would be a true thermodynamic constant only varying with temperature while the constant proposed by the model, K_c would depend on the surface potential ψ_0. The validity of the model can be further explored and compared to the results shown in Fig. 2.10 by using pH sensors with lowered density of surface groups already demonstrated by the authors via vapour phase silanization [68].

2.6. Protein Sensing

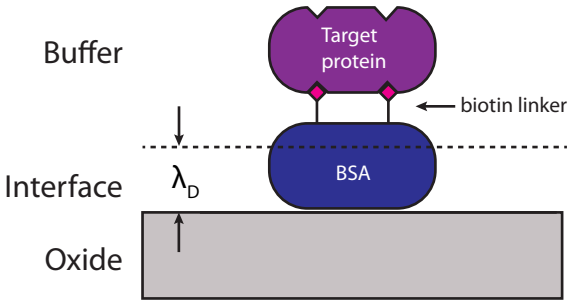

Figure 2.11.: A model scheme involving biotinylated bovine serum albumin (BSA) as a functional layer followed by Streptavidin as a target protein for detection. The Debye length (λ_D) for the electrolyte concentration of the buffer is depicted by the dashed line.

Fig. 2.11 shows a simplified scheme for protein detection employed by us and is discussed in chapter 5. Typically the sensor surface is functionalized with a recognition element that allows specific binding to the molecule of interest (proteins, DNA, etc). The Debye length λ_D is a relevant electrostatic length scale in aqueous systems with mobile charged ions and for large bio-molecules (up to tens of nm) typically both the recognition element and the target molecule have sizes comparable to λ_D. This makes the spatial charge distribution within the target molecule an important consideration when analyzing the sensor response.

2.6.1. Debye Length

The Debye length is an important length scale in electrolyte solution describing the fall in potential with distance r from a charge. Due the presence of mobile ions, any charged species in solution will be surrounded by counter ions negating the electric field from the original charge. For comparison the potential distribution $V(r)$ due to a charge q both in vacuum as well as in solution with ionic screening is presented,

$$V(r) = \frac{q}{4\pi\kappa\epsilon_0}\frac{1}{r} \tag{2.25}$$

$$V(r) = \frac{q}{4\pi\kappa\epsilon_0}\frac{\exp(-r/\lambda_D)}{r},\ \lambda_D = \frac{1}{\sqrt{\frac{e^2}{\epsilon_w\epsilon_0 k_b T}\sum z_i^2 n_i}} \tag{2.26}$$

where ϵ_w is the dielectric constant of the solution, z_i and n_i are are valence and number density of the ionic species i in solution and the other symbols have their usual meaning. As seen in Eqn. Eqn. 2.25 -Eqn. 2.26, electrostatic screening due to counter ions leads to an exponential damping in the potential and beyond $r \gg \lambda_D$ the original charge is 'invisible', being screened out. As an example, a PBS buffer with an ionic concentration of 150 mM KCl has $\lambda_D \sim 0.7$ nm.

Protonation/de-protonation reactions at the sensor surface discussed earlier, involve protons ($[H^+]$) and surface hydroxyl groups $[I-OH]$. Debye screening in this case is not relevant since both the target species and the reactive surface elements have sizes in the order of Å, much smaller than typical λ_D in physiologically similar buffer solutions. On the other hand, biomolecules such as proteins, antigens and DNA strands can have dimensions up to a few tens of nm and for λ_D much smaller than the protein, the binding of the molecule may not be transduced into a response from the sensor since the charge will be screened. While for λ_D comparable to the protein size, it may not be sufficient to consider the simplified model of the protein as a single point charge binding at a fixed distance from the surface[94]. Lloret et al[93] examine the importance of choosing the correct buffer composition and dilution for a given detection scheme when using NWs as biosensors. Fig. 2.12 shows a plot of λ_D as a function of ionic strength of the buffer along with the sizes of some well known proteins (Streptavidin, monoclonal antibody), thus schematically depicting the need to select a sufficiently large λ_D based on the size of the protein system

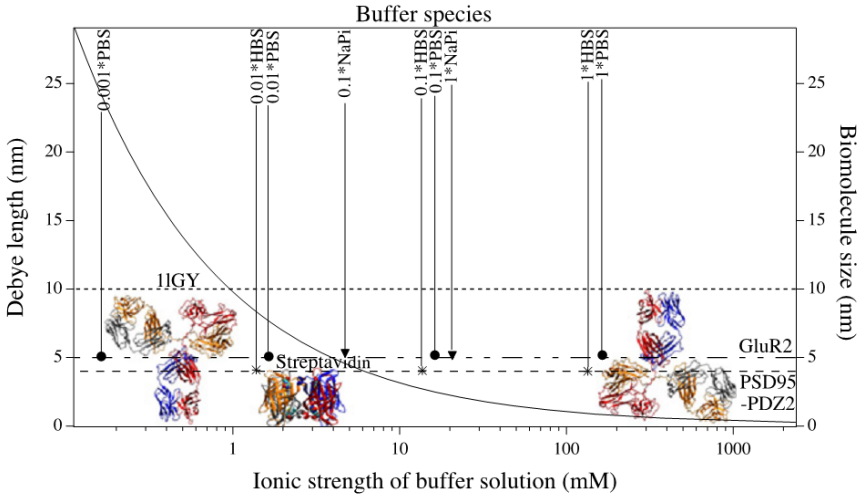

Figure 2.12.: Figure reproduced from Lloret et al[93] shows the variation of λ_D with the ionic concentration in the buffer. Representation of the sizes of a few select proteins has been overlaid for comparison.

involved .

Stern et al[26] explored the influence of λ_D on the magnitude of sensor response. Fig. 2.13 a shows the scheme employed - biotinylated sensor surface as the recognition motif and Streptavidin as the target molecule. After the incubation of Streptavidin, a time trace of the current through the sensor is recorded for increasing ionic concentration in the buffer. At the highest dilution (0.01X in Fig. 2.13 b, $\lambda_D \sim 2.3\,\text{nm}$) a marked sensor response is visible. The sensor is based on a *p*-type NW and thus negatively charged Streptavidin should result in a overall increase in current. Upon flushing buffer solutions of increasing ionic concentration (decreasing λ_D or dilution), the sensor response is seen to decrease with respect to the original current baseline and at the lowest dilution (1X, $\lambda_D \sim 0.7\,\text{nm}$) the response is much smaller due to the fact that most of the protein charge is screened. In addition, in a separate control experiment they demonstrate that the change ionic concentrations does not affect the sensor current. They thus demonstrate that in order for the binding of a charged molecule to contribute to the sensor response the Debye length must be carefully tuned to match the size and the binding distance of the target species. Diluting a buffer for a larger λ_D may not always be an option in the case where protein function and binding is affected at lower ionic strengths.

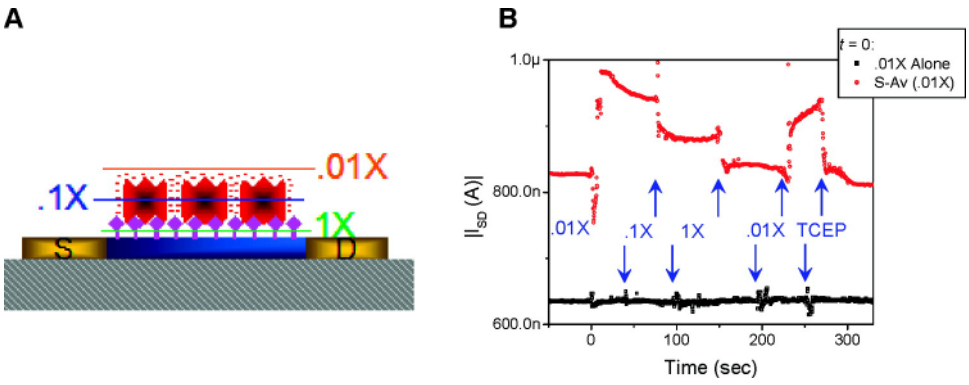

Figure 2.13.: Figure reproduced from Stern et al[26] (a) Schematic depiction of the biotinylated NW sensor surface and the binding of Streptavidin. λ_D at three different buffer dilutions are indicated (green, blue and orange lines) (b) The response of a sensor based on a p type NW to changing buffer dilutions. TCEP added in the last step is used to cleave the biotin linkers. Streptavidin is negatively charged at the pH used

While Stern et al[26] qualitatively showed the importance of tuning λ_D depending on the system, De Vico et al[94] quantitatively explore the distribution of charges within the protein and the sensor response as a function of λ_D. For some proteins crystallographic structural data exists and the relevant structural files from protein data banks (pdb) can give the spatial distribution of amino and carboxyl groups within the protein. With knowledge of the pKa's of the these groups an accurate spatial distribution of charges can be obtained[94]. For λ_D comparable to protein size, charges closer to the sensor surface will play a larger role in the sensor response. This methodology[95] provides an effective tool to understand and predict the electrostatics of protein interactions with the sensor surface but is limited by the lack of knowledge of protein orientation at the surface.

2.7. Conclusions

In conclusion, we explain the underlying principle of an FET based pH and biological sensor as a transduction of charges at the surface into a change in the current via electrostatic interaction. Sensitivity to the pH was presented arising out of the protonation and de-protonation reactions of the terminal groups at the sensor surface. A large density of these groups would thus make the surface more reactive (sensitive) over a larger pH range. We presented a picture of the various interlinked equilibrium mechanisms that link the pH of the bulk solution to the surface charge density. The role of the background ions in solution is discussed with respect to the double layer capacitance as well as anion complexation at the surface. The limitations of model for the latter are discussed along with a proposal to further explore the same experimentally. The analysis discussed till now is mainly for the equilibrium situation and though it does not shed light on the dynamics of diffusion and reaction, it is sufficient in describing the observations shown in the subsequent chapters. We have presented our scheme for the electrical detection of proteins. Compared to H^+ ions, proteins are larger in size and often comparable to the Debye length. Detection of the protein charge at the surface can thus be limited by electrostatic screening. We discuss a method used to overcome this limitation experimentally as well as the possibility to quantitatively model the sensor response using the spatial distribution of charges within the protein.

3. Materials and Fabrications

Starting with NWs grown via molecular beam epitaxy (MBE) in an ultrahigh vacuum chamber, this chapter first provides an overview of two terminal nanowire device fabrication utilizing both ultraviolet light as well as electron beam lithography. We discuss electrical isolation and surface functionalization and finally present the fluidic setup used in the sensor experiments. The NWs presented in this thesis were grown by P. Krogstrup and M. H. Madsen.

3.1. Indium Arsenide

InAs is a group III-V semiconductor known for its small band gap (0.34 eV) and high electron mobility of up to $30000\,\mathrm{cm^2/V\,s}$ in bulk and $2000 - 3000\,\mathrm{cm^2/V\,s}$ in NWs at room temperature[57,58]. Its unique property of a surface electron accumulation layer makes it appealing as a choice of material for the sensor. Dangling arsenic bonds and adsorbed hydrogen atoms at the surface lead[96] to donor like states at the surface, which are neutral when filled and positive when empty. As seen in Fig. 3.1 a, electrons from such states relax into the conduction band near the surface leaving behind now ionized donor states. Somewhat analogous to a semiconductor p-n junction at equilibrium, the redistribution of electrons leads to an electric field resulting in band bending. The large number of these donor states ensure that the Fermi level remains pinned at the surface above the conduction band minimum and a peak in electron density close to the surface, Fig. 3.1 b. This allows for electrical contact across the metal-semiconductor interface to be free of Schottky barriers unlike most other semiconductors. Since the NW sensor involves detecting interactions at its surface, Fig. 3.1 c, the surface accumulation layer should ensure that most of the conducting electrons lie within the influence of the surface charge (Thomas-Fermi length) and thus be more sensitive. Schematically, the surface electron layer can be visualized by contrasting the electron distribution in the cross-section of a n-doped

Si and InAs NW. InAs can be electron or hole doped (n or p) during growth which can be used to further tune the charge carrier profile within the NW. Fig. 3.1 c shows this profile in a p-doped InAs NW and is analyzed in chapter 6.

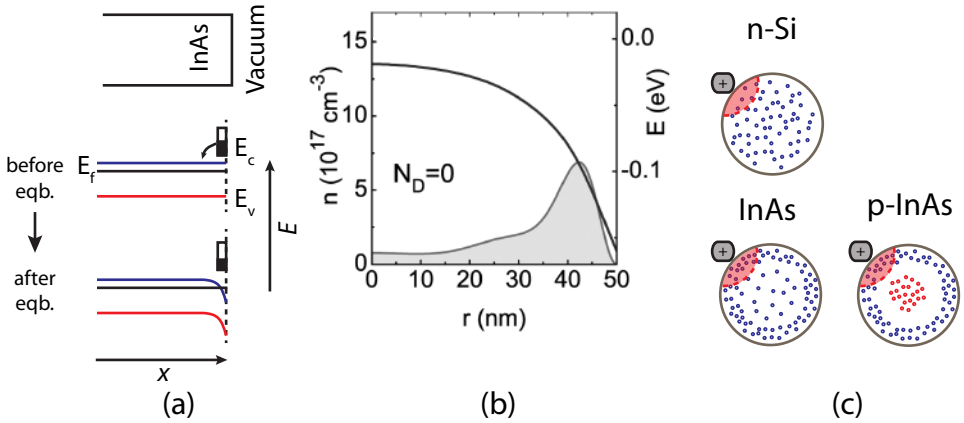

Figure 3.1.: (a) Schematic depiction of the surface band bending leading to the conduction band minimum at the surface lying below the Fermi level due to the surface states (b) Figure taken from Wirth et al[97] shows the calculated electron density as well as the conduction band profile in a cylindrical NW of radius, $r = 50\,\text{nm}$ and $r = 0$ marks the center of the NW. A peak in the electron density is seen close to the surface. (b) Schematic illustration of charge carriers as well as the influence of a positively charged particle at the surface (shaded red region) in the cross section of n doped Si, intrinsic InAs and p-doped InAs. The colours red and blue correspond to holes and electrons respectively.

3.2. Nanowire growth

The primary component of the sensor, the NWs are grown in an ultra high vacuum chamber (p $\sim 10^{-11}$ mbar) via MBE. In this method a thin film of gold evaporated on to the surface of a substrate, typically InAs[99] and subsequently annealed leading to gold droplets. The mean size of these droplets depends on the thickness of the evaporated film. The NW growth catalyzed by the droplets is carried out at temperatures around $450°C$ with a simultaneous flux of In and As_2. A part of the impinging flux of atoms dissolves in the droplets, supersaturates and crystallizes out at the bottom, the resulting in layer by layer axial NW growth. The NW can also grow radially due to the flux of atoms directly upon the nanowire surface and due to adatoms impinging on the substrate and diffusing up the nanowire length.

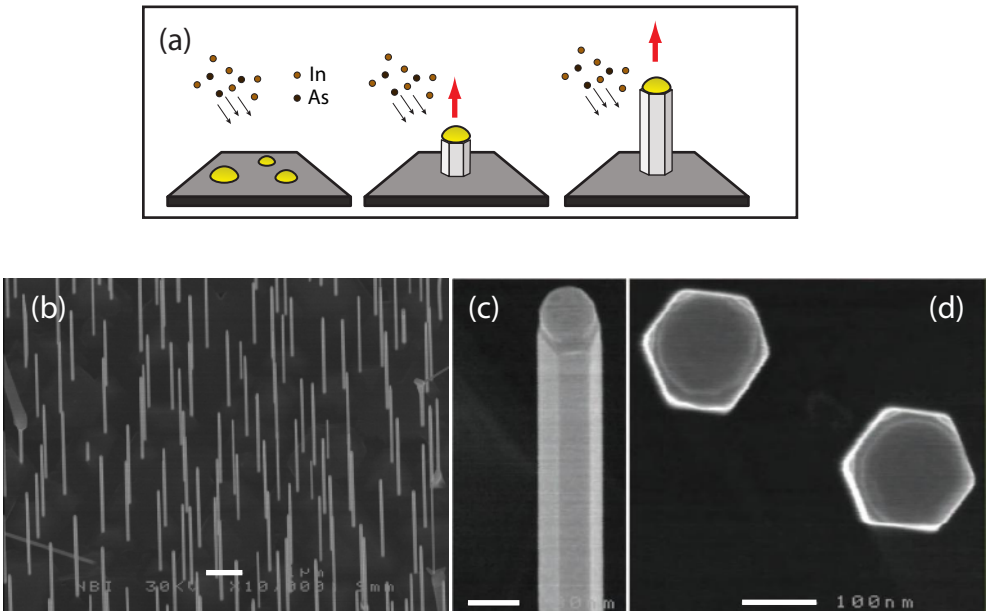

Figure 3.2.: NW growth and characterization. (a) Schematic steps in the NW growth by MBE. (b) A scanning electron microscope (SEM) image of a forest of NWs grown in an MBE chamber. (c) A close up SEM image of a single NW. (d) Top view of adjacent NWs in an SEM. The scale bar in (b), (c) and (d) are 1 μm, 100 nm and 100 nm respectively. The growth schematic taken from Madsen et al[98] and SEM figures courtesy of Martin Aagesen.

The dominating mechanism can be controlled with the substrate temperature and flux ratio of the constituents of the nanowire. The nanowire can be doped by introducing a third flux component such as Be and Si during growth. The NWs thus grown have a typical length of a few microns and a diameter of $\sim$ 100 nm. For our sensor experiments we use intrinsic NWs while we perform low temperature transport experiments on p-doped NWs in chapter 6. The NWs used in this thesis were grown either by P. Krogstrup[100] or M. H. Madsen[98].

3.3. Nanowire field effect transistor (FET)

A field effect transistor (FET) is a semiconductor based device that is effectively a voltage controlled resistor[101]. It comprises a source-drain ohmic electrical contact to lead the charge carriers into and off the device, and a gate contact, typically a metal-oxide-semiconductor type contact capacitively coupled to the semiconductor. A

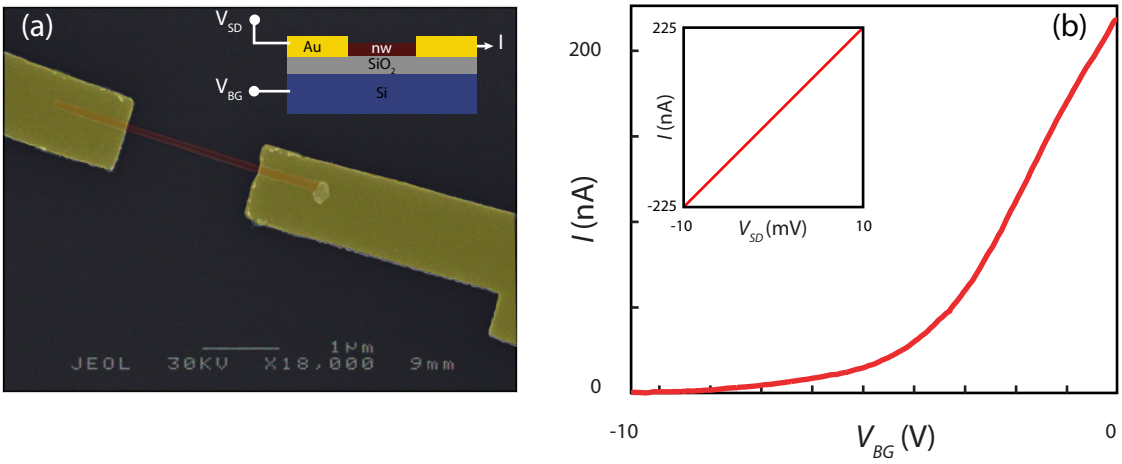

Figure 3.3.: NW FET. (a) SEM image of a nanowire with electrical contacts after EBL. The inset depicts the device schematic with the bias and gate connection. (b) I through the NW device as function of voltage applied to the backgate V_{BG} with bias $V_{SD} = 10\,\text{mV}$. The inset shows I through the same device as a function of bias V_{SD}.

voltage applied to the gate induces an electric field. The gate is usually isolated from the semiconductor by an insulator preventing the transfer of electrons between the two. A field applied to a metal does not penetrate into the bulk as electrons rearrange at the surface screening out the field. However, in the case of a semiconductor with a lower charge carrier density, an applied electric field extends into the bulk changing the potential energy landscape. Thus, controlling the gate voltage the charge carrier density in the semiconductor can be tuned. Fig. 3.3 a shows an SEM image of a NW (brown) with a source-drain electrical contacts (gold) lying on top of a doped Si-SiO_2 substrate which serves as the gate, referred to as the backgate. The inset depicts the device cross-section with bias and gate connections. Applying a small finite bias (10 mV), one can source current through the NW (Fig. 3.3 b inset). Applying a voltage to the backgate, tunes the electron density within the NW seen as a decrease in the current (electron density) with decreasing backgate voltage. Here, the NW is assumed to be a n-type semiconductor. We shall now discuss how to fabricate such nanometer scale FET devices.

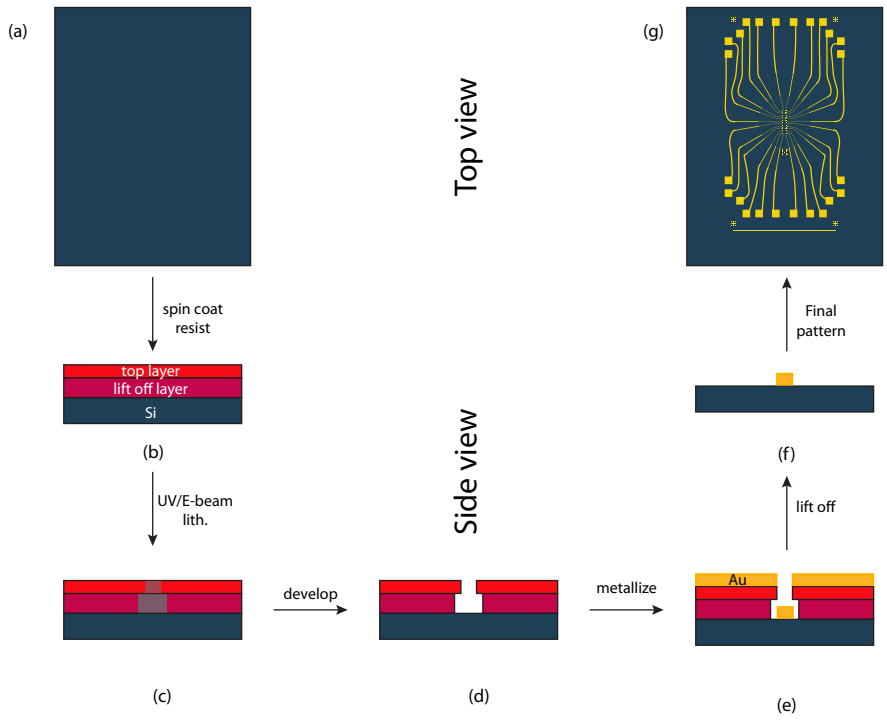

Figure 3.4.: A schematic illustration of the basic steps of lithography in a bi-layer resist scheme. (a) Blank Si wafer scribed to an appropriate dimension. (b) The resist layers are spin coated and baked. (c) The chip covered with resist is patterned via lithography and (d) then developed, washing away the exposed sections. (e) Metallization typically via electron beam physical vapour deposition is followed by (f) lift off in acetone which dissolves the resist, and leaves behind the metal directly in contact with the substrate. (g) The final pattern.

3.3.1. Lithography

A Si substrate is first patterned with a design that allows electrical connection to the NWs as well as an interface to the external measurement setup. Such a pattern is transferred on to the substrate (Fig. 3.4 a) using a combination of negative resist and ultraviolet (or electron beam) lithography. The underlying principle in both techniques is the same. The cleaned substrate is spin coated (Fig. 3.4 b) with a high molecular weight cross linked polymer. A desired pattern can be lithographically defined on a substrate coated with a suitable resist, by shining UV light through a mask or tracing out the pattern with a focused electron beam. The cross links in the exposed sections of the polymer break down (Fig. 3.4 c) and can be washed away in a specific developer (Fig. 3.4 d). Following metallization (Fig. 3.4 e), the chip is

soaked in a solution that dissolves the polymer and 'lifting off' the metal that is not in direct contact with the substrate (Fig. 3.4 f). The pattern now defined on the substrate (Fig. 3.4g) typically has alignment marks (crosses, squares, etc) that are used to align subsequent lithography steps. Following this general description we shall now describe in detail the fabrication methodology.

3.3.1.1. UV lithography

UV lithography is suitable for patterns where the critical dimension is over 1 μm and a large throughput is needed. With a single mask (Fig. 3.5 a), multiple copies of a pattern can be exposed simultaneously. It is thus convenient technique to quickly fabricate large numbers of identical patterns. Fig. 3.5 b-d illustrates the basic steps. We use a Karl Suss MJB-3 mask aligner with a UV light source of wavelength 365 nm and an average intensity of 12 mW/cm^2.

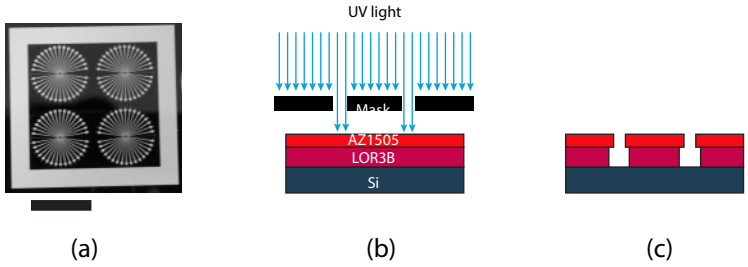

Figure 3.5.: Overview of UV lithography. (a) A portion of a UV mask. The regions in white are transparent glass and the regions in black are chrome. The scale bar is 10 mm. (b) The mask is positioned over the substrate and then exposed to UV light. (c) The regions of resist exposed to UV light are broken down and are washed away during development.

Before spinning resist, the substrate is prepared by cleaning and baking:

- Rinse in Acetone, Methanol and finally in IPA
- 60 s cleaning cycle in the oxygen plasma oven
- Heat at 185°C on a hot plate for 5 min

The last heating step bakes out all solvent, water, etc from the surface and improves adhesion to the subsequent polymer resist layers. Typically, a bi-layer resist scheme - a low molecular weight followed by higher molecular weight polymer is used. This

leads to an 'undercut' resist profile shown in Fig. 3.5 d which allows for easier lift off post metallization:

- Spin coat LOR3B at 4000 rpm for 60 s
- Bake at 115°C for 45 s
- Spin coat AZ1505 at 4000 rpm for 60 s
- Bake at 185°C for 45 s

The chip is loaded in the mask aligner, and exposed to UV light through the relevant mask for 7.5 s. It is developed in a 1:4 mixture of AZ400K developer and millipore water in an ultrasound bath for 45 s. After an optical inspection, the chip is cleaned in the oxygen plasma oven for 20 s to remove resist residues from the developed regions and is now ready for metallization. Typically, 10 nm of Ti and 100 nm of Au are evaporated in a electron gun metallization chamber.

3.3.1.2. E-beam lithography

While UV lithography is suitable for large scale production of lithographically define patterns, E-beam lithography (EBL) is more suited for proto-typing. In this study, EBL is needed in order to fabricate electrical contacts to NWs deposited on a substrate. Since the NWs are dispersed randomly everytime (Sec. 3.3.2), this method allows precise lithography that can be customized every time. EBL differs from UV lithography in that the pattern is traced out by a focused electron beam on the substrate spin coated with resist. The cross linked polymers in the exposed regions are broken down and washed away during development. EBL is a precision technique capable of making patterns with features size as small as 10nm. The trade-off however is that it is a slow process where a single pattern can take up to several hours to expose compared to a few seconds in UV lithography. We use a Raith Eline-100 EBL system, typically at an acceleration voltage of 20 kV with an aperture of 30 μm. The resist PMMA has a clearing dose of 200 μC/cm^2 at this acceleration voltage.

The process steps are similar as before. After cleaning the chip, it is spin coated with two layers of resist:

- Spin coat 6% (9%) Co-polymer in Ethyl lactate at 4000 rpm for 60 s
- Bake at 185°C for 3 min

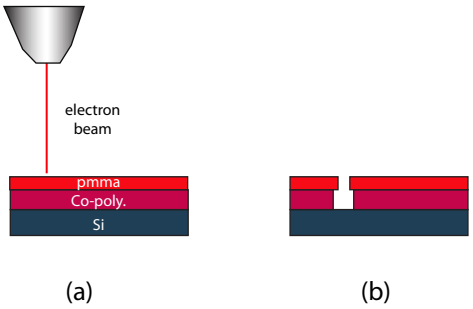

Figure 3.6.: Overview of e-beam lithography. (a) The regions exposed to the focused electron beam break down (b) and are washed away during development

- Spin coat 2% (4%) PMMA in Ethyl lactate at 4000 rpm for 60 s
- Bake at 185°C for 3 min

After exposure the chip is developed in a 1:3 mixture of MIBK and in an ultrasound bath for 60 s, and then rinsed in IPA. After a 20 s cleaning cycle in the oxygen plasma oven, the chip is now ready for metallization.

3.3.2. Nanowires deposition, optical inspection and design

A small piece of the substrate with the array of nanowires grown in the MBE, is cleaved and added to a vial with a few drops of IPA. A suspension of the nanowires is obtained by sonication in a ultrasound bath for 10 s. Using a pipette, a small drop ($\sim 5\,\mu$L) is deposited on top of a chip with a predefined pattern (Fig. 3.7 a). This pattern, discussed in the next section, is lithographically defined in gold on a Si substrate. A dark field optical image of a portion of the central region of interest on the chip post NW deposition is shown in Fig. 3.7 c. The red circle in the image marks a NW. The four crosses in the optical image are used to align and overlay it over the design (Fig. 3.7 c) in a suitable CAD program. A suitable NW is selected and leads (red, brown) are drawn connecting it to the arms in the design (blue) as shown in Fig. 3.7 d.

3.3.3. Electrical contact

There is an additional process step during the lithographic definition of electrical contacts to NW via EBL. After exposure and development of the polymer resist,

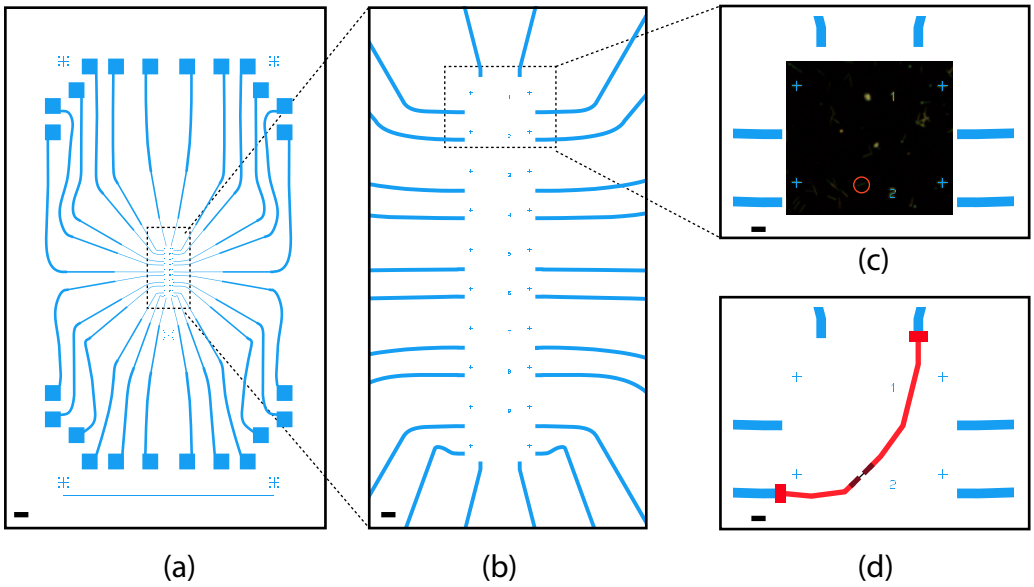

Figure 3.7.: Contacting a NW by EBL: optical images to the CAD file. (a) Schematic overview from a CAD file of the predefined pattern on the chip before NW deposition. (b) Magnified view of a part of the central region of interest in the pattern. (c) A dark field optical image of the dotted region in (b) after NW deposition, overlaid with the design. A NW is marked by the red circle. (d) Connections (red, brown) are drawn from leads in the pre-existing pattern (blue) to the marked nanowire. The scale bar in the images are 150, 20, 5 and 5 μm respectively.

the native oxide on the nanowire needs to be etched away before metallization, in order to make ohmic contact with the semiconducting nanowire itself. Some of the etching techniques used are discussed here. A more thorough overview of the techniques used by different experimental group is covered by Nissen et al[102]. Post etching, the chip is loaded in a high vacuum chamber (p $\sim 10^{-8}$ mbar) and metal is evaporated on to the chip. Typically, 5-10 nm of a sticking layer such as Ti or Ni is used followed by 100nm of Au.

A 7% solution hydrofluoric acid (BHF) buffered in ammonium fluoride is a commonly used etchant. The chip is dipped in the etchant solution for 3-5 s, washed in (DI) water and immediately loaded into the metallization chamber. The BHF etch only affects the oxide on top of the NW as well as that on the Si substrate. A known drawback of this method is that the etched surface quickly re-oxidizes when exposed to air. This method usually yields ohmic contacts to the NWs but the overall device

resistance is often large.

An alternative is to use a simultaneous etching and passivation technique[103]. A 3M solution of S in a 21% aqueous solution of $(NH_4)_2 S$ is prepared. This stock solution is further diluted with de-ionised water to make a 2% solution to prepare the final etching solution. The chip is placed in this solution and kept in a water bath at 50°C for 15 min. It is then rinsed in DI water and ready for metallization. The advantage of this etching solution is that it etches the oxide and passivates it with sulphur, preventing re-oxidation when exposed to air. This method yields low resistance devices with ohmic electrical behaviour, however the etching solution tends to delaminate the polymer resist layer if the adhesion to the surface is not appreciable enough.

The last etching technique used involves in-situ physical sputtering of the surface with Ar ions within the chamber prior to metallization. In this process, a plasma of Ar ions is accelerated towards and bombarded on the chip, physically milling away the oxide at the surface. Since this is followed by evaporation of the metal without breaking vacuum, it yields devices of low overall resistances as before while avoiding issues of delaminating resist layers. It also increases device yield by eliminating an entire step in the process flow. An AJA-international metallization chamber with an in-built Ar ion sputtering system was used for etching and metallization.

3.4. Nanowire sensor

To make a sensor, the NW FET device needs to be electrically isolated so that it is only capacitively coupled to the interactions at its surface. Chemical/biological interactions at the surface lead to changes in the surface charge distribution which influences the conductivity of the device via the 'field effect'. We shall now discuss processing steps necessary to ready a substrate with electrically contacted NWs as a chemical/biological sensor platform.

3.4.1. Electrical isolation

As a sensor, the NW should be sensitive to chemical/biological interactions at the surface through a change in surface charge distributions. To ensure purely a capacitive coupling to the NW surface and prevent current leakage from the NW

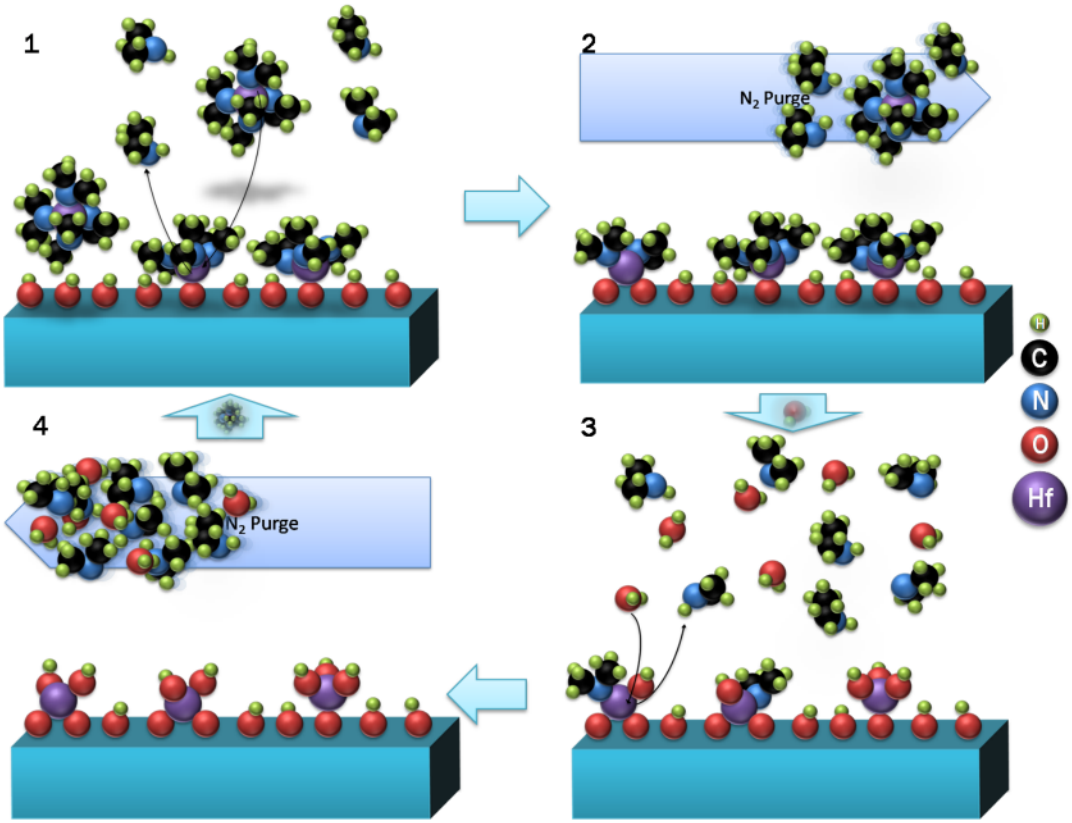

Figure 3.8.: A cycle during atomic layer deposition of hafnium oxide: (1) Organo-metallic precursor pulse reacts with hydroxyl groups at the surface. (2) A N_2 purge removes all unreacted precursor. (3) Water vapour pulse reacts with the organo-metallic groups at the surface, and the amido groups are carried away in the N_2 purge (4), leaving behind a monolayer of hafnium oxide at the surface. Figure adapted from Hviid et al[104]

into the buffer solution, the entire substrate is coated with a thin layer of a conformal high quality oxide by a process known as atomic layer deposition (ALD). Depicted in Fig. 3.8, ALD involves sequential pulsing of an organo-metallic precursor followed by a water vapour pulse, with a N_2 purge in between. Each cycle corresponds to the deposition of an oxide monolayer, with rates varying between 0.8-1.2 Å/cycle. The sequence for the deposition cycles done at 90 °C are presented in Sec. 3.4.1. A Cambridge Nanotech Savannah ALD-100 system used for this process. Tetrakis (dimethylamido)-hafnium (IV) was used as a precursor for hafnium oxide and trimethylaluminium (TMA) as a precursor for aluminium oxide. We have used both HfO_2 and Al_2O_3 as electrical isolation in our experiments. The advantage oxide deposited via ALD is that it grows layer by layer in an conformal manner, thus leading to a high quality oxide with few defects. It is possible to deposit as little as 20 nm providing minimal leakage current and also a large capacitive coupling between the semiconductor and the surface interactions making it a popular choice[84,105,106].

Action	Pre-cursor	t (s)
Pulse	1	0.2
Wait	-	60
Pulse	0	0.015
Wait	-	60

Table 3.1.: ALD cycle parameters done at 90 °C where 1 is the organo-metallic precursor and 0 is water vapour.

3.4.2. Silanization

In this section we discuss self assembled monolayers (SAMs) as a convenient way to change the active surface group on the oxide.. This is commonly employed as a linker layer between the oxide surface and recognition motifs such as biotin[8] as well as a passivating layer over SiO_2 to minimize leakage currents[34]. Typically molecules used for forming SAMs consist of three sections - a head, a linker and a terminal group. The head group has a high affinity of the surface groups on the substrate. The terminal group is chosen based on specific interactions with other molecules in subsequent functionalization steps. Fig. 3.9 shows a schematic overview of a surface functionalized with an amine terminated silane SAM. Beside the formation of the covalent -O-Si- bond(Fig. 3.9 a), the silane molecule can also

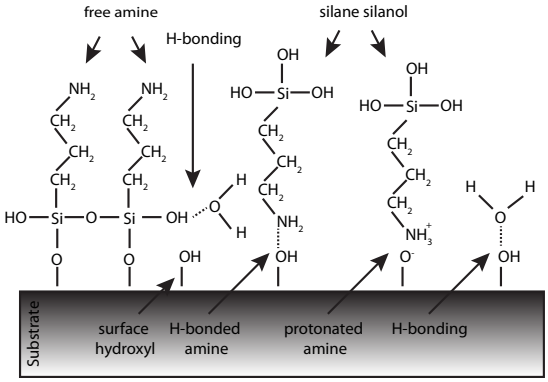

Figure 3.9.: Schematic of an oxide surface functionalized with a self assembled silane monolayer depicting various configurations of linkage of the silane group to the surface. The figure is adapted from [107]

attach to the hydroxyl groups at the surface via hydrogen bonding (Fig. 3.9 b) or a protonated amine $\left(-NH_2^+\right)$ to the deprotonated hydroxyl group $(-O^-)$, resulting in hydroxyl $(-OH)$ surface terminal groups. Incomplete coverage of the surface can also leave exposed hydroxyl terminal groups. The homogeneity of the silane SAM depends on the reaction conditions such as reaction time, curing time and also whether it is carried out in liquid or vapour phase.

The following protocol was developed and discussed in detail by Frederiksen et al [108]. A brief overview is presented here. Hydroxyl groups at the ALD oxide surface were activated by a cleaning process where the wafers were immersed in 1:1 hydrochloric acid and methanol for 30 min, and then rinsed successively in ethanol, methanol, isopropanol. This was followed by a 2 min cleaning cycle in a oxygen plasma oven. The wafer with activated hydroxyl surface groups were transferred to a vacuum atmosphere with 100 µL (3-Aminopropyl)triethoxysilane silane (APTES) and 20 µL N, N-diisopropyl-ethylamine and incubated for 1 h in a N_2 environment. Finally, the chip is cured on a hot plate at 115°C for 7 min and placed in a vacuum chamber overnight.

3.5. Fluidic setup

The following section describes the final optimal setup identified through a long series of iterative experiments. The sensor chip with the electrical isolation and

optional functionalization is prepared to be fitted with the fluidic setup, shown in Fig. 3.10. The chip is glued, using a silver paste, on to a 28 pin DIP socket (CSB02813 spectrum-semi). Electrical connections between the chip and the socket are made using a wire bonder. An FPM O-ring (M-seals, inner diameter ~ 1 mm, outer thickness ~1 mm) is placed over the central sensing region and epoxy (Epotek 353ND) is poured outside around the O-ring. The epoxy is cured at 100 °C on a hot plate for 30 mins. This protects the bonding wires and the gold leads on the chip outside the O-ring in the case the water tight seal breaks. Fig. 3.10 d shows the sensor chip mounted in the DIP socket, with the O-ring at the center and cured epoxy protection around. A sterile PCR tube (outer diameter ~ 5 mm) serves as a fluidic chamber. The tube is sliced at one end to create an opening for the liquid gate, inlet and outlet. A hole, 0.5 mm in diameter, was punched through the the lid of the PCR tube. This end rests on the O-ring to create a water tight connection with the chip. The PCR tube is mounted on a THOR labs lens mount with XY translation control of about 0.5 mm Fig. 3.10 e. This allows for the PCR tube with the O-ring to be aligned with the central sensing region of the chip. An Ag-AgCl electrode (MI-402 micro electrode) immersed in a saturated KCl solution which in turn is encased in a flexible tube is used to set the potential of the solution over the sensor. A ceramic frit at the end of the tube acts as a junction between the inner KCl solution and the outer solution. The frit blocks proteins and other larger molecules from coming in direct contact with the electrode and ensures a stable potential. In the early experiments, such as those described in Sec. 4.1 and Sec. 4.2.1-Sec. 4.2.2, the solution in the fluidic chamber is manually exchanged using pipettes. Subsequently, we switch to a semi-automated method where a peristaltic pump (Longer Pumps BT100-1L) is used to evacuate the solution reproducibly from the same position (Fig. 3.10 b) while fresh solution is manually pipetted in.

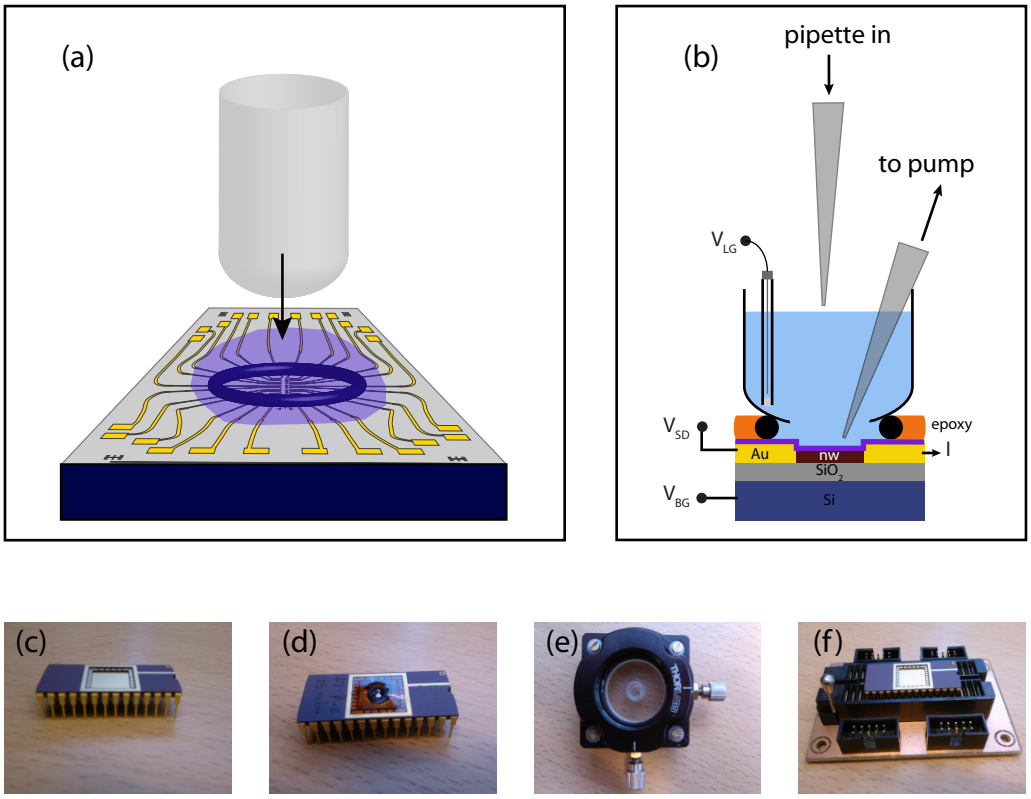

Figure 3.10.: Fluidic setup. (a) Schematic depiction of the sensor chip with the electrical leads (gold), ALD isolation (blue), O-ring (black) and the fluidic chamber. (b) Cross sectional view of the sensor setup. (c) The 28 pin DIP chip carrier. (d) Chip carrier with the sensor chip glued in, bonded and epoxy isolation outside the O-ring. (e) Top view of the THOR labs XY translation mount for the PCR tube. (f) A zero insertion force (ZIF) socket for the chip carrier to allow for electrical connection between the external measurement setup and the chip.

4. pH sensing

A simple yet effective way to characterize the NW sensors is via pH sensing[8,36]. In this chapter, we demonstrate the sensor response to solutions of different pH values. Starting with a basic device setup, the InAs NW sensor response to pH is presented. We also investigate pH response of a sensor with chemical surface modification. The role of the electrolyte solution in the stability of sensor response is examined. Multiple parallel sensor measurements can be used to gauge uniformity of response as well as device to device variation. We present simultaneous and sequential measurement schemes for the same. Finally, combining various elements such as buffered solutions, a liquid gate and a pump for solution exchange, we demonstrate a stable platform for pH sensing. The reader will notice a clear progression from rudimentary proof of principle experiments to highly reproducible devices. All aqueous solutions as well as vapour phase silanization treatment were arranged by R. Frederiksen and N. Lloret in the group of K. Martinez.

4.1. Non-buffered solutions

As a starting point, solutions of differing pH values are prepared using ultra pure water (MQ water, Millipore) with drops of HCl/NaOH added to adjust the pH. This value was checked with a commercial pH meter (Meterlabs PHM201). In the following, the response of a sensor with an unmodified bare oxide surface is presented and then contrasted with a sensor with a silanized oxide surface.

4.1.1. Bare oxide

In this section we report on an experiment with an unfunctionalized sensor with ALD HfO_2 isolation. The mixing chamber was a pipette tip cut down to appropriate dimensions and glued to the substrate using silicone glue. The solution in the mixing

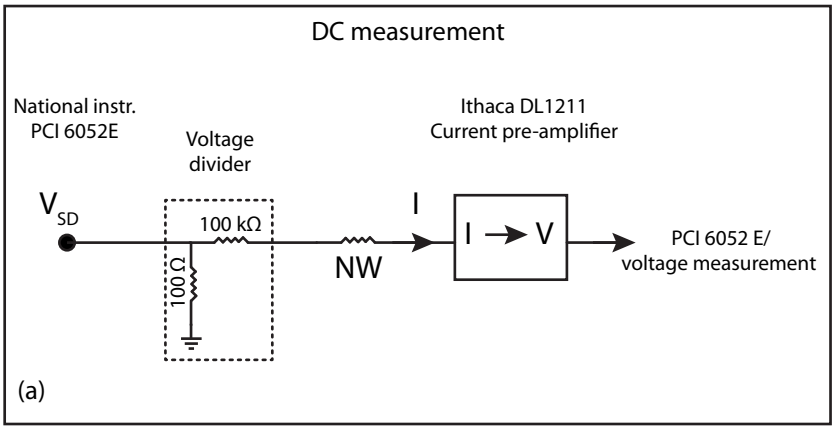

Figure 4.1.: A schematic of the measurement setup for a DC measurement. A computer controlled data acquisition card (DAC) provides the source-drain bias (V_{SD}). A 1:1000 voltage divider is used to reduce noise on the bias. The output of the current amplifier is measured on an analog input on the same DAC.

chamber was exchanged manually using a pipette. DC measurements (See Fig. 4.1) were performed on the following device with a source-drain voltage bias V_{SD} of 10 mV (National Instruments PCI 6052E) and the current was measured using a current preamplifier (Ithaca DL1211). The solution potential is left floating as we do not use a liquid gate.

The device parameters for the NW sensor:

- NW diameter: ~100 nm
- Device length: ~2 μm
- Back gate oxide: SiO_2, 500 nm
- Etchant used: BHF
- Device isolation: ALD HfO_2 @ 90 °C, 20 nm

Fig. 4.2 a shows a time trace of the measured current I through a single NW sensor as solutions of decreasing pH values are introduced and flushed in the mixing chamber. Vertical dashed grid lines mark solution introduction of a new pH value while black arrows mark all solution exchanges. The addition of a new solution is marked by a spike followed by a transient settling current of unto 400 s. The origin of the spikes and transient response is discussed in Sec. 2.4.3 (See also Fig. 2.8). Briefly, solution exchange disturbs the equilibrium at the surface of the sensor and the settling time depends on the diffusion of H^+ ions. Fig. 4.2 b shows the that the sensor response

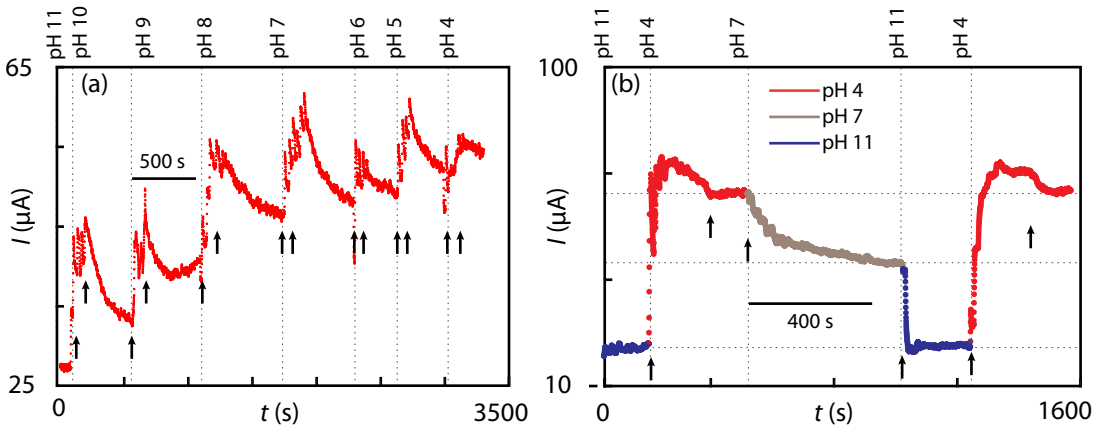

Figure 4.2.: pH response of a HfO_2 covered NW sensor. (a) I at $V_{SD} = 10\,\text{mV}$ as a function of time as solutions of decreasing pH are flushed into the mixing chamber. Arrows mark solution addition and subsequent flushes. (b) In a different time trace, the sensor current is found to be reproducible on cycling through pH 11 to 4, but is marked but a transient response of up to 400 s.

to be reproducible as it is cycled through pH 11 to 4 twice. With each pH step the current settles into a new value presenting spiked step-like response, with the expected trend of increasing current with decreasing pH.

As discussed in Sec. 2.2, the surface charge distribution at the oxide-solution interface depends on the reaction equilibrium of the hydroxyl terminal groups. At a low pH (for e.g., pH 4), there is a net accumulation of positive charges at the surface due to a larger number of protonated hydroxyl groups $\left(-OH_2^+\right)$. Similarly, at large pH (for e.g., pH 10) there is a net negative charge at the surface due to a larger number of deprotonated hydroxyl groups $(-O^-)$. For a n-type semiconductor such as InAs, a net positive surface charge would attract and increase electron concentration within the NW and result in increased current/conductance. Negative charges at the surface would have the opposite effect.

To further quantify the sensor response to pH changes, it is necessary to account for changes in the capacitive coupling of the NW to the surface at different pH. Typically, this is done using a gate trace (NW current as function of gate voltage) to find the corresponding gate potential for a given current baseline[1]. However due to a bad electrical contact between the Si substrate (degenerately doped substrate) and the chip carrier we could not use the backgate to tune the NW conductivity.

[1]This procedure, depicted in Fig. 4.4, is discussed in the following section.

We conclude that though the sensor response is dominated by transients, it is reproducible and decreasing pH leads to increasing current. In the next section we repeat the same measurement protocol with a new NW sensor with chemical surface modification.

4.1.2. Silanized surface

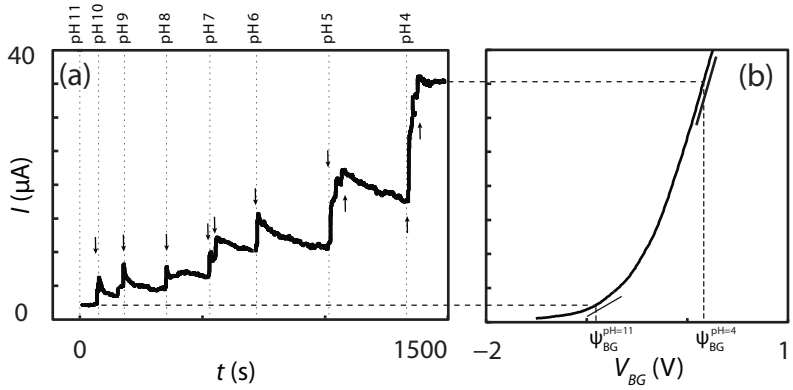

Figure 4.3.: pH response of sensor with a silanized surface. (a) I at $V_{SD} = 10\,\mathrm{mV}$ as a function of time as solution of varying pH values are flushed into the mixing chamber. (b) I through the NW as a function of V_{BG} with $V_{SD} = 10\,\mathrm{mV}$. Dashed lines mark the conversion current corresponding to pH 11 and pH 4 to the equivalent back gate potential ψ_{BG}. The sloped lines at the intersection of dashed lines with the gate trace indicate the slope dI/dV_{BG} at that point.

For this experiment, the oxide surface of a new sensor chip is functionalized with a self assembled silane monolayer (Sec. 3.4.2) resulting in amine (-NH_2) terminal groups. Surface modification can be used to reliably change the terminal surface groups and lay the foundation for further functionalization schemes such as biotin (linkers to streptavidin, avidin, etc). DC measurements are performed on a single NW sensor using solutions of varying pH values as discussed in the previous section. As before, we do not use a liquid gate and the solution is left at a floating potential. The conductivity of the NW can however, be tuned via voltage applied to the underlying backgate V_{BG}. During the operation of the device, V_{BG} is kept at 0 V. Solution in the mixing chamber is exchanged manually using pipettes.

NW device parameters:

- NW diameter: ~100 nm

- Device length: ~1 μm
- Back gate oxide: SiO_2, 500 nm
- Etchant used: BHF
- Device isolation: Silanized ALD HfO_2 @ 90 °C, 20 nm

Fig. 4.3 a shows I through the NW at $V_{SD} = 10\,\text{mV}$ with solutions of decreasing pH flushed into the mixing chamber. Vertical grid lines mark solutions of new pH while the arrows mark solution exchanges. Fig. 4.3 b shows I through the NW as a function of V_{BG}. The sensor response appears to be of similar magnitude as well as present the same transient trend as in Sec. 4.1.1. It can be seen that the capacitance of the NW reflected in the transconductance dI/dV_{BG} (dashed lines), changes from pH 11 to pH 4. We shall discuss how to account for this when comparing the pH step responses below.

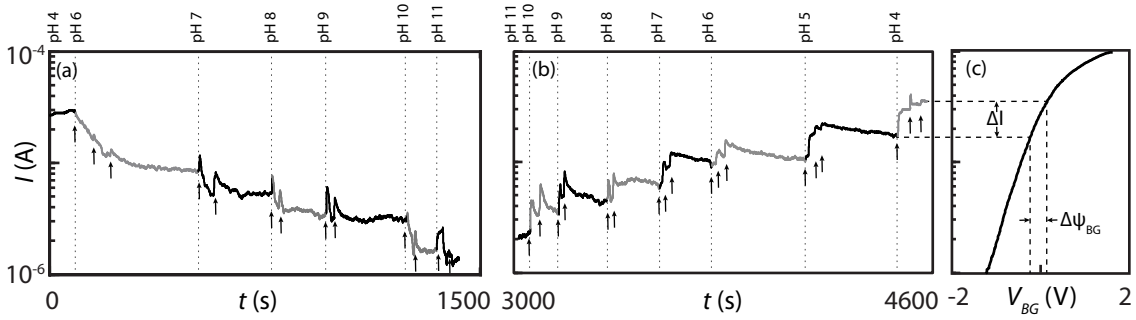

Figure 4.4.: Additional time trace of I through the same NW sensor plotted on a logarithmic scale. (a) Sensor response as pH is changed from 4 to 11 and then (b) from pH 11 to 4. (c) I through the NW device in MQ water as a function of V_{BG}. Dashed lines depict the conversion of the change in current ΔI due to a pH step to the equivalent change in gate potential $\Delta\psi_{BG}$.

Fig. 4.4 a-b shows additional time traces of I through the same NW sensor, as solutions of sequentially increasing (and then decreasing) pH values are flushed (black arrows). These traces are useful for comparing reproducibility as well as drift in sensor response with time. Fig. 4.4 c shows the NW gate trace on a logarithmic scale. Fig. 4.4 b-c show dashed lines which mark the change in current ΔI corresponding to the step from pH 5 to pH 4 on the gate trace, which in turn is used to extract the change in the back gate potential $\Delta\psi_{BG}$ for the pH step[2]. $\Delta\psi_{BG}$ is a measure of the

[2]Since the device remains in the sub-threshold regime from pH 4 to 11 with a linear log (I) – V_{BG}

change in surface potential ($\Delta\psi_0$), being related to it by a factor, Eqn. 2.16. The solution in the mixing chamber is not changed from 1500 to 3000 s and the signal baseline effectively drifts by 62 mV (converting the drift ΔI to $\Delta\psi_{BG}$). This drift can be attributed to the unstable pH of the solution and is not observed with the use of buffered pH solutions presented later.

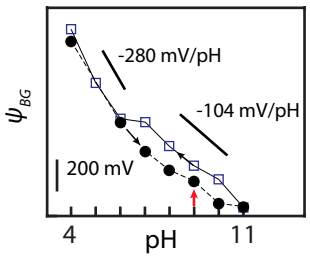

Figure 4.5.: Back gate potential corresponding to the stable baseline after a solution flush as function of the pH of the solution. The potential for solution flushes from pH 4 to 11 (filled circles) and pH 11 to 4 (squares) are shown together after subtracting the drift in the sensor signal (~62 mV) when left exposed to a solution of pH 11 from t = 1500 to 3000 s. The red arrow marks a bump in titration trace possibly due aliphatic amine groups from the silanization step (pKa ~ 10).

The back gate potential corresponding to the stable baseline (ψ_{BG}) for a given pH are shown in Fig. 4.5. The steps in potential for pH 11 to 4 (black squares) are plotted after subtracting the offset due to drift. As seen in Fig. 4.4 b for pH 10 to pH 7, due to an insufficient waiting time after solution exchange, the transient sensor response does not full settle. This can be seen as a disparity between the potentials for the two different pH step directions (filled circles, empty squares) in the specified pH range. An increase $\frac{d\psi_{BG}}{dpH}$ around pH 4-6 is observed and may correspond to the pK_a of hydroxyl groups pointing towards an insufficiently homogenous silane monolayer (Sec. 3.4.2). Experiments to probe the pH sensitivity of a surface after silane passivation have found a longer vapour phase reaction time increases the homogeneity of coverage[68]. A small bump in $\Delta\psi_{BG}$ around pH 9 might be due to amine groups, with the pK_a of aliphatic amino groups ~10[109]. In the ideal case of a homogenous silane layer with large number of $-NH_2$ terminal groups a linear $\Delta\psi_{BG} - pH$ response is expected (Nernstian). Lower $-NH_2$ group density would result in a non linear trace, as is observed, but with increased $\frac{d\psi_{BG}}{dpH}$ around the pK_a of the amino groups.

relation, one can visually compare step sizes on a semi-log plot.

We conclude that a pH dependent sensor response is observed which is however marked by transients. The pH response of the sensor (ψ_{BG} vs. pH, Fig. 4.5) was used to probe the nature of the sensor surface. The silanization of the surface was suspected of being inhomogeneous. In the next section we present experiments using pH buffered solutions and examine their effect on signal stability.

4.2. Buffered solutions

We believed the transients seen till now in the sensor response arose due to spatial variations of pH in the solution with the 'settling time' related to the diffusion of H^+ ions . With the motivation of reducing these transients, we switched to buffer solutions with a well defined pH value. A buffer solution is a mixture of a few components, typically a weak acid and its conjugate base or vice-versa, which can dissociate to release H^+ ions or combine with excess of the same in order to maintain pH constant. Naturally, a larger concentration of the buffer species would imply a larger capacity to resist to changes in pH. In addition we present simultaneous measurements on multiple NWs as well as an improved iteration of the fluidic setup.

4.2.1. Multiple sensors - Parallel measurement

Simultaneous measurements on multiple NWs allow for the demonstration of reproducibility of the sensor response across different devices on the same chip. Concurrent trends can be used to rule out false positives and random shifts in baselines. Moreover, for other types of sensing measurements such as multiplexed detection such a technique can be important.

The following measurements were simultaneously carried out on three NW sensors (red, blue and green traces, Fig. 4.7) on one chip. AC measurements (Fig. 4.6) on two NWs (red, green) were carried out using lock-in amplifiers at an AC bias of 1 mV with reference frequencies around 200 Hz. DC measurements on the third NW (blue) were performed as before. The rise time for both measurements was set to 1 s. Lock-in amplifiers are typically used to measure conductance while DC measurement using current pre-amplifiers are used to measure current. As before, the solution potential is left floating without a liquid gate while the underlying backgate can

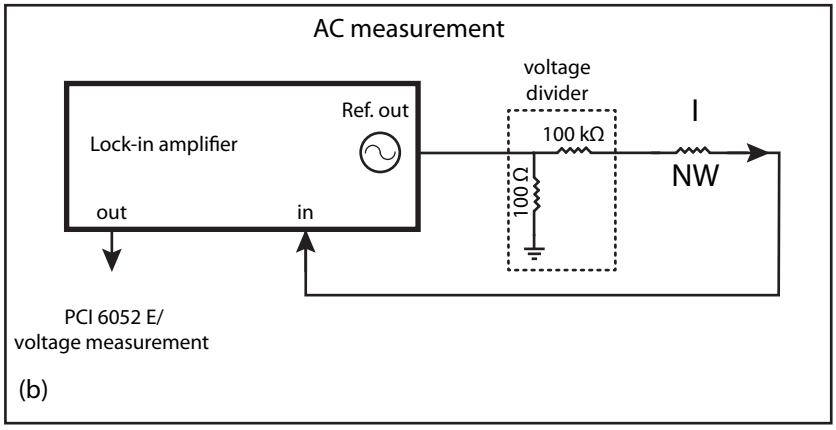

Figure 4.6.: Schematic setup for an AC measurement. Typically the reference frequency from a sine wave generator in the lock-in after a voltage divider passes through the device under test. The lock-in amplifier measures the amplitude of the resulting current which is proportional to device conductance. The output of the lock-in is measured on an analog input on a DAC connected to a PC.

be used to tune NW conductivities. Solution in the mixing chamber is exchanged manually using a pipette.

Device parameters:

- NW diameter: ~100 nm
- Device length: ~1 μm
- Back gate oxide: SiO_2, 300 nm
- Etchant used: BHF
- Device isolation: ALD HfO_2 @ 90 °C, 20 nm
- Buffer: 30 mM TRIS

Fig. 4.7 a shows step responses of three NW sensors as the pH is changed from 4 to 11 and then back to 4. All sensors present the same trend concurrently. It is interesting to note that the response to a pH step for all sensors is sharp and settles within the rise time of measurement setup. The sharp step response and the lack of transients can be explained thus (See Sec. 2.4.3). On changing the pH of the bulk solution, the terminal groups at the sensor surface need to dissociate (or change state) in order to re-establish equilibrium. Usually, equilibration is limited by the diffusion of H^+ ions to (or from) the sensor surface. However since the buffer species

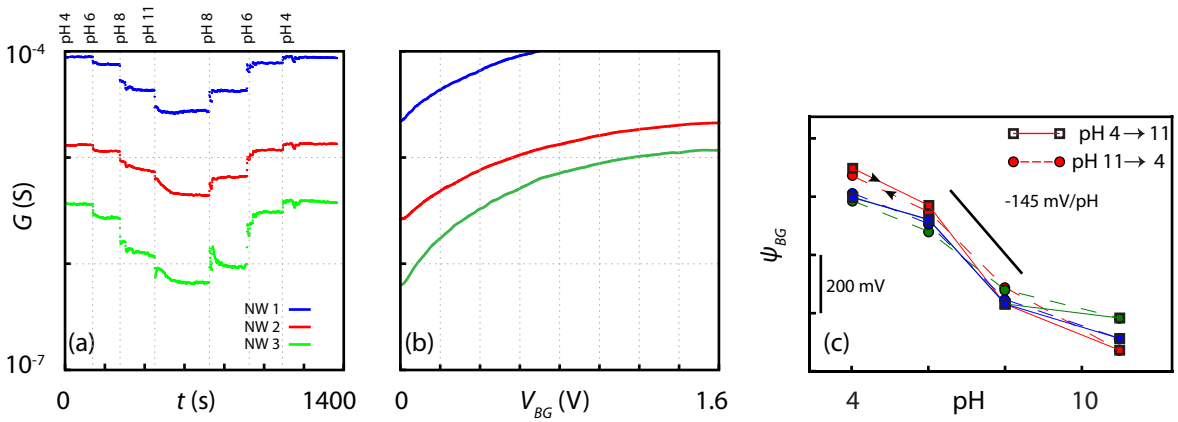

Figure 4.7.: pH response of three NW sensors measured simultaneously. (a) Change in device conductance as the buffers for varying pH. (b) Change in the NW conductance with backgate voltage. (c) NW conductance G is converted to an equivalent backgate potential and plotted with the offset at pH 8 subtracted.

in solution close the sensor surface can supply (or react with excess) H^+ ions, the terminal group and the resulting surface charge density reaches the new equilibrium quickly.

Fig. 4.7 b shows the conductance of the NWs can be tuned with voltage applied to the backgate, V_{BG}. Using these traces the stable conductance baselines for a given pH are converted to potentials, and shown in Fig. 4.7 c. For each NW the potential for both pH directions (circles, squares) is seen to be reproducible. All three sensors respond in kind exhibiting the same sigmoidal trend, visibly different from the $\psi_{BG} - pH$ curve in Fig. 4.5. The variation in conductance between the three NWs seen in Fig. 4.7 a can be attributed to the quality of the electrical contact[3].

The sigmoidal shape of the these traces with increased sensitivity between pH 6-8 implies the point of zero charge (pH_{pzc}) of the surface lies in this range. Close to this pH_{pzc}, the surface has the largest number of neutral hydroxyl groups and is most reactive, thus leading to large changes in surface potential (ψ_0) for small changes in pH. pH_{pzc} for RF sputter deposited HfO_2 has been experimentally found to lie between pH 5 and 7.5[90] and our data is consistent with this value.

[3]BHF was used to etch the NW oxide just before metallization. Due to the finite delay between etching and loading the chip into the metallization chamber during which the freshly etched NW surface can reoxidise on exposure to air, order of magnitude variation in device conductance can been observed.

A large number ($\sim 10^{-18}\,\mathrm{m}^{-2}$) of hydroxyl groups at the oxide-solution interface would give a linear $\psi_{BG} - pH$ dependence, and the sigmoidal shape of the curve implies a lower surface group density (N_s). Using the estimate for pH_{pzc} and the $\frac{d\psi_{BG}}{dpH}\,|_{max}$, the surface site density, N_s can be calculated (Eqn. 2.20). However without a good estimate for the capacitance of the back gate (C_{BG}) to the NW, it is difficult to convert ΔV_{BG} to $\Delta\psi_0$. In later experiments an additional gate (liquid gate) is used which simplifies the estimation of $\Delta\psi_0$.

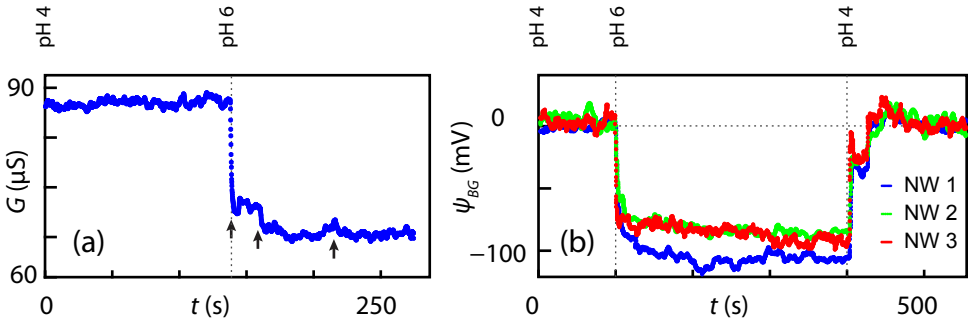

Figure 4.8.: Reproducibility and signal to noise ratio. (a) pH 4 to 6 step response of a single sensor. (b) The response of all three sensors converted to equivalent backgate potential and plotted with the offset at pH 4 subtracted. Arrows mark solution exchange.

Fig. 4.8 a focuses on a single sensor response. A change from pH 4 to 6 causes the sensor to respond and settle into a new baseline within seconds as opposed to nearly 300 s in the case of non buffered solutions. The signal is stable and devoid of transients. Fig. 4.8 b shows the multiple sensor signals for a flush from pH 4 to 6 to 4 again. The raw conductance signal was converted to back gate potential and plotted alongside, with the offset at pH 4 subtracted. The signal response from the three sensors for the given pH step is now observed to be of a similar magnitude.Practically, surface contamination can lead to differing magnitude of responses and thus simultaneous measurements can be used to gauge the state of the sensor surface. With a solution flush from pH 6 to 4, the signal from all three sensors returns to the original pH 4 baseline demonstrating reproducibility across sensors.

Comparing Fig. 4.8 with Fig. 4.4 and Fig. 4.2, we conclude that buffer solutions are essential for signal stability. Clear stable and reproducible steps are seen in response to pH changes. Multiple simultaneous sensor measurements show similar magnitude

of responses and variations in this magnitude can be used to analyse the sensitivity of the oxide surface. However, the variation of the quality of electrical contact from between different NW devices is unpredictable.

4.2.2. Improved fluidics chamber

Here, we present parallel simultaneous DC measurements on two NW sensors (blue and green traces) at V_{SD} of 10 mV with an improved mixing chamber setup, as the one described in Sec. 3.5. The fluid chamber is now a sterile PCR tube clamped to the substrate via an O-ring shown in Fig. 3.10, doing away with the silicone glue. The O-ring material is selected based on its chemical inertness and ion absorption properties as specified by the manufacturer. The solution potential is left floating, while an underlying back gate is be used to tune the conductivity of the NWs. In the course of the sensing experiment V_{BG} is fixed at 0 V. A simultaneous etching and passivation of the NW oxide before metallization yields devices of lower resistance (~10 kΩ) with a smaller variation between devices.

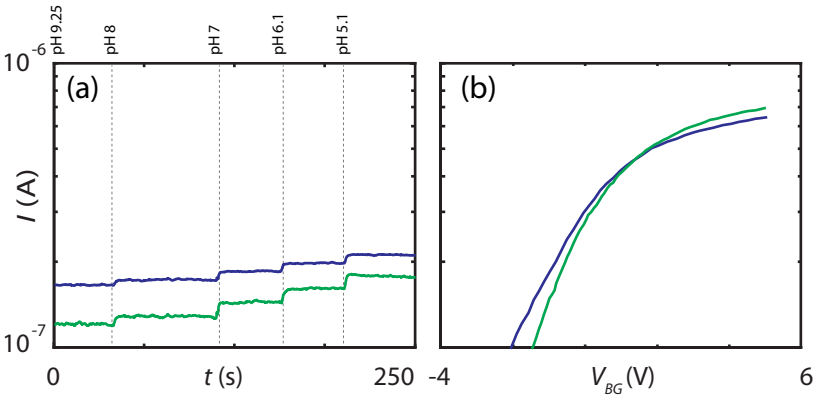

Figure 4.9.: (a) Step response from two NW sensors (green, blue) as pH is changed from 9 to 5. (b) I at $V_{SD} = 10\,\mathrm{mV}$ through the NWs as a function of V_{BG}.

Device parameters:

- NW diameter: ~100 nm
- Device length: ~1 μm
- Back gate oxide: 300 nm
- Etchant used: $(NH_4)_2\,S_x$

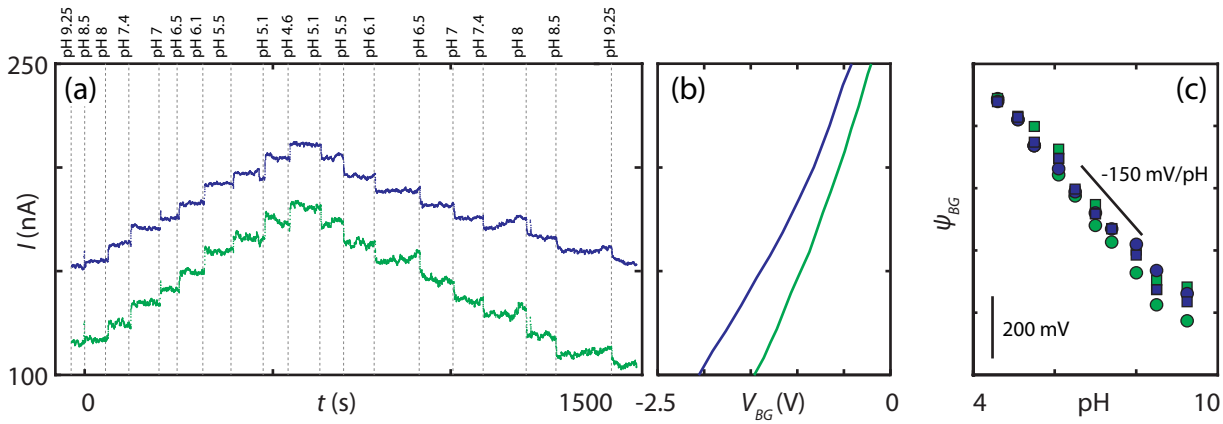

Figure 4.10.: (a) Detailed current response of the two NW sensors measured simultaneously as buffered solutions of varying pH are flushed into the mixing chamber. Vertical grid lines mark the introduction of a solution of different pH and are indicated by the labels. (b) I through the NWs are a function of V_{BG}. (c) This trace is used to extract the potential corresponding to a stable baseline for a given pH.

- Device isolation: ALD HfO_2 @ 90 °C, 20 nm
- Buffer: 100 mM PBS (1X) and 10 mM PBS (10X)

Fig. 4.9 a shows steps in the current response of two NW sensors as solutions of decreasing pH (1X buffer) are flushed from pH 9 to 5. The conductance of the two NW sensor (in MQ water) can be tuned via the back gate (V_{BG}) as shown in Fig. 4.9 b.

Fig. 4.10 a shows a more detailed sensor response as the pH is changed from 9 to 4 and back to 9 in steps of 0.5. This allows for the demonstration of stability and reproducibility. The sensor responses are converted to the corresponding back gate potentials using Fig. 4.10 b and the $\Delta\psi_{BG} - pH$ traces are presented in Fig. 4.10 c. The two NW sensors shows nearly identical trends, with a near linear response over the pH range 4 to 9 implying a high density of surface hydroxyl groups. The sensor chip was used shortly after oxygen plasma cleaning which oxidizes organic residues from the surface and regenerates the hydroxyl groups.[110]. This is an important point regarding the sensitivity of the surface. When exposed to air over time and also with repeated experiments the sensitivity of the sensor ($d\psi_{BG}/dpH$) decreases as the density of the surface hydroxyl groups decreases due to contamination. Minimizing the time delay between the plasma cleaning step and the experiment decreases the

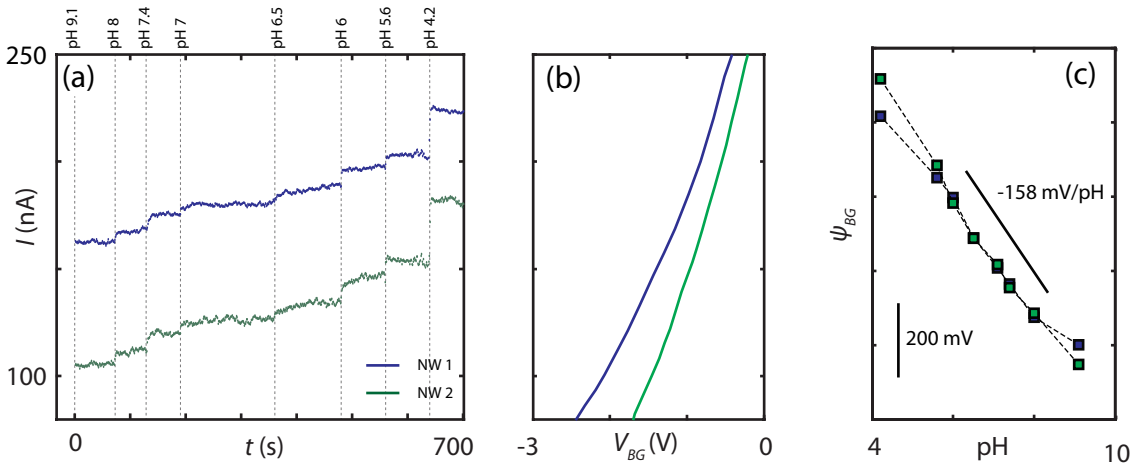

Figure 4.11.: (a) Current response from the two NW sensors (green, blue) with changes in pH using a ten times diluted buffer (10X). Vertical dashed lines mark the introduction of a new buffer with a different pH value. (b) The corresponding back gate trace for the NWs. (c) These traces are used to convert the stable baselines into a corresponding potential. The offset at pH 7 is subtracted.

extent of surface degradation. As we shall show later (See Fig. 4.18), storing the chips in a closed container also preserves the surface sensitivity (See Appendix A).

The following measurements were performed a day after the previous set. The sensor was left soaking in MQ water overnight. Fig. 4.11 a shows pH steps using a 10 fold diluted buffer (10 mM PBS, 10X). Diluting a buffer leads to a reduced buffer capacity [93] and we see its effect in the form of reduced sensor stability. Slower signal stabilization with a pH step is observed. The $\Delta\psi_{BG}$ corresponding to a stable pH baseline is shown in Fig. 4.11 c. The traces show similar sensitivities ($d\psi_{BG}/dpH$) over the pH range. A slight increase in sensitivity observed around pH 7 can be attributed to a decrease in the double layer capacitance at lower electrolyte concentrations in the buffer (See Sec. 2.4.3 and Sec. 2.5). At pH values far from 7, a decrease in sensitivity is observed with a slight sigmoidal trend and this is indicative of lowering of the surface group density.

We conclude that the new fluidic chamber used in these experiments offers a stable environment in which the sensor response is shown to be stable and reproducible. A linear $\Delta\psi_{BG} - pH$ trend is observed in the first round of measurements which degrades to a slight sigmoidal trend the next day. Diluting the buffer results in a slight increase in the sensor sensitivity, however the sensor signal stability is affected.

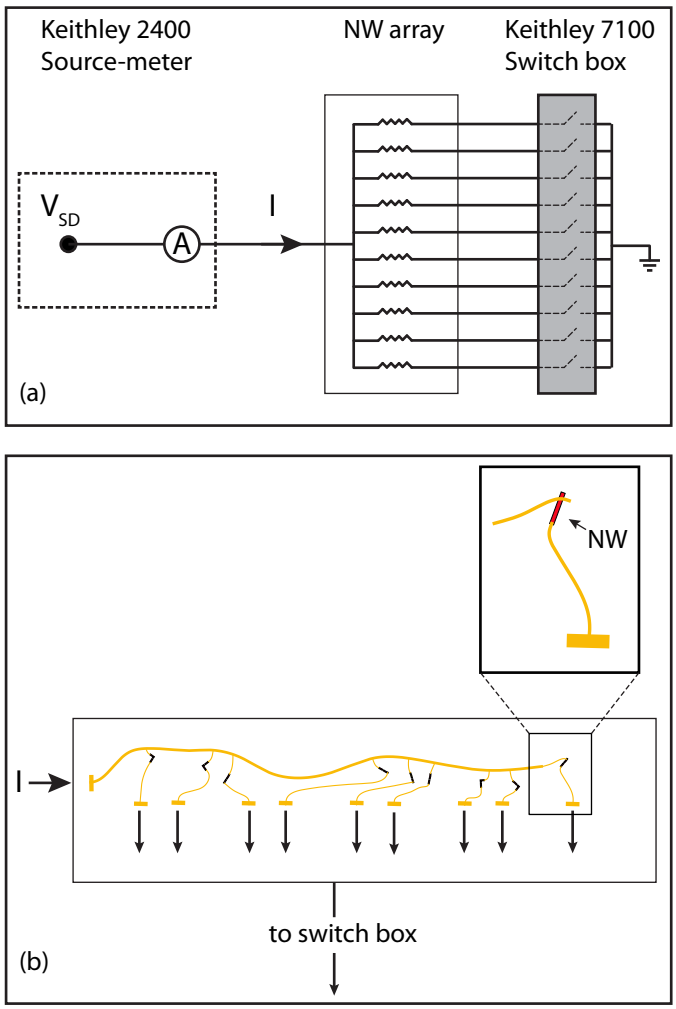

Figure 4.12.: (a) Schematic of the measurement setup for measuring on multiple nanowires with a single current meter. (b) Scheme showing the electrical connections (gold) to nine NWs (red). All NWs share a common source bias electrical line and have individual connections to the drain via a 1:10 multiplexer/switch. Inset shows magnified portion of the design with connections to single NWs.

Finally, this method of parallel measurements is limited by the number of available measurement instruments.

4.2.3. Multiple sensors - sequential measurement

The simultaneous measurements on multiple NW sensors presented in this chapter till now, were done using multiple voltage bias sources and current amplifiers. Such a setup is not easily scalable with increasing number of NW sensors. Thus an alternate measurement scheme, shown in Fig. 4.12 is used. A single voltage source-drain bias source and a current amplifier (or a single source-meter, Keithley 2400) is used to measure current through several NW sensors in a cyclic manner using a relay switch box (Keithley 7001 with a Keithley 7166 switch card[4]). Contrary to the previous measurements discussed till now, the following measurements were performed with a liquid gate (LG) immersed in the solution and fixed in position within the mixing chamber. The liquid gate defines and maintains the solution at a definite potential. The back gate was tested during the electrical probing of the NW devices prior to bonding but was not electrically connected for the sensing experiments. It is left at a floating potential with the sensor chip glued to the chip carrier using photoresist. The solution in the mixing chamber is evacuated using a peristaltic pump connected via tubing to a fresh sterile plastic pipette tip while new solution is manually pipetted in. The pipette is partially immersed in solution within the mixing chamber and fixed at a position close to the sensor surface. This is important as minor changes in the liquid gate position relative to the surface can lead to unpredictable shifts in the sensor signal baseline. The NWs have similar resistances, ~10 kΩ with the etch method yielding good quality electrical contacts to the NWs. This is in the same range as that obtained with an ammonium poly-sulphide etch.

Device parameters:

- NW diameter: ~100 nm
- Device length: ~1 μm
- Back gate oxide: 300 nm
- Etchant used: *In-situ* Ar sputter
- Device isolation: ALD Al_2O_3 @ 150 C, 20 nm

[4]The Keithley 7166 relay card uses mercury wetted electromechanical relays which ensure bounce-less switching.

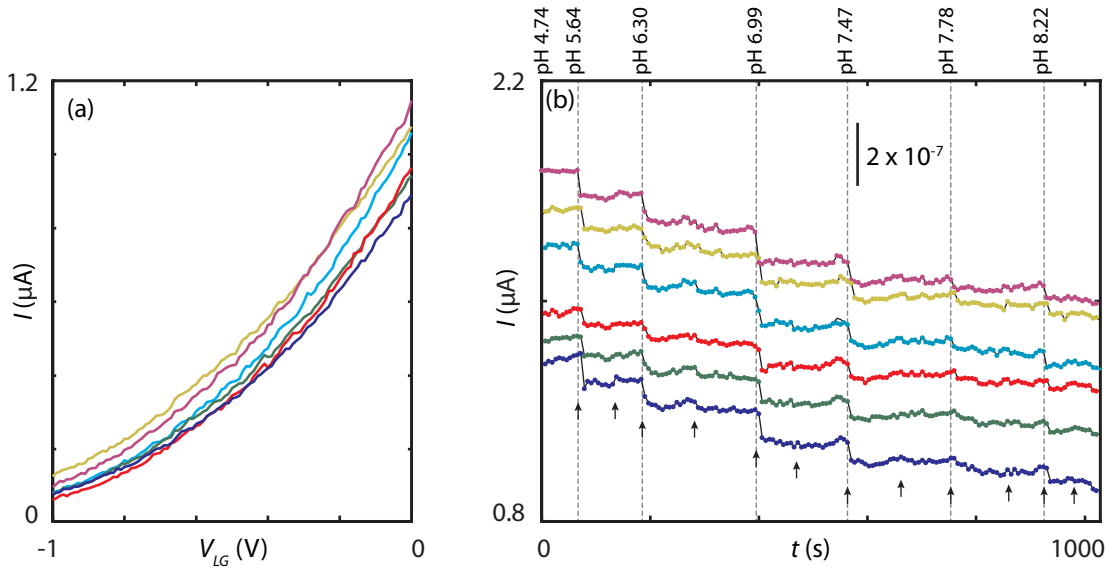

Figure 4.13.: (a) The current through the six NW devices (colors) at a source-drain DC bias of 10 mV as the liquid gate is tuned from 0 to -1 V. The devices were exposed to pH ~7 during these traces. (b) The current through the same six NW devices, measured on in a cyclic manner as buffered solutions of decreasing pH are flushed. The traces are vertically offset for clarity. Arrows mark a solution change or a repeated flush. During the pH steps the liquid gate was held at 0 V.

- Buffer: 30 mM NaP (1X) and 3 mM NaP (10X)

Fig. 4.13 show DC measurement performed at a source-drain bias of 10 mV on six NW devices. Each color represents a single NW device. The conductivity of the devices can be tuned using a liquid gate (in a buffer of pH 7.4), Fig. 4.13 a. As seen previously, flushing buffer solutions of increasing pH produces a step response (Fig. 4.13 b). The traces are offset for clarity. The signal response from each sensor is stable, with the step size larger than the noise. From the response it can be seen that a pH step of ~0.3 can be resolved[5]. All sensors respond in a consistent manner and this is quantified further next.

Fig. 4.14 a shows two liquid gate traces for the same NW taken 10 min apart. Over

[5] As a comparison pH steps of 0.1 have been resolved using NW FETs [111]. The signal to noise ratio in the sensor signal can be improved by increasing the rise time on the current amplifier from 300 ms to 1 s and also increasing the delay between switching and measurement. An overall wait+measure time of 3 s leads to less noise in the sensor response however with sequential measurement six NWs results in a given NW being measured on only once every 18 s. Thus, there is a noise-speed of measurement trade-off.

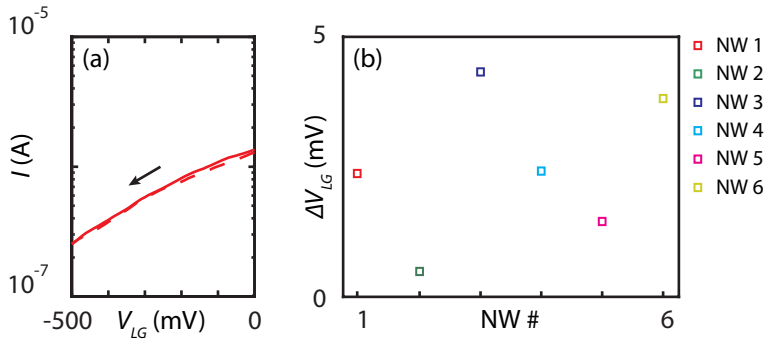

Figure 4.14.: (a) Two liquid gate traces for a single NW device, repeated 10 min apart shows them to be reproducible. (b) The average difference between the two traces for the six NW sensors is less than 5 mV.

small ranges of voltages the traces show high reproducibility. The mean difference between two repeated traces for the six NW devices (coloured squares in Fig. 4.14 b) is usually less than 5 mV. Sweeping the liquid gate over a larger range ($> 500\,\mathrm{mV}$) leads to a larger hysteresis.

Fig. 4.15 shows measurements performed a day after the previous set (Fig. 4.13), a solution of known pH (1X buffer) is flushed in the mixing chamber and once the signal response stabilizes (time trace not shown), the liquid gate is swept over a

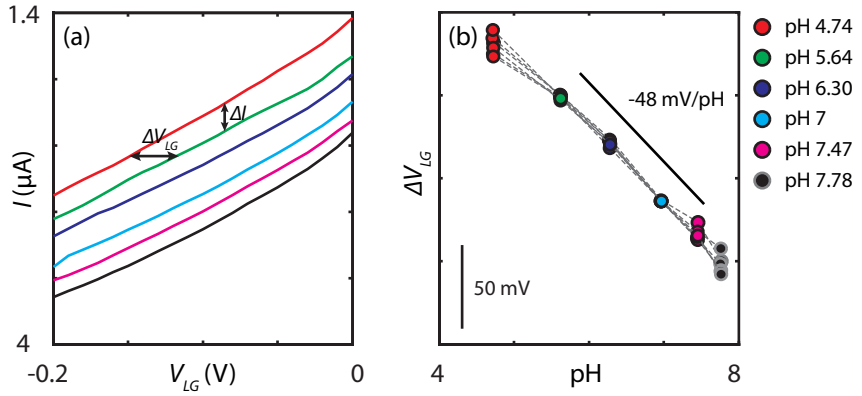

Figure 4.15.: (a) I through a single NW sensor at $V_{SD} = 10\,\mathrm{mV}$ as the LG is swept over a small voltage range at different pH values (colors) using the 1X buffer. (b) The mean ΔV_{LG} for different pH (colors) is shown for all six sensors (dashed lines). The traces are are plotted with offset at pH 7 removed.

small range (200 mV). The corresponding liquid gate traces at different pH values for a single NW device is presented in Fig. 4.15 a. Different colors correspond to different pH values. The mean shift in liquid gate potential with respect to the pH 7 is presented in Fig. 4.15 b. Each dotted line represents a different NW sensor and the colors correspond to a separate pH value. As discussed in Sec. 2.3, a shift in the liquid gate threshold is equal to the change in the surface potential. The sensor response for all six NWs is found to be ~48 mV/pH and linear around pH 6-7. The pH_{pzc} for ALD Al_2O_3 has been reported to be ~pH 7[68]. Far from the pH_{pzc} of the surface, at pH 4.74 the sensitivity is seen to decrease indicating a limited buffer capacity of the oxide surface (surface group density, N_S).

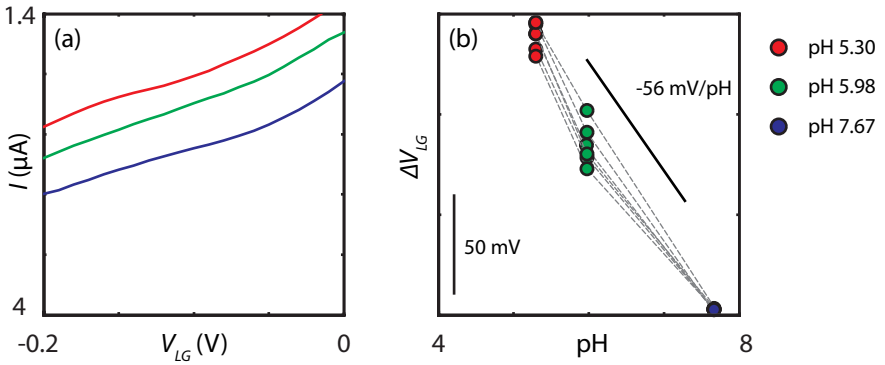

Figure 4.16.: (a) I through a single NW sensor at $V_{SD} = 10\,\text{mV}$ as the LG is swept over a small voltage range at different pH values (colors) using the 10X buffer. (b) The mean ΔV_{LG} for different pH is shown for all sensors (dashed lines) with offset at pH 7.67 removed.

Fig. 4.16 shows experiments performed a day after the previous set (Fig. 4.15), using diluted buffer solutions (10X). Fig. 4.16 a show the LG traces of a single NW sensor in three different buffer solutions (colors). The mean shift between the traces for all sensors (dashed lines) with respect to pH 7.67 is plotted in Fig. 4.16 b. The traces present an average sensitivity of -56 mV/pH, higher than that observed using the 1X buffers.

Using the maximum sensitivity of -48 mV/pH and the parameter $\beta = \frac{e^2 N_S \delta}{C_{DL} k_b T}$ from Eqn.Eqn. 2.20, the surface hydroxyl group density N_s is estimated as $\sim 8 \times 10^{16}\text{m}^{-2}$. C_{DL} is assumed to be $0.2\,\text{F/m}^{-2}$, $\delta \sim 1$ and $T \sim 300\,\text{K}$. Using the formulation discussed in Sec. 2.5 which takes into account anion complexation as well as changing C_{DL} at the two dilutions of the buffer used (1X and 10X), Fig. 4.17 shows a fit to the

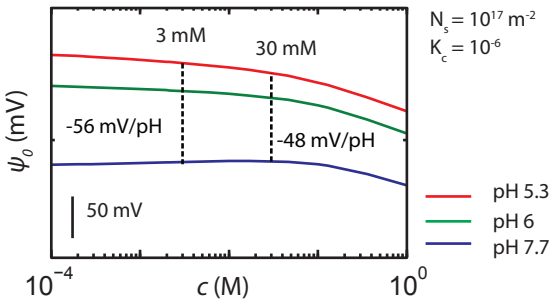

Figure 4.17.: A fit to the model discussed in Sec. 2.5. The vertical dashed lines mark the two buffer dilutions used and the corresponding sensitivity ($d\psi_0/dpH$). The three colours indicate the three different pH values. Values of $N_s \sim 10^{17}\,\mathrm{m}^{-2}$ and $K_c = 10^{-6}$ fits the data.

model and a similar value for $N_s \sim 10^{17}\,\mathrm{m}^{-2}$ is estimated. The equilibrium constant for anion complexation $K_c \sim 10^{-6}$ is found to be in the same order of magnitude as extracted by the Tarasov et al[68].

Repeated measurements over a several days typically lead to a degrading sensor performance. This is observed in the reproducibility of the sensor signal with pH steps as well as the variation in the sensitivity of the different sensors (dashed lines), Fig. 4.18 a. This can be attributed to contamination of the oxide surface. We find that cleaning the sensor chip in an oxygen plasma oven for a minute is sufficient to regenerate the surface hydroxyl groups. The treatment restores near-Nernstian sensitivity for all sensors, Fig. 4.18 b. Following the plasma cleaning, the sensor

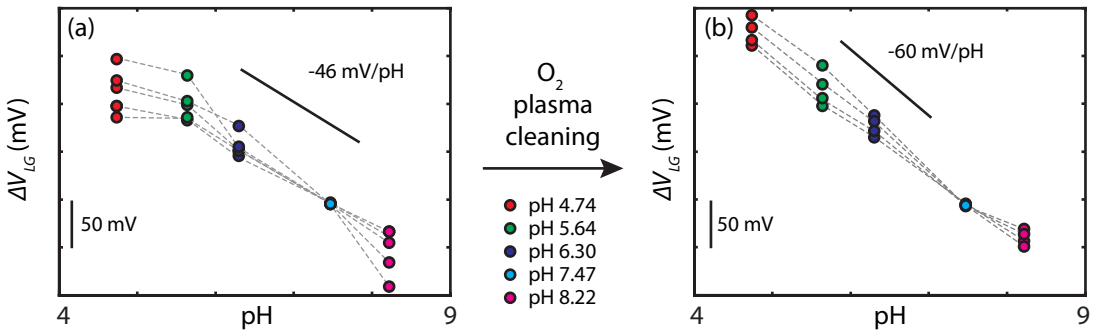

Figure 4.18.: (a) pH response of five NW sensors on the third day of measurement. (b) The post cleaning pH response. One of the five NW sensors was lost due to electrostatic discharge during the cleaning. The offset at pH 7.47 is subtracted and $V_{SD} = 10\,\mathrm{mV}$ in both cases.

chips can be stored in a closed containers with little surface degradation over time. Appendix A shows data from a sensor device that was stored such following plasma treatment and measurements on the device showed a sensitivity of $-56\,\mathrm{mv/pH}$.

4.3. Summary

In conclusion a stable platform using NWs as pH sensors has been developed. With the end goal of applying our sensors to biological interfaces we have tested and established a protocol via pH sensing that allows stable and reproducible sensor measurements. Several factors essential for stability have been discussed. The final design for the mixing chamber comprises a fresh PCR tube as well as a chemically inert O-ring. Pumps are used to evacuate solution from the mixing chamber in a reproducible manner to minimize mechanical disturbances to the setup. A liquid gate is used to maintain the liquid in the mixing chamber at a well defined potential. Finally, the use of buffered solutions is necessary as they ensure a well defined pH value. Probing the sensitivity of a chemically modified surface to pH sensing we can probe the density and homogeneity of the resulting terminal groups. All these elements are combined to avoid ambiguous changes in the sensor baseline and to provide a better understanding of the sensor response. Using the final setup we demonstrated pH sensing using multiple NW sensors with a near-Nernstian response of ∼-56 mV/pH. While longer signal averaging can improve the signal to noise ratio, a thorough analysis of noise sources is needed. In the next chapter we explore the detection of larger bio-molecules.

5. Protein sensing

Having established InAs NW FETs as a stable reproducible devices for pH sensing, we discuss its application to the detection of proteins. A common protein system consisting of biotinylated bovine serum albumin (BSA) as a functionalization layer followed by a target protein with a strong binding affinity for biotin is used to establish the proof of concept of protein sensing via its charge. Fig. 5.1 shows an idealized depiction of the scheme. The Debye length λ_D in the buffer solution is indicated by the dashed line. We shall see that protein detection is not as straightforward as pH sensing as the sensor response is highly dependent on λ_D in solution and its comparison to the relevant length scales in the system such as the protein size and the distance of the plane of binding from the surface. All aqueous solutions including the buffers as well as the protein solutions were prepared by R. Frederiksen in the group of K. Martinez. Simulations of the sensor response to protein binding were done by Luca de Vico.

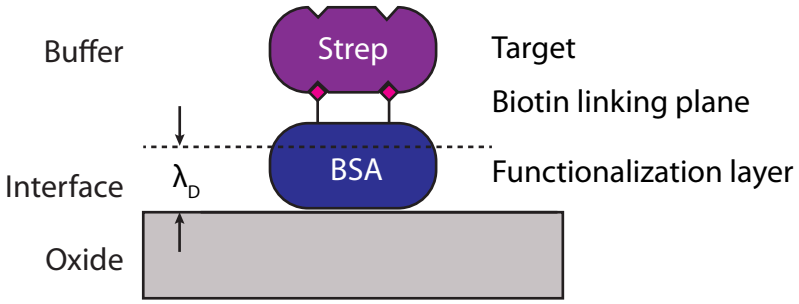

Figure 5.1.: A model scheme involving biotinylated BSA as a functional layer followed by Streptavidin as a target protein for detection. The Debye length (λ_D) for the electrolyte concentration of the buffer is depicted by the dashed line.

5.1. BSA-Streptavidin

In this section we demonstrate the electrical response of the NWFET sensor to the binding of Streptavidin to a functionalized sensor surface. The basis for the following experiment involves an initial functionalization of the sensor surface with biotinylated BSA followed by the addition of the protein of interest, here Streptavidin. We choose the BSA-biotin/Streptavidin system for the following reasons. Streptavidin has a strong affinity for Biotin and this has been utilized in several biosensor schemes[8,9,71] with silane based surface modification. BSA is a soft protein which can adsorb to surfaces even under unfavorable conditions[8,112,113] such as electrostatic repulsion due to the entropy gain due to conformational change upon adsorption. Compared to the pre-experiment silanization treatment of the sensor surface (See Sec. 3.4.2) involving an overnight curing step, incubation of a solution of biotinylated-BSA ($\sim\mu g/ml$) offers a way of immobilizing biotin at the surface with a short (~20 min) incubation time[114] during the the experiment itself. The surface coverage via this functionalization scheme on the ALD oxides used was investigated[115] and found to be high while the non specific binding of Streptavidin (Avidin) in the absence of surface biotinylation was low.

The crystal structure, and thus the internal distribution of charges within BSA is not known however its dimensions are approximated as an ellipsoid, ~ 4 x 4 x 14 nm[116]. Streptavidin is a well characterized protein with a known crystal structure and in its tetrameric form can be thought of a cuboid of dimension ~5.5 x 5.7 x 4.6 nm[94,117]. BSA and Streptavidin have an isoelectric point pI (pH at which the molecule is overall neutral) of 4.7[118] and 5-6[119] respectively. We use a 30 mM sodium phosphate buffer solution at a pH of 7.4. As convention, 1X represents the original undiluted buffer, while 10X and 100X denote 10 and 100 times dilution of the same. All buffers were confirmed to have the same pH. At this pH both proteins have an overall negative charge.

The following DC measurements were performed on three NWFET sensors fabricated in an identical manner as the devices mentioned in Sec. 4.2.3. A fluidics setup similar to the one described in Sec. 4.2.3 and shown in Fig. 3.10 is used. An Ag/AgCl electrode immersed in a saturated KCl solution and encased in plastic tubing with a porous ceramic frit at the end is used as the liquid gate. This gate, inserted into the solution mixing chamber, maintains the solution at a fixed potential. The porous frit connecting the KCl solution with the buffer solution outside, does not let

through large molecules such as proteins which can interact with the electrode and cause shifts in the sensor response[44]. A pump is used to evacuate the mixing chamber while fresh solution is manually pipetted in. We find that fixing the position of the liquid gate as well evacuating solution in a reproducible manner is essential for maintaining a stable sensor baseline as well as avoiding ambiguous jumps in response.

As discussed in Sec. 2.5, a varying salt concentration can lead to a change in the sensor response even for the same pH. In comparing sensor response in various buffer dilutions, after protein adsorption, it is difficult to separate the influence of the protein from the effect of electrolyte interaction with the surface without a parallel control experiment[26]. Alternatively, it is easier to examine the sensor response to protein adsorption by comparing baselines before and after protein incubation for a given buffer dilution.

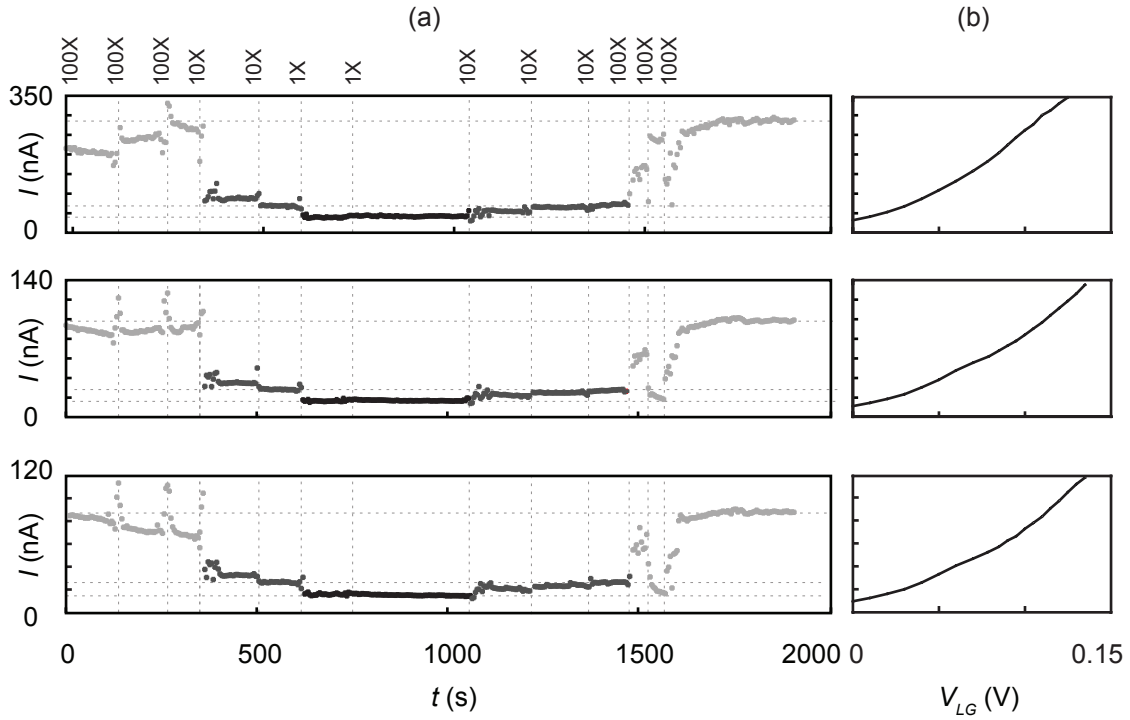

Figure 5.2.: (a) Cyclic DC measurement shows I through three NW sensors as solutions of varying dilutions are flushed into the mixing chamber. The step like response as the dilution is changed from 100X to 1X and then back to 100X demonstrates reproducibility. All solutions have the same pH of 7.4. (b) The corresponding liquid gate traces used to convert current to an equivalent liquid gate potential.

To demonstrate the reproducibility and stability of the sensor response we perform solution flushes from 100X to 1X dilutions and then back to 100X (Fig. 5.2 a). The different dilutions are marked in different shades, ranging from grey to black. Each solution is flushed multiple times to establish and confirm a reproducible baseline. The baseline for the 100X dilution (light grey) exhibits a small transient settling response lasting upto several seconds and is expected given its reduced buffer capacity through dilution(See Lloret et al[93] as well as Fig. 2.8). With repeated solution exchanges the corresponding baseline is seen to be reproducible. The 1X (black) and 10X (dark grey) traces do not show any transient behaviour and settle to the new baseline sharply. Using the liquid gate trace (Fig. 5.2 b) to convert current to an equivalent liquid gate potential, the steps are found to be reproducible within 5 mV.

Having established reproducibility of response with varying electrolyte compositions, we proceed to protein detection. We start by adding buffers of known electrolyte concentrations (1X, 10X and 100X, Fig. 5.3 a). With multiple solution flushes, the sensor baseline is checked to be stable and reproducible. At around t = 1200 s, we introduce a 0.1 μg/ml solution of BSA (red trace) in the undiluted buffer (1X). After ~1500 s of incubation, the solution in the mixing chamber is flushed, washing away excess unbound protein and the three buffers dilutions baselines are established. This is followed by the addition of 100 nM solution of Streptavidin (blue trace) made in the undiluted buffer (1X). After ~1000 s of incubation, the mixing chamber is flushed, washing away unbound protein and the three buffer dilution baselines are established.

A step response with changing buffer dilution is observed Fig. 5.3 a with the 100X trace (light grey) showing a larger settling time. The step from 100X to 1X at $t \sim 1100\,\mathrm{s}$ shows a sharp change and the sensors settle into the same level as at $t = 0\,\mathrm{s}$. The red trace marks the incubation of BSA and a slow equilibration curve is observed. The sensor signals in the 1X buffer have always shown sharp step changes with no visible drift, the slow change in sensor response can be attributed to the binding of BSA to the surface. At $t \sim 3000\,\mathrm{s}$flushing the different buffer solutions stabilizes the signal. A visible decrease can be seen in the sensor baselines for the 100 X (light grey) traces before and after BSA incubation. Contrary to the incubation of BSA, at $t \sim 4000\,\mathrm{s}$ the incubation of Streptavidin (blue trace) does not produce a visible binding curve in either of the three sensors. However, the subsequent buffer flushes show a further decrease in the baselines, particularly for

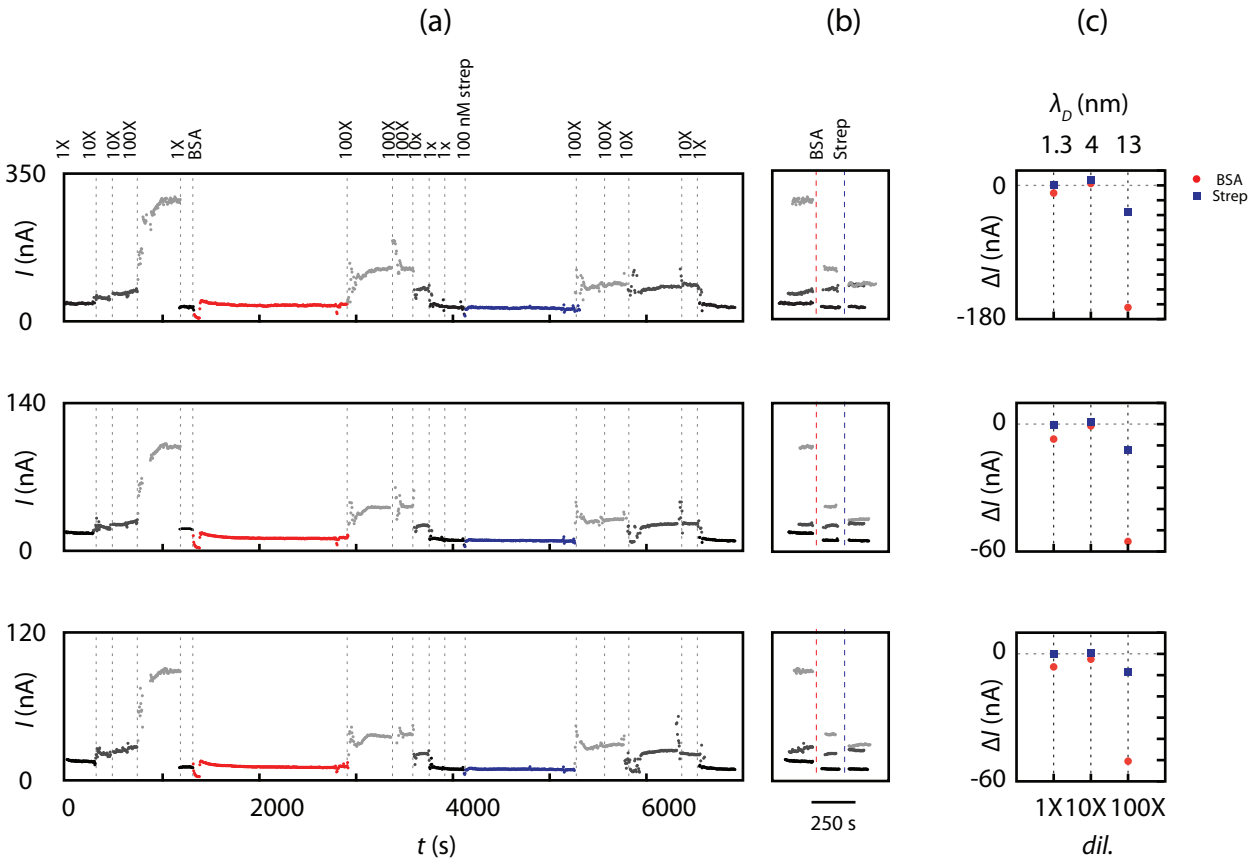

Figure 5.3.: (a) I at $V_{SD} = 10\,\text{mV}$ through the three NW sensors with the incubation of protein (BSA (red), Streptavidin (blue)) and the subsequent buffer solution flushes. (b) The stable baselines before and after protein incubation from (a) are shown. (c) ΔI as a function of dilution. The dilutions and the corresponding λ_D are shown on the x-axis.

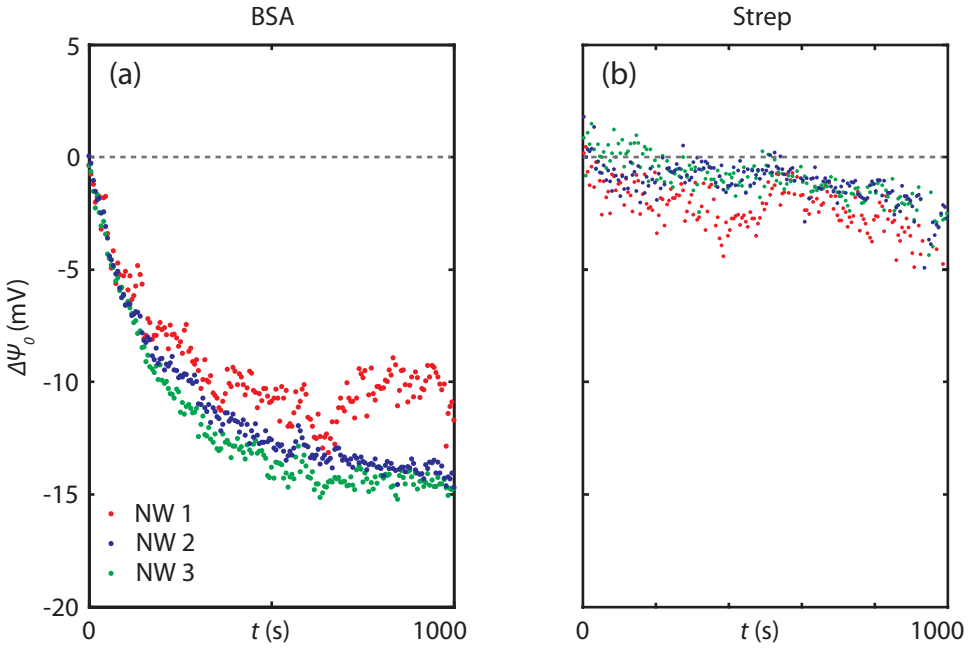

Figure 5.4.: Sensor response to the binding of (a) BSA and (b) Streptavidin from Fig. 5.3 a. Both solutions were prepared using the undiluted buffer (1X). ΔI from the three NW sensors (colours) is converted to the change in surface potential ($\Delta\psi_0$) via the relevant liquid gate trace (not shown). $t = 0$ s corresponds to the introduction of the protein solution in both cases and the offset is subtracted so the curves start at $\Delta\psi_0 = 0$ at t = 0.

the 100X trace.

The stable current baselines in Fig. 5.3 a, before and after protein addition are extracted and presented in Fig. 5.3 b. Qualitatively, a large change in the sensor response is observed due to BSA (and Streptavidin) incubation for 100X dilution compared to 1X and 10X. A combination of changing double layer capacitance and anion complexation with the surface (Sec. 2.5) leads to increasing current baselines with dilution, evident before BSA incubation. The change in the baseline current (ΔI) with the addition of BSA (red circles), and also after Streptavidin (blue squares) for all three NWs is shown in Fig. 5.3 c. In the simple model where the protein is treated as a single charge at a fixed distance from the sensor surface, binding of a negatively charged protein should result in decreased current. Though the magnitude of response of the three sensors is varied, they all present the same

trend - a clear response for 100X and a comparatively smaller response at 1X and 10X dilutions and (Fig. 5.3 c). In order to quantify and compare the responses, ΔI is converted to $\Delta\psi_0$ as before (Fig. 5.2 b, Sec. 4.2.3) and the response for all three NWs is plotted together in Fig. 5.5. The responses of the three sensors are now seen to be consistent and of similar magnitude.

Fig. 5.4 shows the sensor response, converted to the change in surface potential, during the incubation of BSA and Streptavidin. All three sensors present a similar response to BSA, with a decrease of ~15 mV in surface potential after 1000 s. In contrast, the Streptavidin binding barely influences the sensors with the signal change comparable to the noise. This is expected with λ_{D} ~1.3 nm[1], lower than the smallest dimension of BSA, while Streptavidin binding plane is further from the sensor surface.

We shall first examine the BSA response (red circles). For the undiluted buffer (1X, $\lambda_{\mathrm{D}} = 1.3\,\mathrm{nm}$) a potential drop of ~5-10 mV is observed. This is lower than the drop (~15 mV) seen in the binding curve in Fig. 5.4 a and may arise due to washing away of weakly bound proteins/bilayers at the surface. This could also be just due to the ~5 mV limit of reproducibility of sensor response. For the 10X dilution, ($\lambda_D = 4\,\mathrm{nm}$) an overall positive response is observed consistently for all three sensors. Finally, for the buffer of the highest dilution (100X, $\lambda_D = 13\,\mathrm{nm}$), we see an overall negative response. Depending on the orientation of the BSA bound on the surface, the thickness of the functionalization layer can vary from 4 to 10 nm. For λ_D smaller than the protein dimensions, charges within the protein structure closer to the sensor surface will have a larger influence than charges further away and can result in a net influence opposite in polarity compared to the overall protein charge. When λ_D becomes comparable to the size of the protein, the sensor should respond to the overall negative protein charge. Thus for λ_D ~13 nm, the full charge of the BSA molecule is expected to affect the sensor and $\Delta\psi_0$ should be negative. Without knowledge of the spatial distribution of charges within BSA it cannot be stated with certainty that the sign reversal of the sensor responses for 10X dilution is due to charges in the extremities of the protein, lying close to the sensor surface.

The change in potential due the binding of Streptavidin is shown in Fig. 5.5 b (blue squares). As expected, at low Debye lengths (1X, $\lambda_D = 1.3\,\mathrm{nm}$) the average sensor response is centred around 0 mV since the protein is removed from the sensor surface

[1] λ_{D} in the 1X solution is around 1.3 nm and we expect a similar value for the protein solution in the same buffer.

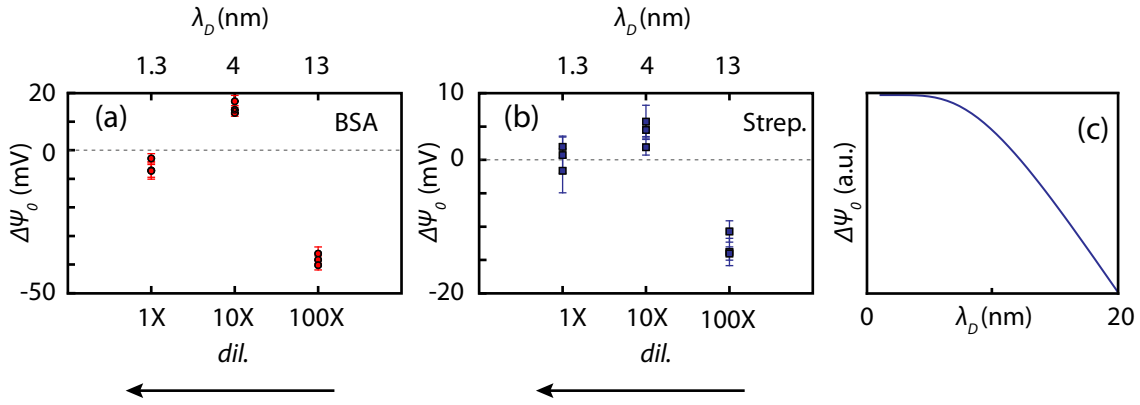

Figure 5.5.: ΔI is converted to a change in the equivalent liquid gate potential (or surface potential ($\Delta\psi_0$)) via the corresponding liquid gate traces (Fig. 5.2 b) for (a) BSA (red) and (b) Streptavidin (blue) incubation. (c) Using a protein charge distribution model[94], the expected change in surface potential with the binding of Streptavidin as a function of λ_D is shown. Arrows indicate the order in which the different buffer dilutions were flushed.

being bound on BSA. This is also evident in the lack of a clear sensor response to the incubation of the Streptavidin in Fig. 5.4 b. For the next dilution (10X, $\lambda_D = 4$ nm), the response is close to a rise of 5 mV but may not be significant given the reproducibility of sensor response (~5 mV, Fig. 4.14). For the highest dilution (100X, $\lambda_D = 13$ nm), as in the case of BSA with Debye length becoming comparable to the height of the protein from the surface we see a distinct drop in surface potential of about 12-15 mV, consistent for a overall negatively charged protein.

Simulations[2] performed by Luca de Vico[94] shown in Fig. 5.5 c show that in the simplified model of the protein (Streptavidin) as a spatial distribution of charge, the sensor signal should only monotonically decrease (become more negative) with increasing dilution. The model is only used to gain a qualitative overview of the protein interactions with the sensor since the former does not take into account device details such as spatial variation of carrier density within the NW and varying transconductance.

We conclude that at the highest dilution of 100X, the sensor response is consistent with the overall charge of the proteins binding at the surface and by tuning the Debye length the strength of the response can be controlled. A consistent response

[2]For the simulation, the program PROPKA[95,120] uses the protein structure from protein data banks to compute the pKa of the ionizable amino groups on the protein, and thus for a given pH, a spatial charge distribution can be obtained.

is seen across the three sensors as well as for two negatively charged proteins. We observe a binding curve during the incubation of BSA and with the correct choice of λ_D binding of target proteins to the functionalization layer could be observed. In the following sections we present measurements performed on the same sensor chip using a positively charged target protein.

5.2. BSA-Avidin

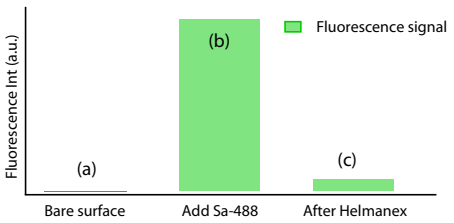

Figure 5.6.: Fluorescence analysis of a piece of (a) Si chip that was (b) functionalized with biotinylated BSA and then Avidin and (c) finally cleaned using a 2% Helmenex solution in MQ water. This analysis is based on images shown in Fig. B.1.

In this section, we demonstrate the binding of positively charged Avidin to a functionalized sensor surface. This is important to establish that the sensor responds to the charge of the protein. If the charge of the protein is transduced into a sensor response, then oppositely charged proteins should result in opposite trends.

In this scheme, the sensor surface is functionalized with biotinylated BSA and followed by the addition of the protein of interest, Avidin. The latter has a $pI \sim 10$[119] and is positively charged at the pH of the buffers used. The dimensions of its tetramer form are ~6.4 x 6.6 x 4.8 nm[95,121]. As before, BSA is negatively charged at the pH used. The sensor chip presented in the previous section is reused following a cleaning step[3]. A 30 mM sodium phosphate buffer with a corresponding Debye length of ~1.3 nm is used. The undiluted buffer is referred to as 1X while 10X and 100X refer to the ten and hundred fold dilution of the same, with a corresponding Debye length of 4 and 13 nm respectively. All solutions had a pH of 7.4.

[3]We use the same chip as discussed in Sec. 5.1. The sensor chip was rinsed with MQ water followed by a 30 min soak in a 2% solution of Helmenex in MQ water and finally rinsed with MQ water for 30 min using a pump to flush the mixing chamber continuously. Ideally, the sensor chip should be cleaned in an oxygen plasma oven, however plugging/unplugging the sensor chip comes with the risk of electrostatic discharge which can blow up the NWs.

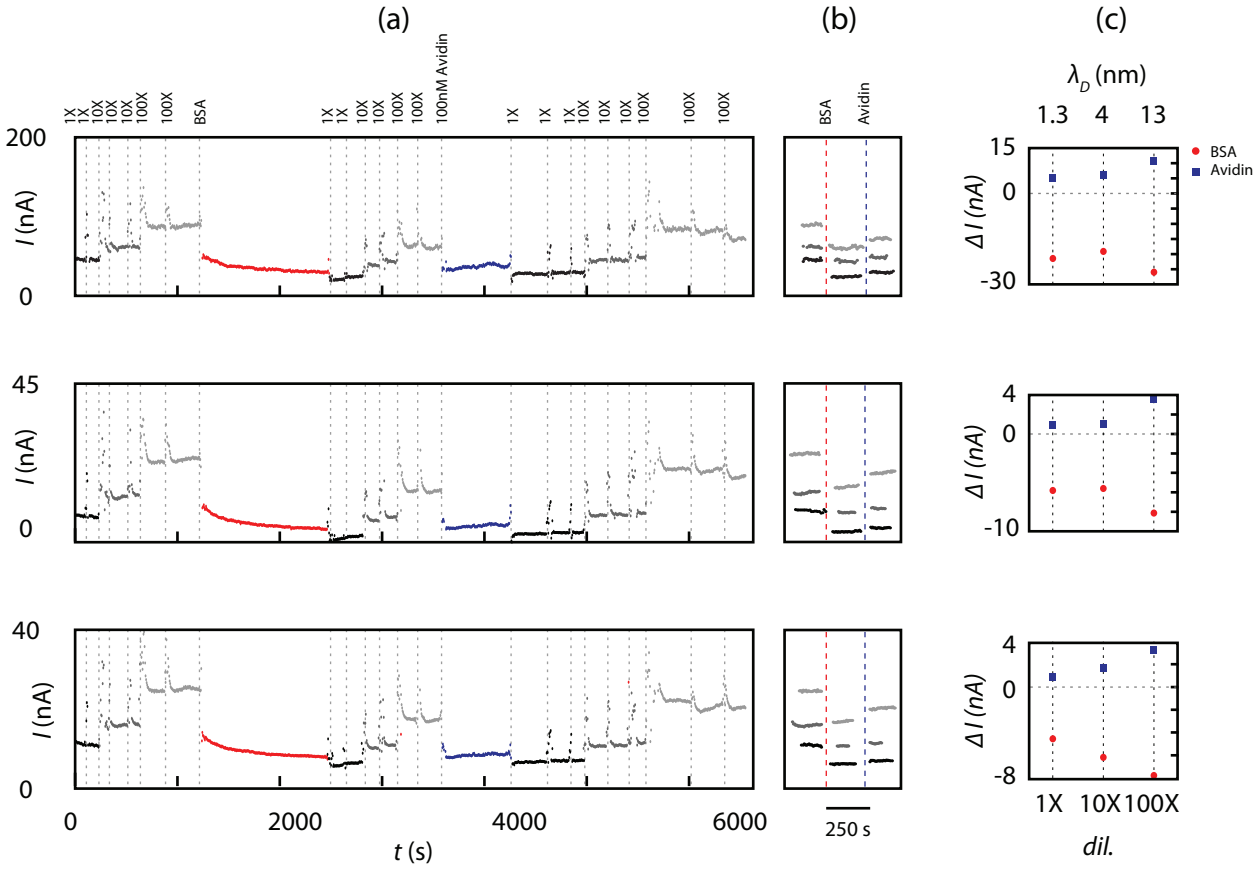

Figure 5.7.: (a) I at $V_{SD} = 10\,\text{mV}$ through three NW sensors measured in a cyclic manner as different buffer solutions are flushed and proteins are added. Three buffer dilutions with the same pH are used - 1X (black), 10X (dark grey) and 100X (light grey). The sensor response to BSA (red trace) and Avidin (blue) is highlighted. (b) The stable baselines from (a) are extracted and presented for visual comparison of the effect of protein incubation on sensor response. (c) The change in the sensor current (ΔI) for the three buffer dilutions for BSA (red squares) and Avidin (blue squares) incubation.

In order to test the cleaning procedure, a Si chip is functionalized with biotinylated BSA followed by the addition of Avidin, labeled with a green fluorophore (Alexa 488). The fluorescence signal from the chip before and after protein incubation as well as after the Helmenex rinse is shown in Fig. 5.6. The decrease in the signal intensity could indicate the removal of the target protein in the cleaning step.

Using the same fluidics setup, DC measurements are performed as in the previous section on the same three NW sensors, Fig. 5.7. The measurement protocol is the same as before. The three buffer dilution baselines are established (shades of grey), followed by the addition of 0.1 μg/ml solution of BSA (red trace) in the undiluted buffer. After incubation for ~1000 s, excess protein is washed away with buffer flush and the buffer dilution baselines are established. This is followed by the addition of 100 nM solution of Avidin (blue trace) in the undiluted buffer. After ~500 s of incubation, the solution is evacuated and the buffer baselines are established.

A step response is seen as buffers of increasing dilution are flushed into the mixing chamber, Fig. 5.7 a. As seen previously, the 100X trace (light grey) shows a small transient settling response in comparison to the sharp settling response of the 1X (black) and 10X (dark grey) traces. The red trace at $t \sim 1100$ s marks the incubation of the functionalization layer, biotinylated BSA. A binding curve is seen. As before, this slow equilibration curve can be attributed to the binding of the protein at the surface since the 1X buffer traces have always shown sharp step responses upon flushing. The subsequent flushing of the buffer dilutions shows an overall decrease in the baselines, easily visible in the 100X trace. The blue trace at $t \sim 3500$ s marks the incubation of Avidin. A magnified view of the binding traces are presented in Fig. 5.8. The subsequent buffer flushes show an increase in the baselines compared to before Avidin incubation.

Fig. 5.8 shows a magnified portion of the sensor response during the incubation of the proteins, BSA and Avidin. The raw sensor response, I is converted to an equivalent liquid gate potential with the offset at the introduction of the protein subtracted. During BSA incubation, the surface potential in Fig. 5.8 a decreases by ~25 mV in 1000 s. The binding curve is qualitatively different from that in Fig. 5.4 with a larger decrease in potential which does not saturate in 1000 s and this may indicate different interaction kinetics of the protein with the surface. During the incubation of Avidin, an opposite trend in the binding curve is observed (Fig. 5.8 b) - an increase of ~5 mV in potential. The change in surface potential as a function

of λ_D is discussed next.

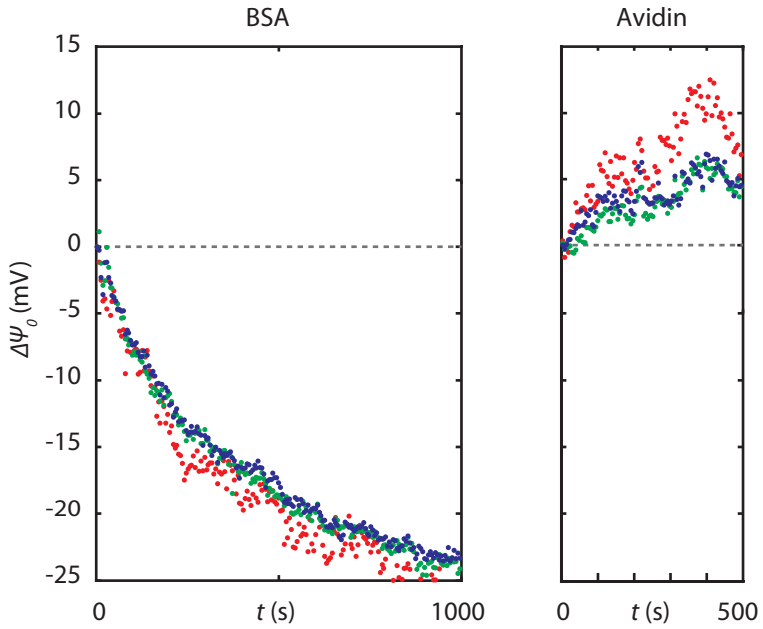

Figure 5.8.: Sensor response to the binding of (a) BSA and (b) Avidin from Fig. 5.7 a. Both protein solutions were prepared using the undiluted buffer (1X). The current response (ΔI) of the three NW sensors (red, green and blue) is converted to the change in surface potential ($\Delta\psi_0$) via the relevant liquid gate trace (not shown). t = 0 s corresponds to the introduction of the protein solution in both cases and the offset is subtracted so the curves start at $\Delta\psi_0 = 0$ at t = 0.

Fig. 5.7 b shows the extracted stable current baselines (I), before and after the incubation of BSA and Avidin, allowing for visual comparison of the effect of protein incubation. The corresponding change in the baseline (ΔI) at different λ_D, for the three NW sensors is depicted in Fig. 5.7 c. As seen earlier, though the magnitude of response (ΔI) varies across the sensors, they present the same trend - increasing $|\Delta I|$ with increasing λ_D. To qualitatively compare sensor responses, ΔI is converted to $\Delta\psi_0$ and presented in Fig. 5.9. The sensor responses are now seen to be consistent and similar in magnitude. The response to the incubation of BSA (red circles) is discussed first. BSA is negatively charged at pH 7.4 and a decrease in current (surface potential) on binding is expected. Following the incubation of BSA, the buffer dilutions are flushed sequentially from 1X to 100X. For the 1X buffer, a drop of ~22 mV in potential is seen, consistent with that observed in the binding trace[4]

[4]Both protein solutions were made in the undiluted buffer and the Debye length in these solutions

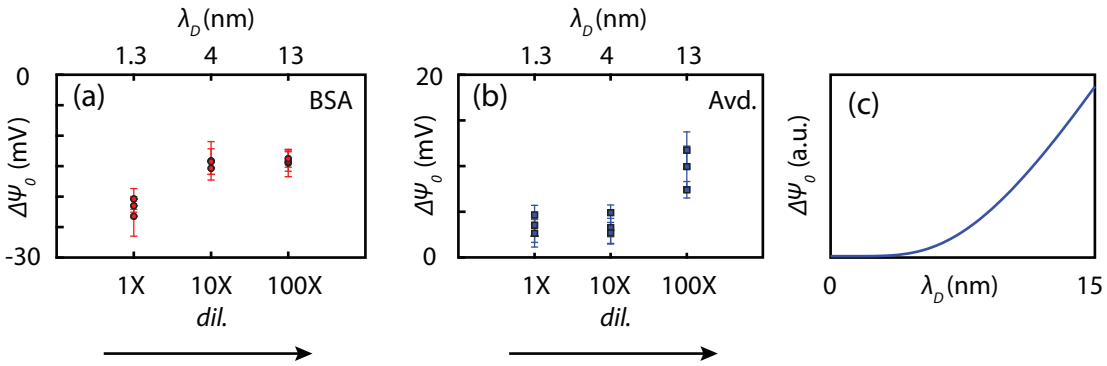

Figure 5.9.: The change in the sensor current (ΔI) is converted to a change in the equivalent surface potential ($\Delta\psi_0$) via the corresponding liquid gate traces (not shown) for (a) BSA (red squares) and (b) Avidin (blue squares) incubation. (c) Using a protein charge distribution model[94], the expected change in surface potential with the binding of Avidin to the sensor, as a function of λ_D is seen to increase monotonically. Arrows indicate the order in which the different buffer dilutions were flushed.

(~25 mV, Fig. 5.8 a). With the subsequent buffer flushes (10X, 100X) a smaller drop of ~14 mV is seen. Given the similar Debye lengths of the buffer solutions used as in the previous section, a similar trend (Fig. 5.5 a) in $\Delta\psi_0$ is expected. Instead, a large signal change at 1X followed by a decreasing response at higher dilutions is seen[5]. It should be noted that we do not understand the nature of the sensor surface and the leftover contaminants following the cleaning procedure. One possible explanation is that the binding affinity of BSA may be lower compared to same for a pristine oxide surface and as a result, part of the bound BSA gets washed away in the subsequent solution exchanges. Nevertheless, an overall decrease of surface potential after BSA incubation even at the highest dilution (100X) indicates the presence of a negatively charged molecule at the surface.

Positively charged Avidin upon binding to the sensor surface should result in an increase in the sensor current (surface potential), opposite to that observed with BSA. Following the incubation of Avidin, an increase of ~4 mV in the 1X buffer baseline is observed. This increase is consistent with increase in potential observed in the binding curve, Fig. 5.8. For the next higher dilution, 10X, a similar increase in potential is seen. While the sensor response for these two dilutions lies on the

should be close to that in the original buffer, ~1.3 nm.

[5] A similar trend in the surface potential after the incubation of BSA is observed in another experiment with the same chip (Fig. B.4).

edge of its reproducibility, at 100X dilution a clear increase of ~10 mV is noted. Simulations[6] for FET sensor response with the binding of Avidin at different λ_D show the signal to monotonically increase with increasing dilution as seen in Fig. 5.9 c. Avidin has a higher absolute charge than Streptavidin at pH 7.4[95], however the overall sensor response also depends other factors such as average distance of binding of the target protein, and surface coverage.

We can conclude that sensors respond to the charge of the protein. With the incubation of negatively charged BSA, a decreasing sensor response in the form of a binding trace is observed. The baselines for the three buffer dilutions also show a negative shift. Avidin incubation on the other hand, positively charged at pH 7.4, results in an increase in potential seen as a small rise of ~5 mV in the binding curve. This trend is also observed in the baseline shift for the different buffer dilutions. The baseline change due to Avidin increases with dilution as a larger part of the protein charge begins to influence the sensor.

5.3. Summary

Data presented in this chapter was the result of experiments on several generations of devices (See Appendix D). Our main obstacle till now had been the stability of signal, small signal response to protein incubation as well as ambiguous shifts in the signal baselines. Protein binding is limited by the diffusion of the species to the sensor surface, and protein concentrations in the low pM range may require incubation on the order of hours[16,23], making signal stability an important factor. Special attention is paid to solution exchange, using a pump to evacuate the solution and a liquid gate to maintain potential. The liquid gate protected from the solution by a porous ceramic frit ensures minimal interference of the protein with the electrode and any signal change can thus indicate interaction of the protein with the sensor surface.

By demonstrating opposite trends with oppositely charged proteins, we have reasonably established that the sensor responds to the charge of the protein. The magnitude of sensor response can be thus tuned by controlling the ionic concentration of the buffer solution. For Debye lengths comparable to the size of the protein and the position of binding, the spatial distribution of charge within the

[6]Simulations were performed by Luca de Vico as in the previous section.

protein may become relevant in trying to understand the sensor response. Large Debye lengths (low ionic concentration) typically obtained by diluting the buffer come with a trade-off of signal instability due to lowered buffer capacity. Typically this can be managed with more frequent solution exchanges, ideally with a pump driven closed solution chamber.

While we have demonstrated the detection of Avidin and Streptavidin in 100 nM solutions, this is not the limit of detection of the system (See Fig. 5.5 and Fig. 5.9) with the sensor responses larger than spread in device-to-device variation. Others (see Table. 1.1) have shown detection of much lower (fM-pM) concentrations using similar protein systems (Silane-biotin + Streptavidin or Avidin). Further experiments will focus on determining the lower limit for our system. We have established a stable platform with proof of concept demonstration of protein detection. With a correct choice of Debye lengths, this can be applied to other protein system to study interactions, binding rate, etc.

6. Transport in *p*-doped InAs nanowires

6.1. Overview

With enhanced control over their growth, nanowires can be tailored with the right dopants as well as grown with radial/axial heterostructure to achieve desired properties. We present electrical measurements and characterization of Beryllium (Be) doped Indium Arsenide nanowires grown via molecular beam epitaxy. *Be* acts as a p dopant in the bulk of the nanowire, while the Fermi level pinning at the surface, a known property of InAs, leads to intrinsic n type behaviour. As a result there exists a cylindrical shell of electrons on the surface, an inversion layer and then cylindrical core of holes. Majority carriers in the nanowire can be controlled with an electric field, such as that from an underlying metal gate, thus exhibiting ambipolar behaviour. With the right combination of metals, it is possible to achieve ohmic contact to both the n and p regions in the wire. We have studied the temperature dependence of the band gap as well as the magnetic field dependence of electron/hole transport at low temperatures. Finally, we have studied electron and hole transport in the nanowires in order to evaluate respective parameters.[1]

6.2. Introduction

For the past decade there has been a tremendous effort towards realizing the potential of semiconducting nanowires (NWs) as the platform for superior device performance in electronics, sensor applications, optical components, and mesoscopic quantum devices[122–124]. For many applications InAs NWs possess desirable properties and have attracted particular focus: small effective electron masses and high

[1]This chapter has been accepted for publication in App. Phys. Lett., 2013.

mobilities combined with an electron surface accumulation layer[125–127] forming barrier free contacts to metals makes them interesting candidates for future electronics. In addition, the proximity of the electron system to the NW surface suggests an enhanced sensitivity to changes in the immediate environment, desirable for applications in nano-scale sensors[61,128]. The intrinsic confinement, a strong spin-orbit (SO) coupling and the ease of forming electrical contacts, also to ferromagnetic or superconducting metals, have made InAs NWs attractive candidates as templates for fundamental studies in mesoscopic quantum transport and leading the way to a number of key breakthroughs including the first demonstration of SO qubits in quantum dots[129], electrical tunability of supercurrents[130], and the implementation of Cooper-pair splitters[131].

Due to the natural surface accumulation layers, experimental studies of InAs NWs have, so-far, almost exclusively dealt with electrons in the conduction band. However, for many purposes the ability to hole-dope the NWs is desirable[132–134]. For example, p-n junctions are essential ingredients in electronics and optoelectronics, and hole-doping InAs NW also forces the surface accumulation layer closer to the surface, thus making such wires even more attractive for sensor purposes. Finally for the purpose of quantum transport, it was recently shown that the Hamiltonian describing the top of the valence band in the wire geometry can be directly mapped to the corresponding conduction band[135]. Thus the hole-system in InAs may offer the same rich physics as the electron system with a range of modified parameters such as a significantly larger effective mass and an order-of-magnitude increase in the SO coupling. This combined with enhanced Landé g-factor led to the suggestion of hole-doped NWs as possible hosts of Majorana fermions[135,136] superior to electron based strong SO systems studied recently[12]. The main objective of this work is to develop and characterize high quality p-doped InAs NWs as well as NW devices for low temperature transport studies of the hole-doped system.

The NWs were grown by molecular beam epitaxy (MBE) using Be as a p-dopant incorporated either through axial or radial growth. Subsequently devices were fabricated in a field-effect transistor geometry exhibiting ambipolar behaviour, thereby allowing a comparison of the electron and hole mobilities in the same sample as a function of temperature. At low temperature the electrical properties were studied as a function of voltage bias, electrostatic gating and magnetic field.

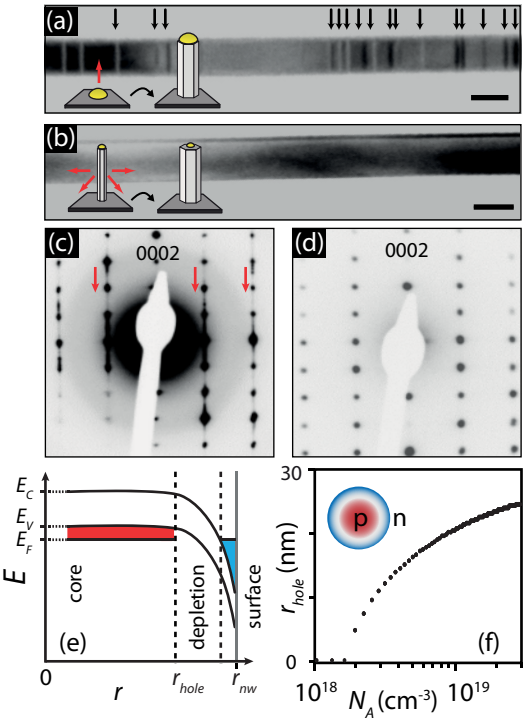

Figure 6.1.: (a) A transmission electron micrograph (TEM) of a Type A NW of diameter 60 nm and stacking fault density of $\sim$ 40 SF/μm (arrows). Type A growth schematic is shown. (b) TEM of a Type B NW ($\lesssim$ 1 SF/μm). Inset shows schematic of the two step growth. Scale bars in both panels are 50 nm. (c) Selective area diffraction images obtained from the [11$\bar{2}$0] direction shows WZ crystal structure with SFs (streaks along red arrows) for type A NWs. (d) SAD showing pure WZ structure for type B NWs. (e) Schematic band diagram along the radial direction. (f) Calculated radius of the effective hole region, r_{hole} in a NW of radius 30 nm as a function of doping density. Inset: Schematic of the electron and hole regions in a NW cross-section.

6.3. Material

Doping incorporation in planar InAs structures using high vacuum deposition techniques such as MBE, is well controlled for most dopants and the electron inversion layers on the surfaces of planar moderately p-doped InAs structures have been studied previously[137–139]. For NWs grown via the vapour-liquid-solid (VLS) mechanism[140], however, control of dopant incorporation is still not well established. Recently, there have been several approaches to growing p-doped InAs NWs, including in-situ doping with Cd[132], Zn[132], and Be[134] as well as post growth doping with Zn[141].

We have investigated Si and Be doped Au catalysed InAs nanowires grown by MBE. While Si is a known amphoteric dopant in planar GaAs and InSb[142–144] we find that the Si doped InAs NWs only exhibit n-type electrical conductivity. This confirms studies of Si doping in wires grown by metal organic vapor phase epitaxy[60] and here we only discuss the results of Be doped nanowires. Two different approaches were employed in the growth of the NWs. Type A wires were grown and doped by axial VLS growth[145] at a temperature of 425°C (Fig. 6.1 a) with a corresponding planar growth rate of 0.4 μm/hr and nominal doping level of $p = 3 \cdot 10^{19}\text{cm}^{-3}$. The NWs grow primarily with a wurtzite (WZ) crystal structure and are prone to crystal defects in the form of stacking faults (SF) (Fig. 6.1 a,c). Since the solubility of Be in Au is negligible, the doping profile depends on Be inter-diffusion through the nanowire surface. To our knowledge, diffusion data of Be in InAs is not reported in the literature but is significant in GaAs[146,147] at high temperatures. In contrast, planar growth of InAs takes place at lower temperatures with a resulting lower diffusion of Be dopants but with Be surface adatoms directly incorporating during growth possibly allowing higher doping levels. Consequently Type B wires are grown in two steps starting with thin diameter (∼25 nm) Type A NWs. The temperature is then lowered to 340°C to ensure radial growth while suppressing VLS axial growth (Fig. 6.1 b). As thin InAs NWs generally grow free of SFs[148] and the radial growth adapts to the crystal structure of the core NW[148], Type B NWs are virtually free of SF as confirmed by TEM analysis (Fig. 6.1 b,d). Fig. 6.1 e shows the expected radial band profile for a p-InAs NW. As with undoped InAs, the band bending at the surface generates a surface inversion layer[137,149,150]. The effective radius of the central hole-doped region, r_{hole} can be estimated by solving the Poisson's equation in cylindrical coordinates[101,147] and is found to depend on the NW radius (r_{nw}) and doping concentration (N_{A}). For $r_{\text{nw}} = 30$ nm, the dependence of r_{hole} on N_{A} is shown in Fig. 6.1 f. With the stated nominal doping level, we expect a p-doped region in a NW of radius 30 nm even with an order of magnitude lower dopant incorporation[147].

6.4. Quantum correction to conductivity in mesoscopic systems

To discuss the following quantum effects in a mesoscopic system we need to present certain relevant length scales. Mean free path l_e is the average distance travelled by a charge carrier between two successive elastic scattering events. These usually involve static scatterers such as impurities, crystal defects, etc and energy is conserved in such collisions. In contrast, interaction with other charge carriers as well as phonons does not conserve energy and leads to inelastic scattering. If one looks upon the charge carrier travelling through the system as a quantum wave, then there is a related phase coherence length l_ϕ over which coherence of the wave is lost. If a charge carrier travels the same path twice, then it shall have the same elastic scattering events and its phase will change in a predictable manner, i.e., it will not be randomized. However, if we consider inelastic scattering which are random themselves, the phase evolves in a statistical manner and over a distance l_ϕ it becomes random. Typically, l_ϕ is larger than l_e.

In the presence of a magnetic field B, a charge carrier travelling in a loop in the clockwise direction acquires a different phase compared to travelling the same loop in the counter-clockwise direction. Magnetic length l_m describes the length scale for which this phase difference is one flux quanta, $\phi_0 = h/e$ and thus $l_m = \sqrt{\hbar/eB}$. The last relevant length scale l_{so} involves the interaction of the spin of a charge carrier with its motion. Briefly put, it is the average distance the charge carrier travels before its spin is randomized.

6.4.1. Universal conductance fluctuations (UCF)

UCF are aperiodic fluctuations in the conductance of a mesoscopic sample with a change in magnetic field or chemical potential (source-drain bias, gate bias). These fluctuations are reproducible and depend on the disorder within the system. For a sample of dimensions smaller than l_ϕ, the amplitude of these fluctuations are zero temperature is nearly universal and of the order $\sim e^2/h$. For a 1-D system with $W < l_\phi < L$ where W, L are the width and length respectively, the system can be treated as $N = l_\phi/L$ statistically independent segments and the corresponding fluctuation amplitude $\sim \frac{e^2}{h}\left(\frac{l_\phi}{L}\right)^2$. Thus, UCF is observed when l_ϕ becomes comparable to sample dimensions, i.e., small samples at low temperatures.

6.4.2. Weak localization (WL)

WL is the result of electron interference which is seen as a decrease in the conductance of a sample due to electron localization (constructive interference). In a diffusive conductor with $l_e < W, L$ and many scattering centres, there are several ways for an electron to get from point A to B via elastic scattering events. The points A and B are taken to be closer than l_ϕ and thus phase information is retained in scattering from A to B. The probability of an electron to get from A to B $P(A, B)$ will be the summation of the probability amplitudes of all possible paths $\left|\sum_i A_i\right|^2$ where A_i is composed of a complex amplitude C_i and phase φ_i as $A_i = C_i \exp(\varphi_i)$. Thus, $P(A, B) = \sum_i |C_i|^2 + \sum_{i,j,i\neq j} C_i C_j \cos(\varphi_i - \varphi_j)$. The first term is a classical term, while the second term describes quantum interference. For a large number of paths φ_i is randomly distributed, the second term in the summation is zero and quantum interference does not affect the conductance. For $l_e < W$ it is possible for an electron to scatter and return to the starting point, forming a loop. To calculate the probability for return to point A $P(A, A)$, consider a loop traversed in the clockwise and counter-clockwise direction. The amplitude C and phase φ will be the same for the two directions. Thus $P(A, A) = |C \exp(\varphi) + C \exp(\varphi)|^2 = 4|C|^2$. The probability for a non phase coherent loop would be $2|C|^2$. This increase in probability to return to the starting point due to constructive interference results in electrons localized in loops and reduced conductance. This increased probability does not depend on the shape of the loop as long as it is smaller than l_ϕ.

Upon applying a magnetic field B the two directions of traversing a loop develop a phase difference $\Delta\varphi = \frac{2BS}{h/e} = \frac{2S}{l_m^2}$. For a given B all loops larger than $l_m$the return probability averages out and decreases to the classical sum, while for loops smaller than l_m still result in coherent back scattering reducing conductance. Thus with increasing B the effects of constructive quantum interference are undone and conductance increases. The magneto-conductance trace is seen as a symmetric curve with a minimum at zero field.

6.4.3. Spin-orbit interaction and weak anti-localization (WAL)

In an atom, the electron orbiting a nucleus experience the static electric field E from the latter as a magnetic field as $B = \frac{1}{c} v \times E$ where v is the orbital velocity. The

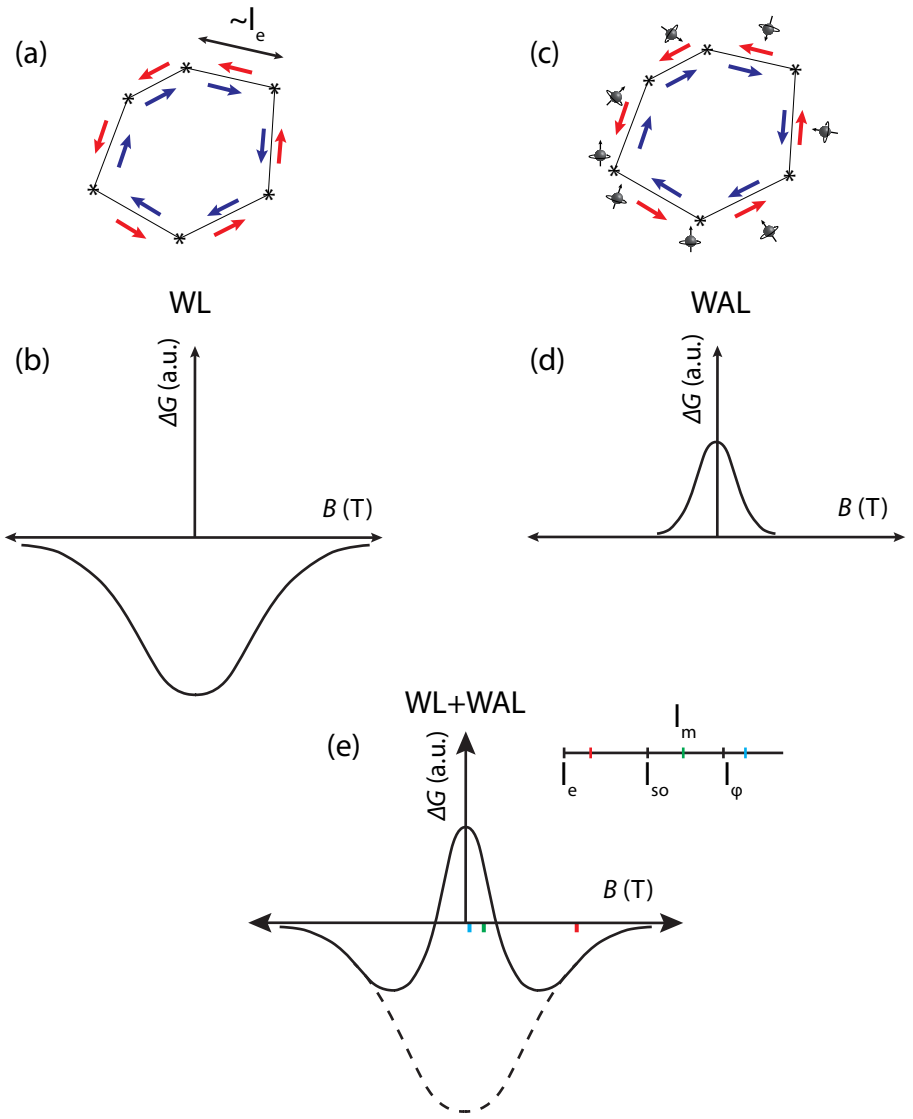

Figure 6.2.: (a) The path of an electron (hole) in a closed loop as it scatters and returns to the starting point. For loops smaller than l_ϕ, constructive interference leads to the electron being localized in the loop and this decreased overall conductance. (b) A typical magneto-conductance trace for a sample with WL shows the correction to conductance ΔG. (c) Similar to the loop shown in (a) the electron can travel in a looped path however this time due to the presence of SOI the electron spin undergoes precession and this results in an overall destructive interference. (d) ΔG is now positive and application of a magnetic field negates the effect of WAL for loops larger than l_m. (e) In materials with moderate SOI a combination of WL and WAL is observed as a peak in conductance at zero B and a minima at finite B.

magnetic moment of the electron can couple to B, linking electron spin to its orbital motion. The strength of this coupling increases in material of high atomic mass due to a larger electric field. The term spin-orbit (SO) interaction refers to the effect where the spin of the charge carrier (electron/hole) is linked to its motion. Briefly, this can arise out of electron (hole) interaction with an electric field E and is referred to as Rashba effect. In the reference frame of the electron (hole), motion through an electric field is seen as an effective magnetic field B oriented perpendicular to E as well as direction of motion, can couple to the spin of the charge thus linking spin and motion. An inbuilt electric field can arise in semiconductor heterostructures such as quantum wells and p-n junctions due to a mismatch in the Fermi levels and resulting band bending.

The effect of SOI is similar to that of inelastic scattering in that it randomizes the phase associated with the spin of the charge carrier over l_{so}. Bergmann[151] showed this results in destructive interference with a positive correction to G, and half the magnitude compared to that due to WL. In the case $l_{so} \gg l_\phi$ SOI is irrelevant and constructive interference of phase coherent electron waves in loops leads to the magneto-conductance trace seen in Fig. 6.2b (WL). For $l_{so} < l_\phi$ interesting effects arise. For loops betweenl_e and l_{so} the correction ΔG is negative while for loops between l_{so} and l_ϕ ΔG is positive. Applying a magnetic field imposes an upper limit l_m for paths that can contribute to WL (WAL). At small B with $l_\phi < l_m$ there is no effect on G. Increasing B with $l_{so} < l_m < l_\phi$ anti-localization in paths larger than l_m is affected and there is an overall decrease in G. Finally, at larger B with $l_m < l_{so}$ the localization is affected and an increase in G with B is expected. The combination of WL and WAL is thus seen as a peak in conductance at zero B and a minimum at finite B, Fig. 6.2e at which $l_m \sim l_{so}$. For strong SO materials the magneto-conductance trace resembles an inverted bell shaped curve peaked at zero B, Fig. 6.2d. Spin flips can also occur on collision with magnetic scattering centers however there is no source of such impurities in our system and we neglect this effect. Thus WAL can be used to gauge the strength of SO coupling in a material.

6.5. Fabrication

In order to fabricate devices, NWs are deposited from a suspension in Isopropyl alcohol on a Si substrate patterned with gold strip gate electrodes that are covered

Table 6.1.: Materials tested for p-type ohmic contact. The best combinations for each growth type are marked (■)

metals	Type A	Type B
Ti/Au	□	
In/Ti/Au	□	
Ni/Au	■	□
Ti/Pt/Au		□
AuGe/Au		□
Au/Zn/Au		■
Pd/Cr/Au or Pd/Au		■

by Atomic Layer Deposition (ALD) HfO_2 (grown at 90°C) Fig. 6.3 a-b. NWs are selected by optical inspection and source-drain contacts are fabricated by electron beam lithography. The native oxide on the NW surface is etched by a short dip in buffered hydrofluoric acid immediately prior to metallization. The band bending and resulting electron accumulation layer on the InAs surface makes it a challenging task to achieve good electrical contact to the hole-system in the NW core. Following previous works[149,152] several different combinations of metal layers were tested as source-drain contacts: Ti/Au, In/Ti/Au, Ni/Au, Ti/Pt/Au, AuGe/Au, Au/Zn/Au, Pd/Cr/ Au. Fig. 6.3 c compares the yield and quality of the electrical contacts when Pd and Ni were used as the adhesion layer. Clearly, the use of Pd yields a larger fraction of low resistance devices and generally, we find that Pd and Au when used as the adhesion layer yield better electrical contacts which may be due to their higher electronegativity[149]. For some wires with Ni/Au contacts, annealing at 330°C improved the contact to the p region while for other metal combinations, annealing did not have an appreciable effect.[2]

[2]For type A NWs annealing at 330°C for 60 s improved the contact for devices based on Ni/Au[153]. For other metal combinations, annealing did not have an appreciable effect. For type B NWs annealing under the same conditions while improving the contact to the electrons, only had an adverse effect on the contact to the hole region, for all metal combinations. This difference in the effect of annealing may reflects the difference in the dopant profiles in the two growths. The degradation of the contact to the hole region could be attributed to redistribution of the dopants at the increased temperatures, leading to a larger depletion width. Table. 6.1 shows a list of metal used to make electrical contacts.

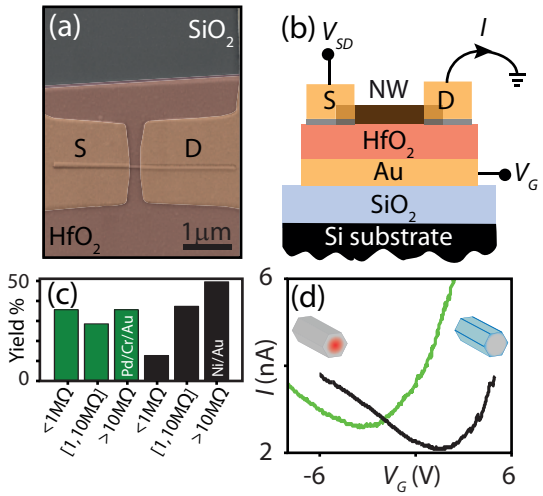

Figure 6.3.: (a) False color SEM of a NW device highlights the Gold source-drain electrodes as well as the underlying gate+oxide. (b) Cross sectional schematic of the device. (c) Summary of resistance for devices with contacts based on Pd/Cr/Au (15 devices) and Ni/Au (10 devices). (d) Typical room temperature measurement of I as a function of V_G at a bias of 10 mV for two different devices.

6.6. Discussion

The field-effect transistor configuration of the devices allows us to probe the electron and hole conduction regimes. In Fig. 6.3 d we show typical traces of current, I measured as a function of gate voltage V_G at room temperature. In contrast to intrinsic InAs NWs, the doped devices show a characteristic minimum in current as expected for ambipolar behavior[132,134]. In the p-doped NWs, the Fermi level (E_F) lies close to the top of the valence band (E_V) in the bulk while it is pinned above the conduction band minimum at the surface, ($E_{pin} = E_F - E_C^{min}$), see Fig. 6.1 e. Tuning V_G from positive to negative values depletes the electrons at the surface and populates the core with holes (Fig. 6.3 d).

In the following, transport characteristics through this electron-hole system are analyzed in detail. To study the transport mechanisms we measure the current as a function of source-drain bias, V_{SD}, gate voltage, V_G and temperature, T. Fig. 6.4 a shows the bias spectroscopy plot of I as a function of V_{SD} and V_G taken at 4.2 K for a device with Ni/Au (high resistance) contacts. The gap separating electron and hole transport is clearly reflected in the central low current region (dark) where this NW is depleted from carriers. The bias threshold for current to flow depends on V_G and forms a diamond shaped region centered around $V_G \sim 1$ V. The

slopes of the diamond edges are determined by source/drain capacitances[154] and a notable difference is due to the different spatial charge distribution in the two regimes. Fig. 6.4 b shows the evolution of gate traces with temperature (thermal spectroscopy). At $T \sim 250$ K, the NW is depleted of carriers in a region around $V_G \sim 1$ V and the depletion window widens with decreasing temperature. For each V_G there is a threshold temperature for the onset of (electron or hole) conduction and as shown further on, this energy scale matches the barrier determined from the bias spectroscopy (Fig. 6.4 a). In the ambipolar devices the carrier distribution is modulated both radially and laterally (contact region vs. free surface). We will now discuss the mechanism for charge injection into the NW when depleted, using the points I-IV marked in Fig. 6.4 a-b as reference.
Within the depletion window, E_F lies below E_C at the surface and above E_V in the bulk. However by increasing the bias (Fig. 6.4 e,f) or temperature (Fig. 6.4 c,d) electrons (holes) can gain sufficient energy (ϕ_B) to populate the conduction (valence) band. Consider the scenario at the most positive gate voltage, where holes are depleted and there are electrons at the NW surface. The metallic contacts screen the NW region underneath from the gate field and the surface accumulation layer ensures ohmic contact to the electron system. Tuning the gate to less positive values, the device conductance drops as the surface electron density is depleted. Conduction is restored at higher temperatures (I) as in Fig. 6.4 d by thermally activated population of the conduction band (barrier ϕ_B^n). Similarly, at a high enough V_{SD} (III) electrons can tunnel across the triangular Schottky-like barrier into the conduction band (Fig. 6.4 f).

As the gate voltage is decreased further, the Fermi level approaches the valence band maximum in the NW core. At a sufficiently high temperature (II), an electron can be thermally excited (ϕ_B^p) to the Fermi level and tunnel across the band gap into the contact (Fig. 6.4 c). Similarly, at a sufficiently high V_{SD} (IV) an electron from the valence band can tunnel into the contact as shown in Fig. 6.4 e. A hole, thus created in the NW core, can traverse the length of the device under source-drain bias. Hole conduction involves an additional interband tunneling and the curvature of the depletion edge at $V_G \sim 0$ V (left corner of diamond) reflects the non-linear dependence of tunneling probability on V_G. Neglecting the contribution of thermionic emission at 4K, we model the low-temperature current as tunneling across a Schottky barrier given by[155,156] $I \propto V_{SD}^2 \exp\left(-4\sqrt{2m^* e\,\phi_B^3}/3\hbar W\right)$ where the electric field, W across the barrier, ϕ_B is approximated as $\sim V_{SD}/l$, m^* is the

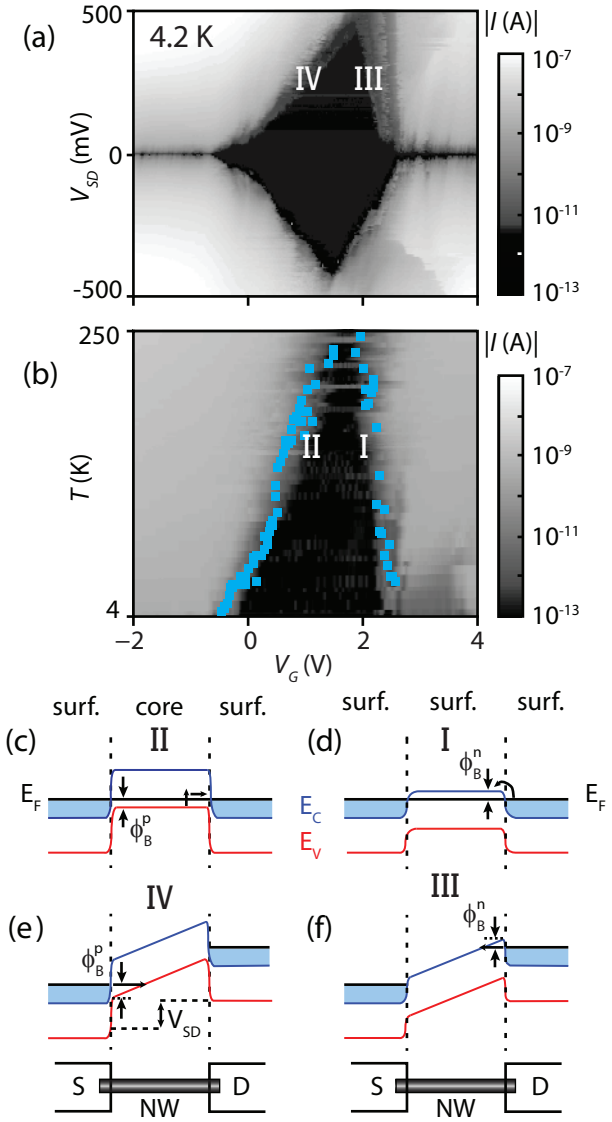

Figure 6.4.: Measurements on a device of l ∼300 nm and diameter, d_{nw} ∼65 nm. (a) I as a function of V_{SD} and V_{G} at a temperature of 4 K. (b) I as a function of T and V_{G} at a bias of 10 mV. The barrier extracted from (a) for negative bias is overlaid (blue squares) for comparison. We assume an effective mass of $0.41m_{\mathrm{e}}$ and $0.025m_{\mathrm{e}}$ for the holes and electrons, respectively and m_{e} is the electron rest mass. Band diagram at low bias along the path of a thermally excited: (c) hole (surface-core-surface) or (d) electron (surface) through the device. Similar band profiles for along the path of the charge carrier at high bias and low temperature: (e) hole, (f) electron.

effective mass, e the electron charge and l the device length. The slope of the linear region in a plot of $\log(I/V_{SD}^2)$ vs. V_{SD}^{-1} is used to estimate ϕ_B , which is converted to an effective temperature (ϕ_B/k_B) and plotted on Fig. 6.4 b (blue squares). The agreement with thermal onset confirms that the same barrier is probed by thermal and bias spectroscopy and supports our qualitative model (Fig. 6.4 c-f).

While a single gap-related barrier ϕ_B dominates transport at higher temperatures we will now address the low-temperature range where quantum effects are significant. NWs with Au/Zn/Au contacts yielded devices with lower resistance that enabled studies of the sub-Kelvin regime and measurements from one such device are presented in Fig. 6.5 a. From the transconductance we extract the electron (μ^e) and hole (μ^h) field effect mobilities using a cylinder on a conducting plane model for gate capacitance[157,158]. The data plotted in Fig. 6.5 b shows that both electron and hole mobilities increase and saturate with decreasing temperature at 80 and 25 cm^2/Vs, respectively. Due to their larger effective mass ($0.41m_e$) hole mobilities are indeed expected to be lower than that for electrons ($0.025m_e$). Regarding the electron mobilities we expect decreased μ^e for p-doped NWs due to enhanced surface scattering[159] as well as ionized impurity scattering[137] at the high doping densities. In undoped InAs NWs the low temperature μ^e is indeed found to be up to two orders of magnitude higher[160,161] than in our study. The hole mobility μ^h only changes weakly with T and while comparable to values reported to other similar NW systems[133,141], comparison with bulk systems[3] indicates that doping of the wires induces microscopic disorder despite high crystalline quality.
The low T gate traces in Fig. 6.5 a show reproducible fluctuations in G (insets) that increase in amplitude on cooling the device. These are consistent with universal conductance fluctuations (UCF) arising from quantum interference effects in a coherent diffusive conductor as has been analyzed in detail for intrinsic InAs NWs[162]. Interestingly, the UCF amplitude differs between the electron and hole regimes. The root mean squared (rms) variance of the conductance fluctuations, δG for both the electron and hole regimes are plotted as a function of T in Fig. 6.5 c. Saturation of δG around 1 K for both regimes can be understood as the phase coherence length, l_ϕ becoming comparable to device length $l \sim 1$ μm. δG for electrons levels out around $0.2e^2/h$ close to the experimentally observed value in intrinsic InAs NWs[163]. On the

[3] In a p-doped planar system with moderate doping ($\sim 10^{16} cm^{-3}$), the low temperature hole field effect mobilities have been reported to be around 800 cm^2/Vs[137,150] which was reported to decrease to 240 cm^2/Vs with increased doping levels, $10^{17} cm^{-3}$.

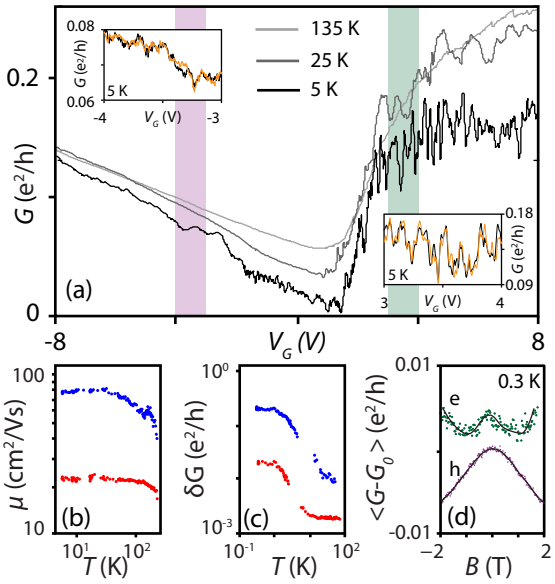

Figure 6.5.: Measurements on a device of l ∼1 μm and d_{nw} ∼55 nm. (a) Gate dependence of G at different T for V_{SD} = 1 mV. The insets demonstrate reproducibility of the conductance fluctuations (UCF) for successive gate traces at 5 K in the hole and electron regimes. (b) T dependencies for μ, electrons (blue) and holes (red), extracted from the transconductance. (c) δG as a function of T for electrons (blue) and holes (red). A moving average fit has been subtracted from the data in (a) to remove variation with V_{G}. (d) B field dependence of G at 300 mK averaged over a gate range of 1 V in the electron and hole regimes (corresponding coloured region in (a)). The curves are vertically offset for clarity. B field is applied perpendicular to the NW axis.

other hand, an order of magnitude lower saturation value for the holes ∼ 0.02 e^2/h is below what is expected even after taking into account the potential reduction (by a factor 1/2) expected for strong SO systems[164], indicating transport in this regime is influenced by a series contact resistance to the hole system.

We finally address magnetoconductance measurements obtained by applying a magnetic field B perpendicular to the NW axis. Fig. 6.5 d shows traces obtained by averaging G over a range of gate voltage much larger than the typical fluctuation period (Fig. 6.5 a). At 0.3 K an overall suppression occurs with a peak around zero field. This behavior resembles weak anti-localization (WAL) which has been observed for intrinsic InAs NWs[165] and is attributed to a quantum correction to G expected for coherent transport in a weakly disordered systems with SO interactions. The fact that the peak for the hole regime (purple trace) extends beyond 2 T shows that the SO length l_{SO} does not exceed the magnetic length $l_m = \sqrt{\hbar/eB}$ at this field[166], i.e.

l_{SO} <18 nm[167]. For comparison, the electron l_{SO} estimated from the trace minima at ∼1 T is around 25 nm, while l_{SO} ∼50-200 nm has been observed in intrinsic InAs NWs[165,168]. Our result therefore indicates that the SO interaction is stronger for the hole system in these doped InAs NW. However, further investigations would be needed to confirm this observation.

6.7. Conclusion

In conclusion, we have developed structurally clean p-type NWs as well as contacting schemes that can form the basis for further investigations of quantum transport and disorder at different doping levels. While basic signatures of disordered quantum transport are observed (UCF, WAL), more experiments are needed to test the usability of the resulting ambipolar systems for advanced devices such as few-hole quantum dots or other applications.

This work was funded by EU FP7 project SE2ND (no. 271554), the Strategic Research Council, the Danish National Advanced Technology Foundation and UNIK Synthetic Biology. The Center for Quantum Devices is supported by the Danish National Research Foundation. The authors thank K. Grove-Rasmussen, K. Flensberg, P. D. Nissen, C. Sørensen and E. Johnsen for helpful discussions.

7. Conclusions and Outlook

7.1. Overview

Using InAs nanowires as FET devices we have shown pH sensing with a sensitive as well as stable and reproducible response. The conductivity of the NW sensors can be tuned with voltage applied to either the underlying backgate or the liquid gate which lies immersed in solution. Furthermore, the change in surface potential due to surface reaction or protein binding can be estimated by measuring the shift in the gate traces. Converting the sensor signal, typically a change in current or conductance, to the change in surface potential is an effective way of normalizing response allowing for comparison across sensors on the same chip as well as other experiments. For example, during pH sensing the maximum predicted change in surface potential with pH is $-59.5\,\mathrm{mV/pH}$ at 300 K and is achieved for a high density of reactive terminal groups. The transduction of this change in surface potential into a change in current/conductance depends on the device parameters such as insulation thickness, gate as well as source-drain bias, carrier density, mobility, etc.

For signal stability, we used a liquid gate to maintain the solution at a well defined constant potential and the design of the gate electrode prevents direct interaction with the protein. While we used an open fluid exchange chamber which allows easier fluid exchange, a closed fluid chamber with a pump to draw solution through the chamber in a reproducible manner would improve the reproducibility and stability of the sensor signal. The use of pumps can have further advantages. To enable detection of low concentration (~fM-pM) of proteins, solution flow across the sensor can increase the flux of the proteins at the sensor surface thereby decreasing incubation time by orders of magnitude[169].

Progressing from pH sensing, we have shown the sensitivity of the NW sensors to the charge of proteins that bind to the surface. Using a model scheme of biotinylated-BSA as the functionalization layer and Streptavidin (or Avidin) as the protein of

interest, dependence of the sensor response on the ionic screening length (Debye length) was shown. The observation of opposite trends with the binding of oppositely charged proteins strongly suggests the sensors respond to the charge of the proteins. The magnitude of the sensor response to the incubation of 100 nM solution of Streptavidin (and Avidin) was larger than the noise and with further experiments we can determine the limit of detection.

Lastly, we have studied charge carrier transport properties through p-doped InAs NWs as a function of temperature as well as magnetic field. We probe the natural depletion layer that forms between the electrons at the surface of the NW and holes in the core. While electron and hole mobilities were low compared to planar InAs systems, holes exhibited a broad weak anti-localization peak indicating a strong spin-orbit interaction. In addition to the novel low temperature properties of the system, we believe the unique combination of surface electrons and bulk holes can be applied to chemical and biological sensing applications. With local underlying gates it may be possible to tune few of the NW devices on the sensor chip into hole conduction and the others in electron conduction. Simultaneous measurements on these NW sensors can enable mulitplexed sensing[24] where complimentary responses can be used to rule out false positives as well as test if the change in sensor signal occurs due a change in capacitive coupling or changing surface charges.

7.2. Future experiments and outlook

Sensing involves the detection of the change in potential at the sensor surface due to the charge of the binding target species. The transduction of this event into a signal will primarily depend on the capacitive coupling of the charge carriers in the sensor to the surface as well as their mobility. InAs is a high mobility semiconductor and due to the surface layer of electrons, the latter's capacitive coupling to surface event should be large. While we have demonstrated a sensing platform based on these NWs, it still remains to be established if this material offers an advantage over the more traditional Si based NWs. One of the ways to explore this idea is through signal to noise analysis.

The main sources of noise in ISFETs have been identified as low frequency flicker noise due to fluctuations in either the charge carrier mobility or charge carrier density[170]. Jakobsen et al[171] find the latter to be the dominating term arising due to

the trapping/detrapping of charge carriers at the semiconductor-insulator interface. In addition to this, electrochemical noise from the electrode-electrolyte interface contributes to the overall noise and depends on the conductance, and thus ionic concentration of the electrolyte. Increasing ionic concentration or increasing electrolyte conductance leads to a smaller noise contribution. Having already discussed the advantages of the NW geometry for sensing applications (Sec. 1.3.1), the electron density profile in the NW cross-section can be important in determining signal-to-noise ratio. If we define the signal as the effect of the charge of a target species bound at the sensor surface and noise arising primarily out of trapping-detrapping, then with the bulk of the electrons lying close the surface in InAs (Fig. 3.1) the signal can become comparable, if not larger, than the noise. This is contrary to the case of Si NWs where only in the sub-threshold regime[76] with larger screening lengths (Thomas-Fermi length) the "bulk" of the NW can respond to surface events. Thus, a signal-to-noise analysis of InAs NW sensors at different gate voltages (or electron densities) may yield an interesting insight.

A logical next step would be involve experiments following the same protocol as discussed in Sec. 5.1 with BSA-bioin and Avidin in order to compare with the binding response of Streptavidin. In addition, following the protocol of Duan et al[16] and using dilute buffers with a sufficiently large Debye length one could observe the concentration dependent binding response of the sensor.

Further direction to increase the magnitude of sensor response to protein binding can involve an alternate functionalization scheme[9,16] such as silanization followed by the addition of biotin as the recognition motif. This layer would have a smaller overall thickness, bringing the binding plane of the target protein closer to the sensor surface. The surface silanization can be probed before-hand via pH sensing where a homogenous surface modification should result in a large density of terminal $-NH_2$ groups and a linear surface potential response with changing pH.

Protein functionality can depend on the buffer strength/electrolyte concentration and in the case of limiting Debye length the response of a FET sensor can be limited by the noise. Some alternate methods to circumvent screening can be explored:

- Frequency based detection: The power spectrum of the current through a NW has been shown to depend on the concentration of protein it was exposed to[172].
- Ion step: The spike amplitude and subsequent transient response upon chang-

ing buffer solution dilution (ion step) has been used for detection of Heparin down to 50 fM and can be extended to other protein systems[92,173,174].

- Zeta potential/streaming current: While the bulk of the solution is electrically neutral, close the surface of the sensor there are mobile counter-ions in the diffuse layer. Applying a pressure and driving a solution over two sensors a fixed distance apart, the resultant ionic current can be measured and converted to the zeta potential, defined as the potential at the Stern layer. This method can be applied to protein detection after incubation even if the Debye screening shields the protein charge from the sensor[175,176].
- Liu et al[177,178] propose an oscillating electric field to overcome Debye screening. The varying electric field around the NW sensor will cause ionic transport and the ions involved are expected to not fully relax to completely screen potential. This is an interesting idea that can be tested with protein adsorption in low Debye length solutions.

In conclusion, the demonstration of a stable and reproducible InAs NW FET platform for sensing holds much promise for chemical and biological detection. New functionalization schemes and control over surface modification can allow novel sensors that can be applied to the detection as well as real time binding kinetics of biological molecules such as DNA, viruses, proteins, etc.

A. pH sensing

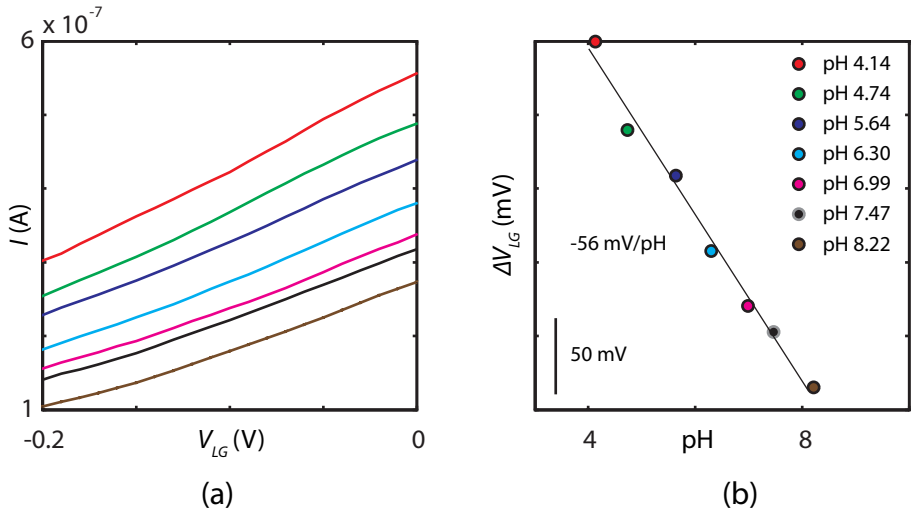

Figure A.1.: DC measurements on a single NW sensor at a 10 mV DC source drain bias. (a) The LG is swept over a small range (200 mV) and the corresponding sensor current at different pH values (colours) is shown. (b) The mean shift in liquid gate potential between the LG traces shown .

Here we present DC measurements on a single NW sensor fabricated in the same batch as the devices presented in Sec. 4.2.3. The following device was stored in a closed container in air and measured a week after fabrication. The back gate was not electrically connected to the device while a liquid gate was used to control the solution potential. A pump was used to evacuate solution from the mixing chamber and fresh solution was manually pipetted in. As before, pH buffered solutions were used.

The measurement protocol involved flushing fresh solution into the mixing chamber and following repeated solution exchanges and signal stabilisation, the liquid gate voltage was swept over a small range (200 mV). Fig. A.1 a shows data from a single

sensor on the chip. Different colours indicate solutions of different pH. The mean shift of the gate trace is shown in Fig. A.1 b. We see the device sensitivity ($\frac{d\Delta V_{LG}}{dpH}$) is high ~ 56 mV/pH and linear over the range of pH presented. This compares well with the devices presented in Sec. 4.2.3.

B. BSA - Gold Streptavidin

In this section, the sensor chips discussed in Sec. 5.1 and Sec. 5.2 are cleaned[1] and reused to demonstrate the binding of a negatively charged gold colloid particle (Au-Strep.)[179] conjugated with Streptavidin[180] to a surface functionalized with biotinylated BSA. The cyclic DC measurements were performed on the same NWs sensors as in Sec. 5.1. In this scheme, the surface is first functionalized with biotinylated BSA functionalization followed by the addition of a 100 nM colloidal suspension gold-Streptavidin as the species of interest. We use three dilutions of a 2 mM sodium phosphate buffer - undiluted, 10X and 100X with corresponding Debye lengths of 5, 16 and 51 nm respectively. All solutions had a pH of 7.4. The gold colloidal particles have an average diameter of 20 nm.

We start by establishing a stable baseline for all three dilutions by repeated solution exchange as shown in Fig. B.2 a. The three rows of figures correspond to the same sensors shown in Fig. 5.3 a. A step like response in current is seen with increasing dilution. Surface contamination/degradation may account for lower conductivities of the sensors. Biotinylated BSA is introduced in the mixing chamber and after ~1500 s of incubation, the three buffer dilutions are flushed sequentially, establishing a stable baselines. This is followed by the addition of Au-Streptavidin. After ~1000 s the buffer baselines are again established.

Fig. B.3 a shows a magnified portion of the sensor responses from Fig. B.2 a, to the incubation of biotinylated BSA. The sensor current is converted to an equivalent liquid gate potential with offset at the introduction of the protein subtracted. The surface potential drops by 18 mV after 1500 s however the kinetics involved appear to be different with the response still not saturated at ~1500 s. It is not clear what

[1]The sensor chip was rinsed with MQ water followed by a 30 min soak in a 2% solution of Helmenex in MQ water and finally rinsed with MQ water for 30 mins using a pump to flush the mixing chamber continuously. Ideally, the sensor chip should be cleaned in an oxygen plasma oven, however plugging/unplugging the sensor chip comes with the risk of electrostatic discharge which can literally blow up the NWs.

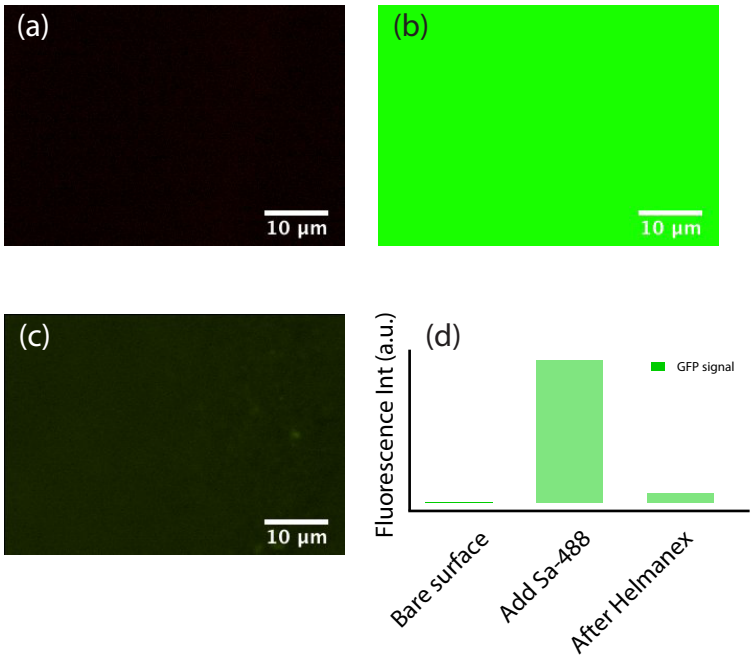

Figure B.1.: Fluorescence signal from a (a) bare Si chip, (b) after BSA-biotin and Avidin incubation and (c) after the rinse in a 2% Helmanex solution. (d) The average signal intensity from the three images.

is the nature of the sensor surface after the Helmenex wash and if the bound BSA is washed away entirely or partly washed away and partly unfolded. λ_D in the protein solution should be similar to that in the undiluted buffer, around 5 nm. A binding curve is observed during the incubation of Au-Streptavidin, with a fall of ~3 mV in surface potential after 500 s. Compared to the addition of Streptavidin, discussed in the previous section, a larger λ_D as well as a larger charge (gold colloid) may contribute to a slightly larger signal response. The latter is still small compared to the BSA signal due to the fact that is binds a finite distance from sensor surface. The magnitude of the sensor response for increasing dilutions (Debye lengths) is discussed later in this section.

The stable baselines for the three solutions (varying shades of grey) are shown in Fig. B.2 b. The change in sensor current, ΔI due to BSA binding (red circles) as well as Au-Streptavidin binding (blue squares) is presented in Fig. B.2 c. Though the magnitude of response is different across the sensors, a similar trend is observed. Qualitatively, ΔI becomes larger with increasing dilution. To compare the responses ΔI is converted to an equivalent change in liquid gate potential ($\Delta\psi_0$), as before

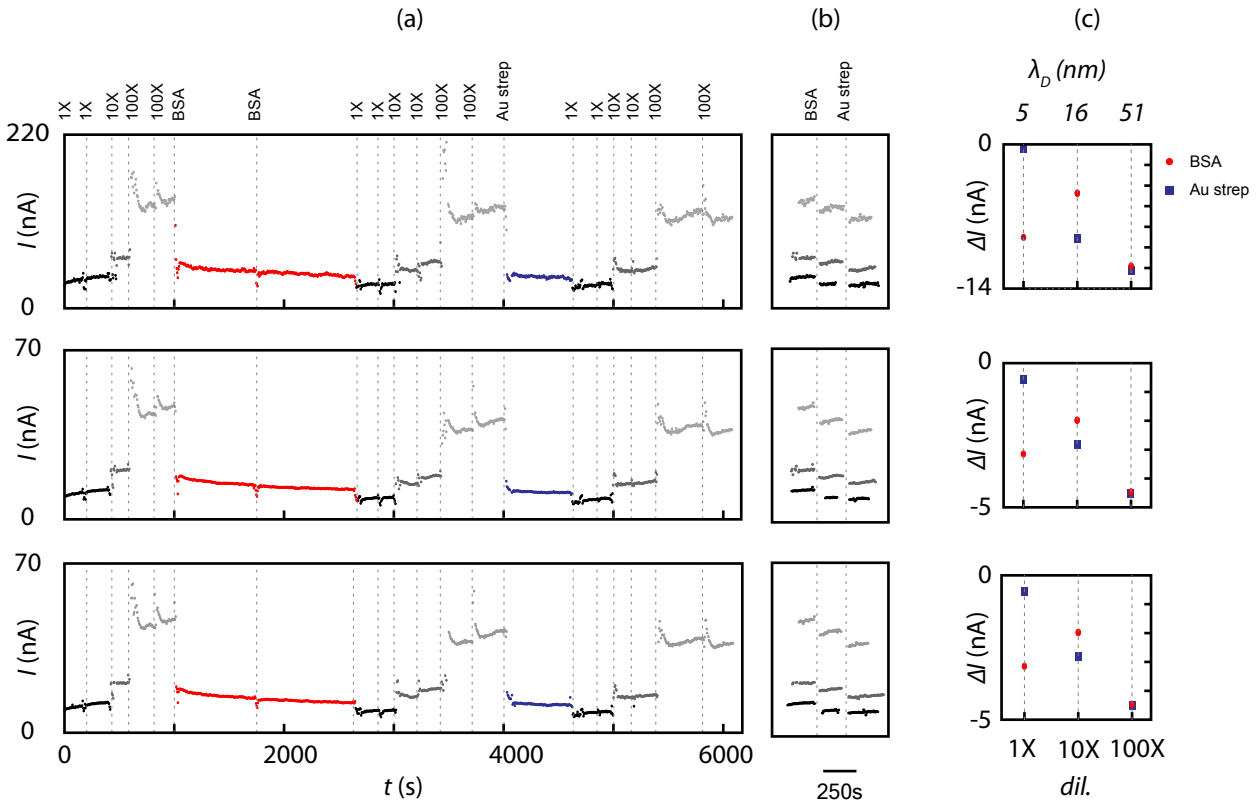

Figure B.2.: (a) DC response of three NWFET sensors to the incubation of BSA (red trace) and Au-Streptavidin (blue trace) as well as the sequential flushing of buffer solutions of varying ionic concentration (different shades of grey). Vertical grid lines and the label above mark the introduction of a solution into the mixing chamber. (b) The Stable baselines corresponding to the different buffer dilutions are extracted. (c) The change in the current baseline (ΔI) with the addition of BSA (Au-Strep.) for the three buffer dilutions(1X, 10X and 100X). The corresponding λ_D is also indicated on the x-axis.

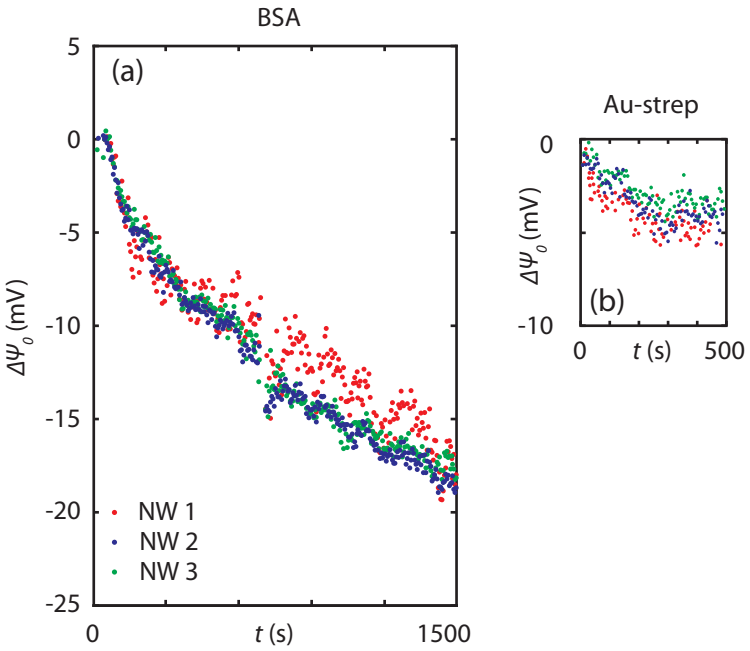

Figure B.3.: A magnified portion of the sensor response to the incubation of BSA and Au-Strep. from Fig. B.2 a. Both proteins solutions were made in the 1X buffer and the sensor response (I) is converted to liquid gate potential with the offset at the introduction of protein subtracted.

and presented in Fig. B.4.

The response to the addition of BSA (red circles) is discussed first. For the undiluted buffer (1X), a potential drop of ~12 mV is observed which is lower than the drop (~18 mV) observed in the binding curve in Fig. B.3 a. As discussed in the previous section, this may arise out of the washing away of unbound proteins and multiple layers. At higher λ_D (10X, 100X) a smaller overall drop in potential ($\Delta\psi_0$) is observed, ~4 mV, which does not change much with an increase of λ_D from 16 to 51 nm. Since the condition of the surface, with possible leftover contaminants following the Helmanex cleaning, is unknown it is difficult to know the stability of the BSA binding. The buffers are sequentially flushed from 1X to 100X and the solution exchanges may result in unbinding and washing away of the added BSA, leading to a lower surface potential at the higher dilutions.

The change in the surface potential in response to the incubation of Au-Streptavidin is presented in Fig. B.3 b. It should be noted that the Streptavidin here serves as

a linker to the biotin and it is the charge on the Au colloidal particle that will lead to a significant $\Delta\psi_0$. For the undiluted buffer (1X), there is no change in the surface potential within the limit of reproducibility of the sensors. At the next higher dilution, 10X a drop of ~8-10 mV in surface potential is observed. In comparison, $\Delta\psi_0$ does not change for $\lambda_D \sim 51$ nm. $\lambda_D \sim 16$ nm is already comparable to the expected size of the target protein+BSA system and increasing λ_D should not affect the surface potential. While Steptavidin is known for its low non-specific binding we do not have a sensing experiment without biotinylated BSA functionalization as a control to gauge the sensor response to the same. We observe a clear binding curve during the addition of BSA and a weak one for Au-Streptavidin.

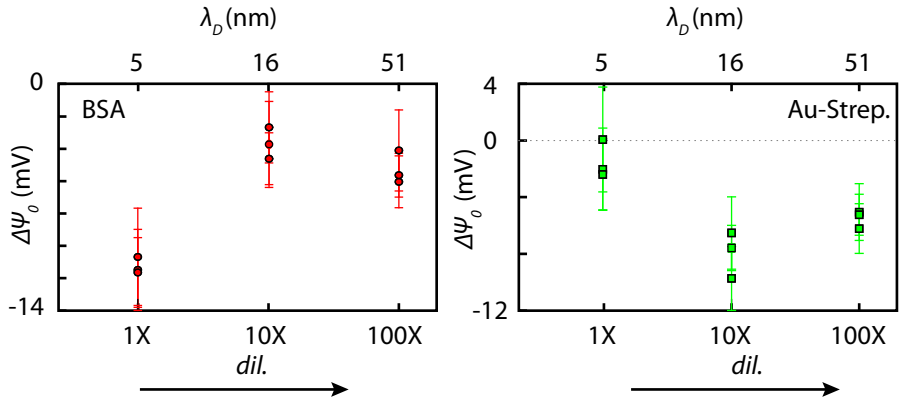

Figure B.4.: The change in the sensor current (ΔI) is converted to a change in the equivalent liquid gate potential (or surface potential ($\Delta\psi_0$)) via the corresponding liquid gate traces (not shown) for (a) BSA and (b) Streptavidin incubation. Arrows indicate the order in which the different buffer dilutions were flushed.

In conclusion, the sensor was functionalized with negatively charged BSA-biotin. A binding curve during the incubation of the same is seen as well as an overall decrease in the sensor baseline at different dilutions. The addition of negatively charged Au-streptavidin results in a smaller signal response, with a visible binding curve. The sensor baselines also show a concurrent decrease after incubation consistent with the binding of a negatively charged protein.

C. Automatic image analysis and CAD positioning using MATLAB

A NW sensor consists of an individual NW with two electrical source drain contacts. As discussed in Sec. 3.3.2, this involves depositing NWs on a substrate and taking images using an optical microscope. These images need to be rotated, scaled and aligned in a CAD file which is turn is used in the subsequent ebeam lithography. 6-10 images for every sensor chip design is typical and following MATLAB scripts allow for this procedure to be automated, making it easier to fabricate multiple sensor chips in parallel. Fig. C.1 shows the basic scheme of the script. The MATLAB code for the same is shown.

The following is the main script:

Listing C.1: new_cross_search.m

```
%  Open console and load files
[filenames, pathname] = uigetfile({'*.jpg'},'Open File','Multiselect','on','D:\
    Designs\'); % choose file to open
 addpath(pathname);
 write=1;

%% ....Multiple filenames put in cells, where as single file selection is
% not a cell
filetype=whos('filenames');
if strcmp(filetype.class,'cell')~=1
    filenames={filenames};
end

iter=length(filenames);
%% ------------------------------------------------------
cross=imread('D:\Designs\Cross\cross_new_microscope.jpg');
% [dr,dc,~]=size(cross);

for count=1:iter
    filenaam=filenames{count};
    tic

%% This cell uses strels, and takes a sec. longer. Usually off by 0.01 deg.
```

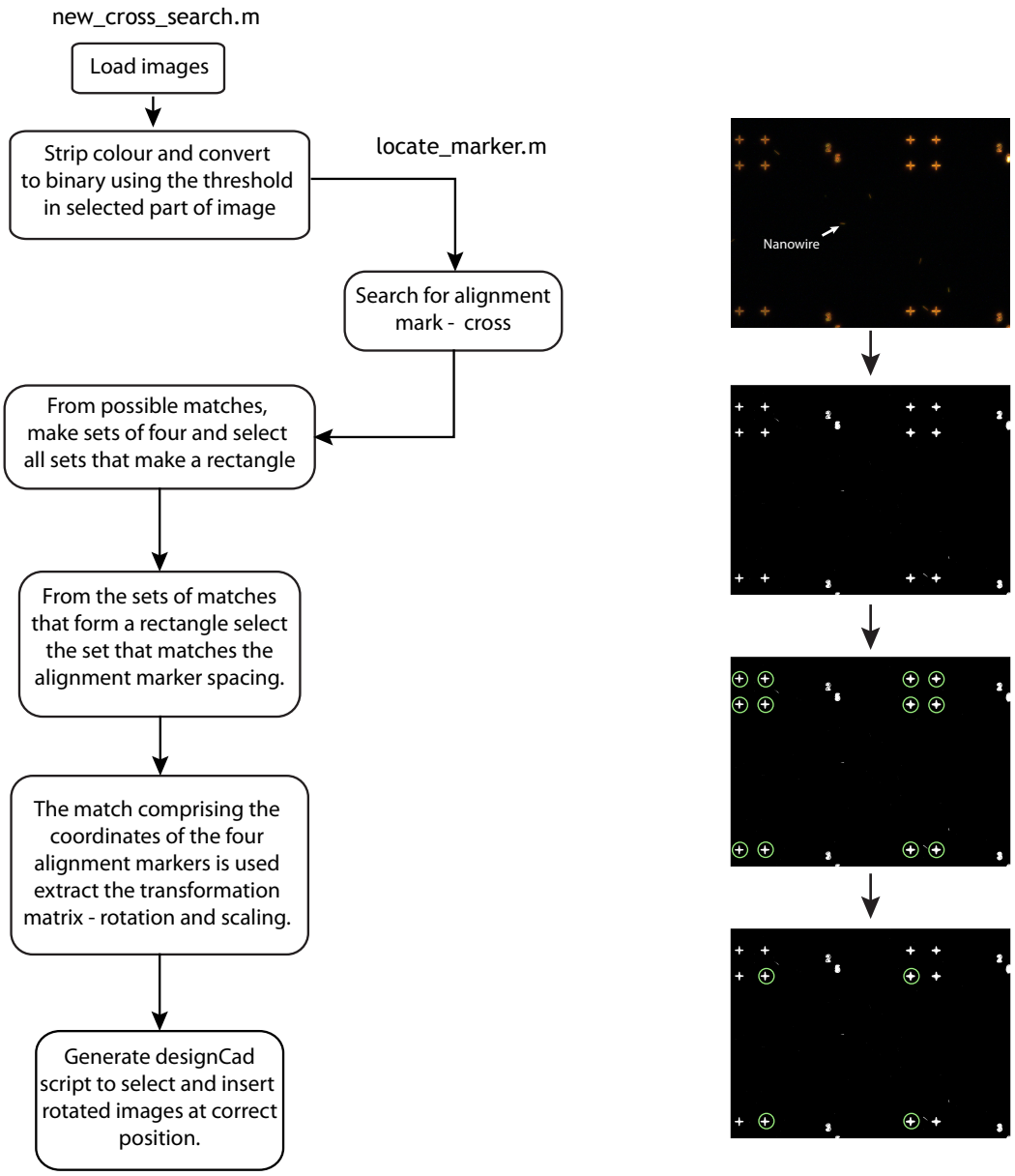

Figure C.1.: Flow chart presenting the scheme for analysing an image to determine rotation and scaling. Images beside the text boxes provide an illustration of the content.

```
    level_factor=0.8;
    image_proc=locate_marker(filenaam,pathname,level_factor,1000);
    centroid_matrix=image_proc{1};
    area_matrix=image_proc{4}; %area of the cross found. This will be used as a
        weight to extract scaling, rotation, etc...
    markercount=size(centroid_matrix);
    prmu=combnk(1:markercount,4);%all possible sets of 4, which will be tested if
        they form a rectangle.
    rec_array=zeros(length(prmu),1);
   %%
   for k=1:size(prmu)
       rec_array(k)=rect_finder(centroid_matrix(prmu(k,:),:));
   end

   figure('Position',[100 100 900 400],'nextplot','add')
   subplot(1,3,1);imshow(filenaam,'initialmagnification',33);
   hold on
   found=find(rec_array);
   for l=1:length(found)
       rects{l}=centroid_matrix(prmu(found(l),:),:);
       areas{l}=area_matrix(prmu(found(l),:),:);
   end

   area_array=rectarea(rects);

 %% ---- find the set of crosses which match the required area

   [~,p]=min(abs(area_array - ones(length(area_array),1)*3.7e6));%1.77e6
   k=p;
   subplot(1,3,1);plot(rects{k}(:,1),rects{k}(:,2),'o')
   y=order_rect(rects{k});% index k is the largest rect found.
   weights=areas{k};
   y1=extract_angle(y.sortset,weights(y.index));%insert weights here
   if abs(y1.matrix(1))>0.3
       y1.angles=y1.angles(logical([0 1;1 0]));
   else
       y1.angles=y1.angles(logical([1 0;0 1]));
   end
%% ----This is a crude way of checking if correction angle is +0.1 or -0.1.
% If it's -0.1 the program spits ou 89.9.
   if mean(real(y1.angles))>5
       y1.angles=y1.angles-90;
       y1.unmodangles=90 - y1.unmodangles;
   end
%% ------------------------------------------------------------------------
   toc

   sortthis=rects{p};
   [~,ix]=sort(sortthis(:,2));
   sortagain=sortthis(ix(3:4),:);
   simpleangle=sortagain(1,:)-sortagain(2,:);
   simpleangle=atand(simpleangle(2)/simpleangle(1));
   [~,ix]=sort(sortagain(:,1));
```

```
    crnr=sortagain(ix(1),:);
    subplot(1,3,1);plot(crnr(1),crnr(2),'ro');
    hold off
    fprintf('weighted␣angles:␣[%2.2f␣%2.2f]\nLSQ:␣[%2.2f␣%2.2f;%2.2f␣%2.2f]\nsimple
        ␣angle:␣%2.3f\n',y1.angles,y1.unmodangles,simpleangle)


    %Now rotate the image and save it


%% Modify x_r_c and y_r_c with rotation
isize=size(imread(filenaam));
% orgn=[2559/2 1919/2];
orgn=[isize(2)/2 isize(1)/2];
bl = crnr;
vector_i=bl- 1 - orgn;
theta=-mean(y1.angles);
im_r=imrotate(image_proc{2},-theta,'bilinear','crop');
R_theta=[cosd(theta) -sind(theta); sind(theta) cosd(theta)];
vector_f=R_theta*(vector_i)';
bl=vector_f'+1+orgn;
s=sprintf('%2.2f,%2.2f',bl(1),bl(2));
% figure(3*i);
subplot(1,3,3);imshow(im_r,'InitialMagnification',33);
title('rotated␣image␣with␣ref␣cross␣shown');
hold on
plot(bl(1),bl(2),'yo')
hold off

s=strcat('@',s,'_rot.jpg');
modfilename1=strrep(filenaam,'.jpg',s);
modfilename=strcat(pathname,modfilename1);

if write==1
    imwrite(im_r,modfilename,'jpg');
end
make_macro_biofetlong(modfilename1,pathname,'trial',orgn,count,count==iter);
end

%%
% Close all button
hb4 = uicontrol('Style','pushbutton',...
           'String','Close␣all␣figures','Position', [100 10 100 50],...
           'Callback','uiresume;close␣all');
uiwait
```

The script Listing C.1 calls this function to locate alignment markers:

Listing C.2: locate_marker.m

```
function out=locate_marker(fn,pathname,level_factor,cleanupdisksize)

% Is the input a direct image or image location
if isempty(pathname)
    I_original=fn;
else
    fn=strcat(pathname,'\',fn);
    I_original=imread(fn);
end

% Depending if the image is B&W or colour...
[d1,d2,d3]=size(I_original);
if d3==3
%     I_bw=rgb2gray(I_original);
      I_bw=I_original(:,:,1);
else
    I_bw=I_original;
end
% ------------------------------------------

% Define strel = a cross with dimensions in
% pixels: length and width of a bar-----
h=162;
t=18;
h2=round(h/2);
a=zeros(h,h);
a(:,round(h2 -t/2):round(h2+t/2))=1;
a(round(h2 -t/2):round(h2+t/2),:)=1;
% ------------------------------------------------

% Maximize contrast and convert to binary-----
level = graythresh(I_bw);
bw = im2bw(I_bw,level_factor*0.8*level);
bw = bwareaopen(bw, cleanupdisksize);
bw = imfill(bw,'holes');

% ------------------------------------------------
%Search for the cross and display it--------
se_H=strel(a);
cross_found=imopen(bw,se_H);

bw=cross_found;
[B,L] = bwboundaries(bw,'noholes');
stats = regionprops(L,'Area','Centroid');
centroid_matrix=[];

for k = 1:length(B)
  centroid = stats(k).Centroid;
  centroid_matrix=[centroid_matrix;centroid];
```

```
end
%output is the centers of all posibble matches, the original image and binary image
     with locates crosses.
out={centroid_matrix,I_original,bw};
```

D. Generations of biofet devices

Table D.1.: The following is a list of various iterations of the sensor setup and design

Features	Issues	Solution	Drawback
HF etch prior to metallization	Ohmic electrical contact to the NW	Longer evacuation time in the metallization chamber before metal evaporation	Unpredictable quality of electrical contact with large device-to-device variation
ALD oxide	ALD oxide patterning and lift off issues	Oxide deposition temp. reduced to $90 - 115\,^{\circ}\mathrm{C}$, followed by lift off in hot PG removed ($80\,^{\circ}\mathrm{C}$)	-
Fluidic chamber: Pipette tip glued to surface with Silicone glue	Overnight curing step. Chamber not always water tight.	-	-

Signal stability	Sensor signal drift over time as well as spikes/transients observed with solution flushes. We suspected instabilities in the pH of the solution.	Switch to pH buffered solutions	-
Gold wire immersed in solution used as liquid gate	The signal stability was affected and a pronounced drift was observed. This may have resulted out of instability of the electrode.	Solution potential was left floating and the back gate was used to control NW conductivity instead.	-
E-beam lithography for customizable designs.	Exposure time longer than UV lithography	-	-
$(NH_4)_2S_x$ etching and passivating technique for reproducible low resistance electrical contact to the NW	Can lead to resist delamination in case of weak adhesion to substrate.	-	-

[Protein incubation]	Small response to protein incubation, comparable to drift	Thinner ALD oxide isolation - 5-10 nm	Leakage current from NW into solution.
Non active regions of the sensor are isolated with SU8, a negative resist patterned via EBL	Low exposure dose lead to frequent over-exposure	-	-
Isolation with PMMA, as above and this is followed by ALD oxide	PMMA isolation developed cracks. Leakage current was observed.	-	-
Protein aggregation	Tests performed by R. Frederiksen found that in the presence of Silicone glue, the BSA functional layer would aggregate.	New fluidic chamber design with O-rings	-
Modified fluid chamber which is mechanical clamped and O-rings make a water tight seal	Excess mechanical pressure on the O-ring can grind away the ALD oxide isolation	-	-

Pump is used to draw solution out of the chamber.	Tight connections to avoid bubbles.		
ALD Al_2O_3 was tried instead of HfO_2 due the unavailability of precursor material.	Al_2O_3 is harder to pattern and lift off.		
Common source-drain bias for several NWs	Common source-drain bias line allows cyclic measurement	Slower measurement on a single NW.	-
A sealed Ag/AgCl electrode is used a liquid gate.	The ceramic frit at the end of the sealed tube needs to be cleaned before every experiment.	-	-
In-situ Ar ion etch prior to metallization leads to reproducible electrical contacts, eliminating wet etch issues.	-	-	-

List of Publications

1. *Indium Arsenide nanowire field-effect transistors for pH and biological sensing,* **S. Upadhyay**, R. Frederiksen, N. Lloret, L. de Vico, J. Jensen, K. Martinez, J. Nygård - in preparation

    - The experiments were carried out together with R. Frederiksen. I fabricated the devices and RF & N. Lloret were responsible for surface functionalization, buffer and protein solutions. Data analysis was performed together with RF and Luca De Vico.

2. *Low temperature transport in p-doped InAs nanowires*, **S. Upadhyay**, T. Sand-Jespersen, M. H. Madsen, P. Krogstrup, and J. Nygård. Appl. Phys. Lett. 103, 162104 (2013)

    - The experiments were carried out together with T. Sand-Jespersen. I fabricated the devices. Data analysis was peformed together with TSJ and J. Nygård.

3. *Effects of buffer composition and dilution on nanowire field-effect biosensors*, N. Lloret, R.S. Frederiksen, T.C. Møller, N.I. Rieben, **S. Upadhyay**, L. De Vico, J.H. Jensen, J. Nygård, K.L. Martinez. Nanotechnology, 24(3), 035501 (2013).

    - I was involved in the data analysis as well as a section in the article.

4. *Comparison of gate geometries for tunable, local barriers in InAs nanowires*- P.D. Nissen, T. Sand-Jespersen, K. Grove-Rasmussen, A. Márton, **S. Upadhyay**, M. H. Madsen, S. Csonka, and J. Nygård. J. Appl. Phys. 112, 084323 (2012)

    - I guided A. Marton in the fabrication of and measurements on one of the two device geometries discussed in the article.

5. *Doping incorporation paths in catalyst-free Be-doped GaAs nanowires*, A. Casadei, P. Krogstrup, M. Heiss, J. A. Röhr, C. Colombo, T. Ruelle, **S. Upadhyay**, C. B. Sørensen, J. Nygård, and A. Fontcuberta i Morral. Appl. Phys. Lett. 102, 013117 (2013)

    - I was involved in the data analysis along with J.A. Röhr and P. Krogstrup, as well as a section in the article along with PK.

Bibliography

[1] Turner, A. P. F. *Science* **2000**, *290*, 1315–1317.

[2] Lu, W.; Xie, P.; Lieber, C. M. *IEEE Transactions on Electron Devices* **2008**, *55*, 2859–2876.

[3] Duan, X.; Huang, Y.; Cui, Y.; Wang, J.; Lieber, C. M. *Nature* **2001**, *409*, 66–9.

[4] Yan, R.; Gargas, D.; Yang, P. *Nature Photonics* **2009**, *3*, 569–576.

[5] Zimmler, M. a.; Capasso, F.; Müller, S.; Ronning, C. *Semiconductor Science and Technology* **2010**, *25*, 024001.

[6] Kelzenberg, M. D.; Turner-Evans, D. B.; Kayes, B. M.; Filler, M. a.; Putnam, M. C.; Lewis, N. S.; Atwater, H. a. *Nano letters* **2008**, *8*, 710–4.

[7] Wright, J. S.; Lim, W.; Norton, D. P.; Pearton, S. J.; Ren, F.; Johnson, J. L.; Ural, A. *Semiconductor Science and Technology* **2010**, *25*, 024002.

[8] Cui, Y.; Wei, Q.; Park, H.; Lieber, C. M. *Science* **2001**, *293*, 1289–92.

[9] Stern, E.; Klemic, J. F.; Routenberg, D. A.; Wyrembak, P. N.; Turner-evans, D. B.; Hamilton, A. D.; Lavan, D. A.; Fahmy, T. M.; Reed, M. A. *Nature* **2007**, *445*, 519–522.

[10] Nadj-Perge, S.; Frolov, S. M.; Bakkers, E. P. A. M.; Kouwenhoven, L. P. *Nature* **2010**, *468*, 1084–1087.

[11] Pribiag, V. S.; Nadj-Perge, S.; Frolov, S. M.; van den Berg, J. W. G.; van Weperen, I.; Plissard, S. R.; Bakkers, E. P. A. M.; Kouwenhoven, L. P. *Nature nanotechnology* **2013**, *8*, 170–4.

[12] Mourik, V.; Zuo, K.; Frolov, S. M.; Plissard, S. R.; Bakkers, E. P. A. M.; Kouwenhoven, L. P. *Science* **2012**, *336*, 1003 – 1007.

[13] Das, A.; Ronen, Y.; Most, Y.; Oreg, Y.; Heiblum, M.; Shtrikman, H. *Nat. Phys.* **2012**, *8*, 887–895.

[14] Krogstrup, P.; Jørgensen, H. I.; Heiss, M.; Demichel, O.; Holm, J. V.; Aagesen, M.; Nygard, J.; Fontcuberta i Morral, A. *Nature Photonics* **2013**, *7*, 306–310.

[15] Bergveld, P. *IEEE Transactions on Biomedical Engineering* **1970**, *BME-17*, 70–71.

[16] Duan, X.; Li, Y.; Rajan, N. K.; Routenberg, D. A.; Modis, Y.; Reed, M. A. *Nature nanotechnology* **2012**, *7*, 401–7.

[17] Schöning, M. J.; Poghossian, A. *The Analyst* **2002**, *127*, 1137–1151.

[18] Patolsky, F.; Zheng, G.; Hayden, O.; Lakadamyali, M.; Zhuang, X.; Lieber, C. M. *PNAS* **2004**, *101*, 14017–14022.

[19] Clément, N.; Nishiguchi, K.; Fujiwara, A.; Vuillaume, D. *Nature Communications* **2010**, *1*, 92.

[20] Männik, J.; Heller, I.; Janssens, A. M.; Lemay, S. G.; Dekker, C. *Nano letters* **2008**, *8*, 685–8.

[21] Berthing, T.; Bonde, S.; Sørensen, C. B.; Utko, P.; Nygård, J.; Martinez, K. L. *Small* **2011**, *7*, 640–7.

[22] Duan, X.; Gao, R.; Xie, P.; Cohen-Karni, T.; Qing, Q.; Choe, H. S.; Tian, B.; Jiang, X.; Lieber, C. M. *Nature Nanotechnology* **2012**, *7*, 174–9.

[23] Nair, P. R.; Alam, M. A. *Appl. Phys. Lett* **2006**, *88*, 233021–233023.

[24] Zheng, G.; Patolsky, F.; Cui, Y.; Wang, W.; Lieber, C. *Nature Biotechnology* **2005**, *23*, 1294–1301.

[25] Choi, Y.; Olsen, T. J.; Sims, P. C.; Moody, I. S.; Corso, B. L.; Dang, M. N.; Weiss, G. a.; Collins, P. G. *Nano letters* **2013**, *13*, 625–31.

[26] Stern, E.; Wagner, R.; Sigworth, F. J.; Breaker, R.; Fahmy, T. M.; Reed, M. A. *Nano letters* **2007**, *7*, 3405–9.

[27] Cui, Y.; Lauhon, L.; Gudiksen, M. *Applied Physics Letters* **2001**, *78*, 2214–2216.

[28] Hahm, J.; Lieber, C. *Nano Lett.* **2004**, *4*, 51–54.

[29] Gao, Z.; Agarwal, A.; Trigg, A. D.; Singh, N.; Fang, C.; Tung, C.-H.; Fan, Y.; Buddharaju, K. D.; Kong, J. *Analytical chemistry* **2007**, *79*, 3291–7.

[30] Wang, W.; Chen, C.; Lin, K.-h.; Fang, Y.; Lieber, C. M. *PNAS* **2005**, *102*, 3208–3212.

[31] Chang, K.; Chen, C.; Sheu, J.; Li, Y. *Sensors and actuators. B: Chemical* **2009**, *138*, 148–153.

[32] McAlpine, M. C.; Friedman, R. S.; Jin, S.; Lin, K.-h.; Wang, W. U.; Lieber, C. M. *Nano Letters* **2003**, *3*, 1531–1535.

[33] Timko, B. P.; Cohen-Karni, T.; Yu, G.; Qing, Q.; Tian, B.; Lieber, C. M. *Nano letters* **2009**, *9*, 914–8.

[34] Tian, R.; Regonda, S.; Gao, J.; Liu, Y.; Hu, W. *Lab on a chip* **2011**, *11*, 1952–61.

[35] Stern, E.; Steenblock, E. R.; Reed, M. A.; Fahmy, T. M. *Nano Letters* **2008**, *8*, 3310–4.

[36] Stern, E.; Vacic, A.; Li, C.; Ishikawa, F. N.; Zhou, C.; Reed, M. a.; Fahmy, T. M. *Small* **2010**, *6*, 232–8.

[37] Fan, Z.; Wang, D.; Chang, P.-C.; Tseng, W.-Y.; Lu, J. G. *Applied Physics Letters* **2004**, *85*, 5923.

[38] Li, C.; Curreli, M.; Lin, H.; Lei, B.; Ishikawa, F. N.; Datar, R.; Cote, R. J.; Thompson, M. E.; Zhou, C. *J. Am. Chem. Soc.* **2005**, *127*, 12484–12485.

[39] Rouhanizadeh, M.; Tang, T.; Li, C.; Hwang, J.; Zhou, C.; Hsiai, T. K. *Sensors and Actuators B: Chemical* **2006**, *114*, 788–798.

[40] Cheng, Y.; Xiong, P.; Yun, C. S.; Strouse, G. F.; Zheng, J. P.; Yang, R. S.; Wang, Z. L. *Nano Letters* **2008**, *8*, 4179–4184.

[41] Ishikawa, F. F. N.; Chang, H. H.-K.; Curreli, M.; Liao, H.-I. H.; Olson, C. A.; Chen, P.-C.; Zhang, R.; Roberts, R. W.; Sun, R.; Cote, R. J.; Thompson, M. E.; Zhou, C. *ACS Nano* **2009**, *3*, 1219–24.

[42] Yeh, P.-H.; Li, Z.; Wang, Z. L. *Advanced Materials* **2009**, *21*, 4975–4975.

[43] Besteman, K.; Lee, J.-O.; Wiertz, F. G. M.; Heering, H. A.; Dekker, C. *Nano Letters* **2003**, *3*, 727–730.

[44] Heller, I.; Janssens, A. M.; Männik, J.; Minot, E. D.; Lemay, S. G.; Dekker, C. *Nano Letters* **2008**, *8*, 591–5.

[45] Chen, R. J.; Bangsaruntip, S.; Drouvalakis, K. a.; Kam, N. W. S.; Shim, M.; Li, Y.; Kim, W.; Utz, P. J.; Dai, H. *PNAS* **2003**, *100*, 4984–9.

[46] Okuno, J.; Maehashi, K.; Kerman, K.; Takamura, Y.; Matsumoto, K.; Tamiya, E. *Biosensors & bioelectronics* **2007**, *22*, 2377–2381.

[47] Ishikawa, F. N.; Stauffer, B.; Caron, D. a.; Zhou, C. *Biosensors & bioelectronics* **2009**, *24*, 2967–72.

[48] Subramanian, S.; Aschenbach, K. H.; Evangelista, J. P.; Najjar, M. B.; Song, W.; Gomez, R. D. *Biosensors & bioelectronics* **2011**, *32*, 1–7.

[49] Kurkina, T.; Vlandas, A.; Ahmad, A.; Kern, K.; Balasubramanian, K. *Angewandte Chemie International Edition* **2011**, *50*, 3710–3714.

[50] Drouvalakis, K. a.; Bangsaruntip, S.; Hueber, W.; Kozar, L. G.; Utz, P. J.; Dai, H. *Biosensors & bioelectronics* **2008**, *23*, 1413–21.

[51] Cohen-Karni, T.; Qing, Q.; Li, Q.; Fang, Y.; Lieber, C. M. *Nano letters* **2010**, *10*, 1098–102.

[52] Lei, N.; Li, P.; Xue, W.; Xu, J. *Measurement Science and Technology* **2011**, *22*, 107002.

[53] Stine, R.; Mulvaney, S. P.; Robinson, J. T.; Tamanaha, C. R.; Sheehan, P. E. *Analytical chemistry* **2013**, *85*, 509–21.

[54] Tolani, S. B.; Craig, M.; DeLong, R. K.; Ghosh, K.; Wanekaya, A. K. *Analytical and bioanalytical chemistry* **2009**, *393*, 1225–31.

[55] Aravinda, C. L.; Cosnier, S.; Chen, W.; Myung, N. V.; Mulchandani, A. *Biosensors & bioelectronics* **2009**, *24*, 1451–5.

[56] García-Aljaro, C.; Bangar, M. A.; Baldrich, E.; Muñoz, F. J.; Mulchandani, A. *Biosensors & bioelectronics* **2010**, *25*, 2309–12.

[57] Dayeh, S. a.; Yu, E. T.; Wang, D. *Small* **2009**, *5*, 77–81.

[58] Dayeh, S. *Semiconductor Science and Technology* **2010**, *024004*.

[59] Kawaji, S.; Gatos, H. *Surface Science* **1967**, *7*, 215–228.

[60] Wirths, S.; Weis, K.; Winden, A.; Sladek, K.; Volk, C.; Alagha, S.; Weirich, T. E.; von der ahe, M.; Hardtdegen, H.; Lueth, H.; Demarina, N.; Gruetzmacher, D.; Schaepers, T. *J. Appl. Phys.* **2011**, *110*, 053709.

[61] Du, J.; Liang, D.; Tang, H.; Gao, X. P. A. *Nano Lett.* **2009**, *9*, 4348 – 4351.

[62] Patolsky, F.; Zheng, G.; Lieber, C. M. *Nanomedicine* **2006**, *1*, 51–65.

[63] Wanekaya, A. K.; Chen, W.; Myung, N. V.; Mulchandani, A. *Electroanalysis* **2006**, *18*, 533–550.

[64] Ramgir, N. S.; Yang, Y.; Zacharias, M. *Small (Weinheim an der Bergstrasse, Germany)* **2010**, *6*, 1705–22.

[65] Penner, R. M. *Annual review of analytical chemistry (Palo Alto, Calif.)* **2012**, *5*, 461–85.

[66] Cohen-Karni, T.; Lieber, C. M. *Pure and Applied Chemistry* **2013**, *85*, 883–901.

[67] Lee, M.-H.; Lee, K.-N.; Jung, S.-W.; Kim, W.-H.; Shin, K.-S.; Seong, W.-K. *International journal of nanomedicine* **2008**, *3*, 117–24.

[68] Tarasov, A.; Wipf, M.; Bedner, K.; Kurz, J.; Fu, W.; Guzenko, V. A.; Knopfmacher, O.; Stoop, R. L.; Calame, M.; Schönenberger, C. *Langmuir* **2012**, *28*, 9899–9905.

[69] Tarasov, A.; Wipf, M.; Stoop, R.; Bedner, K. *ACS NANO* **2012**, 9291–9298.

[70] Wipf, M.; Stoop, R. L.; Tarasov, A.; Bedner, K.; Fu, W.; Wright, I. A.; Martin, C. J.; Constable, E. C.; Calame, M.; Schönenberger, C. *ACS Nano* **2013**, 130614171719008.

[71] Hsiao, C.-Y.; Lin, C.-H.; Hung, C.-H.; Su, C.-J.; Lo, Y.-R.; Lee, C.-C.; Lin, H.-C.; Ko, F.-H.; Huang, T.-Y.; Yang, Y.-S. *Biosensors & bioelectronics* **2009**, *24*, 1223–9.

[72] Hakim, M. M. A.; Lombardini, M.; Sun, K.; Giustiniano, F.; Roach, P. L.; Davies, D. E.; Howarth, P. H.; de Planque, M. R. R.; Morgan, H.; Ashburn, P. *Nano letters* **2012**, *12*, 1868–72.

[73] Huang, Y.; Dong, X.; Shi, Y.; Li, C. M.; Li, L.-J.; Chen, P. *Nanoscale* **2010**, *2*, 1485–8.

[74] Bergveld, P. *Medical & biological engineering & computing* **1979**, *17*, 655–61.

[75] Bergveld, P. *Sensors and Actuators* **1981**, *1*, 17–29.

[76] Gao, X.; Zheng, G.; Lieber, C. *Nano letters* **2009**, 547–552.

[77] Shinwari, M. W.; Deen, M. J.; Landheer, D. *Microelectronics Reliability* **2007**, *47*, 2025–2057.

[78] Bousse, L.; F. De Rooij, N.; Bergveld, P. *Electron Devices, IEEE ...* **1983**, 1263–1270.

[79] Nair, P. R.; Alam, M. A. *Nano Lett* **2008**, *8*, 1281–1285.

[80] Yates, D. E.; Levine, S.; Healy, T. W. *Journal of the Chemical Society, Faraday Transactions 1* **1974**, *70*, 1807.

[81] Siu, W.; Cobbold, R. *IEEE Transactions on Electron Devices* **1979**, *26*, 1805–1815.

[82] Rooij, N. F. D. E.; Bergveld, P. *Thin Solid Films* **1980**, *71*, 327–331.

[83] Bergveld, P.; Rooij, N. *Sensors and Actuators* **1981**, *1*, 5–15.

[84] Chen, S.; Bomer, J. G.; Carlen, E. T.; van den Berg, A. *Nano Letters* **2011**, *11*, 2334–2341.

[85] Van Der Wal, P.D. and Briand, D. and Mondin, G. and Jenny, S. and Jeanneret, S. and Millon, C. and Roussel, H. and Dubourdieu, C. and de Rooij, N.-F. *Sensors, 2004. Proceedings of IEEE* **2004**, 677–680.

[86] van Hal, R.; Eijkel, J.; Bergveld, P. *Advances in Colloid and Interface Science* **1996**, 31–62.

[87] Bard, A.; Faulkner, L. *Electrochemical methods: fundamentals and applications*, 2nd ed.; John Wiley & Sons, Inc., 1980; p 850.

[88] Khanal, D. R.; Wu, J. *Nano letters* **2007**, *7*, 2778–83.

[89] den Berg, A. V.; Bergveld, P.; van den Berg, A.; Reinhoudt, D.; Sudhölter, E. *Sensors and Actuators* **1985**, *8*, 129–148.

[90] Kosmulski, M. *Langmuir* **1997**, *7463*, 6315–6320.

[91] Lai, C.-S.; Yang, C.-M.; Lu, T.-F. *Electrochemical and Solid-State Letters* **2006**, *9*, G90.

[92] van Kerkhof, J.; Eijkel, J.; Bergveld, P. *Sensors and Actuators B: Chemical* **1994**, *18*, 56–59.

[93] Lloret, N.; Frederiksen, R. S.; Møller, T. C.; Rieben, N. I.; Upadhyay, S.; De Vico, L.; Jensen, J. H.; Nygård, J.; Martinez, K. L. *Nanotechnology* **2013**, *24*, 035501.

[94] De Vico, L.; Iversen, L.; Sørensen, M. H.; Brandbyge, M.; Nygård, J.; Martinez, K. L.; Jensen, J. H. *Nanoscale* **2011**, *3*, 3635–40.

[95] De Vico, L.; Sørensen, M.; Iversen, L.; Rogers, D. M.; Sørensen, B. S.; Brandbyge, M.; Nygård, J.; Martinez, K. L.; Jensen, J. H.; Sø rensen, M. H.; Sø rensen, B. S.; Nygå rd, J. *Nanoscale* **2011**, *3*, 706–17.

[96] Weber, J. R.; Janotti, A.; Van de Walle, C. G. *Applied Physics Letters* **2010**, *97*, 192106.

[97] Wirths, S.; Weis, K.; Winden, A.; Sladek, K.; Volk, C.; Alagha, S.; Weirich, T. E.; von der Ahe, M.; Hardtdegen, H.; Lüth, H.; Demarina, N.; Gruützmacher, D.; Schaäpers, T. *J. Appl. Phys.* **2011**, *110*, 053709.

[98] Madsen, M. H. Indium Arsenide Nanowires - Fabrication, Characterization, and Biological Applications. Ph.D. Thesis, University of Copenhagen, 2013.

[99] Madsen, M. H.; Krogstrup, P.; Johnson, E.; Venkatesan, S.; Mühlbauer, E.; Scheu, C.; Sørensen, C. B.; Nygård, J. *Journal of Crystal Growth* **2013**, *364*, 16–22.

[100] Krogstrup, P. Dynamical Theory and Experiments on GaAs Nanowire Growth for Photovoltaic Applications. Ph.D. Thesis, University of Copenhagen, 2013.

[101] Sze, S. *Physics of Semiconductor Devices (2nd ed.)*; John Wiley & Sons, Inc., 1981.

[102] Nissen, P. D. Spin Qubits in GaAs Heterostructures and Gating of InAs Nanowires for Low-temperature Measurements. Ph.D. Thesis, University of Copenhagen, 2013.

[103] Suyatin, D. B.; Thelander, C.; Björk, M.; Maximov, I.; Samuelson, L. *Nanotechnology* **2007**, *18*, 105307.

[104] Hviid, R. Hafnium Oxide Upgrades pH Sensing InAs Nanowire FET Devices. M.Sc. thesis, University of Copenhagen, 2010.

[105] Knopfmacher, O.; Tarasov, a.; Fu, W.; Wipf, M.; Niesen, B.; Calame, M.; Schönenberger, C. *Nano letters* **2010**, *10*, 2268–74.

[106] Chen, Y. W.; Liu, M.; Kaneko, T.; McIntyre, P. C. *Electrochemical and Solid-State Letters* **2010**, *13*, G29.

[107] Xu, Z.; Liu, Q.; Finch, J. *Applied Surface Science* **1997**, *120*, 269–278.

[108] Frederiksen, R. Development and characterizati on of the InAs NW -BioFET for label - free protein detection. M.Sc. thesis, University of Copenhagen, 2011.

[109] Bryantsev, V. S.; Diallo, M. S.; Goddard, W. A. *The journal of physical chemistry. A* **2007**, *111*, 4422–30.

[110] Baker, M. *Thin Solid Films* **1980**, *69*, 359–368.

[111] Tian, B.; Cohen-Karni, T.; Qing, Q.; Duan, X.; Xie, P.; Lieber, C. M. *Science* **2010**, *329*, 830–4.

[112] Nakanishi, K.; Sakiyama, T.; Imamura, K. *Journal of Bioscience and Bioengineering* **2001**, *91*, 233–244.

[113] Roach, P.; Farrar, D.; Perry, C. C. *Journal of the American Chemical Society* **2005**, *127*, 8168–73.

[114] Brusatori, M. A.; Tie, Y.; Van Tassel, P. R. *Langmuir* **2003**, *19*, 5089–5097.

[115] Ladhani, L. Comparison of Functionalization Methods for Use on an InAs NW Bio-FET. M.Sc. thesis, University of Copenhagen, 2011.

[116] Wright, A. K.; Thompson, M. R. *Biophysical journal* **1975**, *15*, 137–41.

[117] Weber, P. C.; Ohlendorf, D. H.; Wendoloski, J. J.; Salemme, F. R. *Science (New York, N.Y.)* **1989**, *243*, 85–8.

[118] Ge, S.; Kojio, K.; Takahara, A.; Kajiyama, T. *Journal of biomaterials science. Polymer edition* **1998**, *9*, 131–50.

[119] Diamandis, E.; Christopoulos, T. *Clin. Chem.* **1991**, *37*, 625–636.

[120] Rostkowski, M.; Olsson, M. H. M.; Søndergaard, C. R.; Jensen, J. H. *BMC structural biology* **2011**, *11*, 6.

[121] Pugliese, L.; Coda, A.; Malcovati, M.; Bolognesi, M. *Journal of molecular biology* **1993**, *231*, 698–710.

[122] Lu, W.; Lieber, C. M. *J. Phys. D Appl. Phys.* **2006**, *39*, R387 – R406.

[123] Samuelson, L.; Thelander, C.; Bjork, M.; Borgstrom, M.; Deppert, K.; Dick, K.; Hansen, A.; Martensson, T.; Panev, N.; Persson, A.; Seifert, W.; Skold, N.; Larsson, M.; Wallenberg, L. *Physica E* **2004**, *25*, 313 – 318.

[124] Law, M.; Goldberger, J.; Yang, P. *Annu. Rev. Mater. Res.* **2004**, *34*, 83 – 122.

[125] Olsson, L.; Andersson, C.; Hakansson, M.; Kanski, J.; Ilver, L.; Karlsson, U. *Phys. Rev. Lett.* **1996**, *76*, 3626 – 3629.

[126] Bhargava, S.; Blank, H.; Narayanamurti, V.; Kroemer, H. *Appl. Phys. Lett.* **1997**, *70*, 759 – 761.

[127] Noguchi, M.; Hirakawa, K.; Ikoma, T. *Phys. Rev. Lett.* **1991**, *66*, 2243 – 2246.

[128] Offermans, P.; Crego-Calama, M.; Brongersma, S. H. *Nano Lett.* **2010**, *10*, 2412 – 2415.

[129] Nadj-perge, S. Single spins in semiconductor nanowires. Ph.D. thesis, 2010.

[130] Van Dam, J.; Nazarov, Y.; Bakkers, E.; De Franceschi, S.; Kouwenhoven, L. **2006**, *442*, 667 – 670.

[131] Hofstetter, L.; Csonka, S.; Nygard, J.; Schoenenberger, C. **2009**, *461*, 960 – 963.

[132] Hang, Q.; Wang, F.; Buhro, W. E.; Janes, D. B. *Appl. Phys. Lett.* **2007**, *90*, 062108.

[133] Li, H.-Y.; Wunnicke, O.; Borgstrom, M. T.; Immink, W. G. G.; van Weert, M. H. M.; Verheijen, M. A.; Bakkers, E. P. A. M. *Nano Lett.* **2007**, *7*, 1144–1148.

[134] Sorensen, B. S.; Aagesen, M.; Sorensen, C. B.; Lindelof, P. E.; Martinez, K. L.; Nygard, J. *Appl. Phys. Lett.* **2008**, *92*, 012119.

[135] Sau, J. D.; Tewari, S.; Sarma, S. D. *Phys. Rev. B* **2012**, *85*, 064512.

[136] Mao, L.; Gong, M.; Dumitrescu, E.; Tewari, S.; Zhang, C. *Phys. Rev. Lett.* **2012**, *108*, 177001.

[137] Kawaji, S.; Gatos, H. C. *Surface Science* **1967**, *7*, 215 – 228.

[138] Kawaji, S.; Kawaguchi, Y. *Journal of the Physical Society of ...* **1968**,

[139] Kawaji, S.; Miki, S.-i.; Kinoshita, T. *J. Phys. Soc. Japan* **1975**, *39*, 1631.

[140] Wagner, R.; Ellis, W. *Appl. Phys. Lett.* **1964**, *4*, 89–90.

[141] Ford, A. C.; Chuang, S.; Ho, J. C.; Chueh, Y.-L.; Fan, Z.; Javey, A. *Nano Lett.* **2010**, *10*, 509 – 513.

[142] Ballingall, J. M. *Applied Physics Letters* **1982**, *41*, 947.

[143] Greiner, M. E.; Gibbons, J. F. *Journal of Applied Physics* **1985**, *57*, 5181.

[144] Williams, R.; Skuras, E. *Semicond. Sci. Technol. 5*, S338–S341.

[145] Madsen, M. H.; Krogstrup, P.; Johnson, E.; Venkatesan, S.; Mühlbauer, E.; Scheu, C.; Sørensen, C. B.; Nygård, J. *Journal of Crystal Growth* **2012**, –.

[146] Masu, K.; Konagai, M.; Takahashi, K. *Journal of Applied Physics* **1983**, *54*, 1574–1578.

[147] Casadei, A.; Krogstrup, P.; Heiss, M.; Röhr, J.; Colombo, C.; Ruelle, T.; Upadhyay, S.; Sørensen, C.; Nygård, J.; Fontcuberta i Morral, A. *arXiv preprint, arXiv:1210.1670* **2012**, 2–5.

[148] Shtrikman, H.; Popovitz-Biro, R.; Kretinin, A.; Houben, L.; Heiblum, M.; Bukala, M.; Galicka, M.; Buczko, R.; Kacman, P. *Nano Letters* **2009**, *9*, 1506–1510.

[149] Millea, M.; McColl, M.; Silver, A. *J. Electronic Materials* **1976**, *5*, 321.

[150] Millea, M.; Silver, A.; Flesner, L. *Thin Solid Films* **1979**, *56*, 253 – 266.

[151] Bergmann, G. *Solid State Communications* **1982**, *42*, 815–817.

[152] Lysczek, E.; Robinson, J.; Mohney, S. *Mater. Sci. Eng., B* **2006**, *134*, 44 – 48.

[153] Hill, C. J.; Beach, R. A.; McGill, T. C. *J. Vac. Sci. Technol. B* **2000**, *18*, 2044–2046.

[154] Hanson, R.; Kouwenhoven, L. P.; Petta, J. R.; Tarucha, S.; Vandersypen, L. M. K. *Rev. Mod. Phys.* **2007**, *79*, 1455–1455.

[155] Lepselter, M.; Sze, S. *Proceedings of the IEEE* **1968**, *56*, 1400 – 1402.

[156] Sarker, B. K.; Khondaker, S. I. *ACS Nano* **2012**, *6*, 4993–4999.

[157] Wang, D.; Wang, Q.; Javey, A.; Tu, R.; Dai, H.; Kim, H.; McIntyre, P. C.; Krishnamohan, T.; Saraswat, K. C. *Applied Physics Letters* **2003**, *83*, 2432–2434.

[158] Wunnicke, O. *Applied Physics Letters* **2006**, *89*, 083102.

[159] Affentauschegg, C.; Wieder, H. H. *Semicond. Sci. Technol.* **2001**, *16*, 708.

[160] Dayeh, S. A.; Aplin, D. P. R.; Zhou, X.; Yu, P. K. L.; Yu, E. T.; Wang, D. *Small (Weinheim an der Bergstrasse, Germany)* **2007**, *3*, 326–32.

[161] Ford, A. C.; Ho, J. C.; Chueh, Y.-L.; Tseng, Y.-C.; Fan, Z.; Guo, J.; Bokor, J.; Javey, A. *Nano Letters* **2009**, *9*, 360–365.

[162] Blömers, C.; Lepsa, M. I.; Luysberg, M.; Grützmacher, D.; Lüth, H.; Schäpers, T. *Nano Lett.* **2011**, *11*, 3550–3556.

[163] Bloemers, C.; Lepsa, M. I.; Luysberg, M.; Gruetzmacher, D.; Lueth, H.; Schaepers, T. *Nano Lett.* **2011**, *11*, 3550 – 3556.

[164] Lee, P. A.; Stone, A. D.; Fukuyama, H. *Phys. Rev. B* **1987**, *35*, 1039–1070.

[165] Hansen, A. E.; Björk, M. T.; Fasth, C.; Thelander, C.; Samuelson, L. *Phys. Rev. B* **2005**, *71*, 205328.

[166] Roulleau, P.; Choi, T.; Riedi, S.; Heinzel, T.; Shorubalko, I.; Ihn, T.; Ensslin, K. *Phys.∼Rev.∼B* **2010**, *81*, 155449.

[167] Hao, X.-J.; Tu, T.; Cao, G.; Zhou, C.; Li, H.-O.; Guo, G.-C.; Fung, W. Y.; Ji, Z.; Guo, G.-P.; Lu, W. *Nano Lett.* **2010**, *10*, 2956 – 2960.

[168] Liang, D.; Du, J.; Gao, X. *Phys. Rev. B* **2010**, *81*, 153304.

[169] Sheehan, P.; Whitman, L. *Nano letters* **2005**, *5*, 803–807.

[170] Deen, M. J.; Shinwari, M. W.; Ranuárez, J. C.; Landheer, D. *Journal of Applied Physics* **2006**, *100*, 074703.

[171] Jakobson, C.; Nemirovsky, Y. *IEEE Transactions on Electron Devices* **1999**, *46*, 259–261.

[172] Zheng, G.; Gao, X. P. a.; Lieber, C. M. *Nano letters* **2010**, *10*, 3179–83.

[173] van Kerkhof, J.; Bergveld, P.; Schasfoort, R. *Biosensors and Bioelectronics* **1993**, *8*, 463–472.

[174] Bergveld, P.; van Hal, R.; Eijkel, J. *Biosensors and Bioelectronics* **1995**, *10*, 405–414.

[175] Koch, S.; Woias, P.; Kudlich, E.; Zimmerer, B. *Sensors and Actuators B* **1996**, *34*, 289–294.

[176] Koch, S.; Woias, P.; Meixner, L.; Drost, S.; Wolf, H. *Biosensors & Bioelectronics* **1999**, *14*, 413–421.

[177] Liu, Y.; Lilja, K.; Heitzinger, C.; Dutton, R. W. *Electron Devices Meeting* **2008**, 491–494.

[178] Liu, Y.; Huber, D. E.; Tabard-Cossa, V.; Dutton, R. W. *Applied Physics Letters* **2010**, *97*, 143109.

[179] Jung, S. M.; Kim, H.-J.; Kim, B.-J.; Kim, Y.-S.; Yoon, T.-S.; Lee, H. H. *Applied Physics Letters* **2010**, *97*, 153302.

[180] Liesi, P.; Julien, J. P.; Vilja, P.; Grosveld, F.; Rechardt, L. *Journal of Histochemistry & Cytochemistry* **1986**, *34*, 923–926.

Nomenclature

ALD	Atomic Layer Deposition
As	Arsenic
Au	Gold
Be	Beryllium
BSA	Bovine Serum Albumin
CEA	Carcinoembryonic antigen
DAC	data acquisition card
DI	de-ionised water
EBL	Electron beam lithography
In	Indium
IPA	Iso-Propyl Alcohol
LG	Liquid gate
LOD	Limit of detection
MBE	Molecular beam epitaxy
MIBK	Methyl Iso-Butyl Ketone
PSA	Prostrate specific antigen
PZC	Point of zero charge
RF	Radio frequency

SAMs	Self Assembled Monolayers
SBM	Site binding model
SO	Spin-orbit
TCEP	Tris(2-carboxyethyl)phosphine hydrochloride
Ti	Titanium
TRIS	Tris (hydroxymethyl)aminomethane
UCF	Universal conductance fluctuations
WAL	Weak anti-localization
WL	Weak localization